

Atomic Waves in Inhomogeneous Light Media

Dissertation zur Erlangung des Doktorgrades

Dr. rer. nat.

der Fakultät für Naturwissenschaften

der Universität Ulm

von

Stephan Meneghini

aus Ulm

UNIVERSITÄT ULM

ABTEILUNG FÜR QUANTENPHYSIK

LEITER: PROF. DR. W. P. SCHLEICH



ULM, AUGUST 2000

*Für meinen Vater, der das Ende dieser
Promotion leider nicht mehr miterleben durfte.*

Amtierender Dekan: Prof. Dr. O. Marti
1. Gutachter: Prof. Dr. W.P. Schleich
2. Gutachter: Prof. Dr. P. Reineker
Tag der Promotion: 16. Oktober 2000

Zusammenfassung

Experimentelle Quantenoptik mit isolierten Quantensystemen ist ein junges Forschungsgebiet. Die technologischen Fortschritte der letzten Jahre haben viele grundlegende Experimente erst ermöglicht. Angespornt durch die Versuche in der Gruppe von Mark Raizen (Austin) und Ton van Leeuwen (Eindhoven) haben wir die Wechselwirkung von Lasern mit Atomstrahlen untersucht. In diesen Experimenten wurde die transversale Struktur eines Atomstrahls verändert. Diese Manipulationen werden durch die Modulation des Laserfelds verursacht. Das Ziel dieser Arbeit ist die detaillierte Untersuchung verschiedener Laserfeldmodulationen in longitudinaler und transversaler Richtung und deren Auswirkungen auf die Form des transversalen Atomstrahlprofils. Zusätzlich arbeiten wir mit Dämpfung, um in bestimmten Bereichen störende Atome zu beseitigen. Für unsere Untersuchungen verwenden wir analytische Näherungen und numerische Simulationen. Teile unserer Arbeit wurden auch schon in Konstanz in der Gruppe von Jürgen Mlynek experimentell realisiert. Dort ist das Ziel, Nanolithographie mit atomaren Wellen zu entwickeln.

In unseren Überlegungen kommt ein Strahl aus Zweiniveau-Atomen zum Einsatz, die ein stehendes Lichtfeld durchqueren. Der Laser spricht den Übergang von einem metastabilen Grundzustand zu einem angeregten Zustand an. Von diesem aus ist zudem ein spontaner Zerfall möglich. Die transversale Bewegung der Atome ist quantisiert. Wir haben nun die Auswirkungen von Resonanz oder Verstimmung des Lasers bezüglich des Übergangs untersucht. Dabei konzentrieren wir uns auf Orts- und Impulsverteilungen der Atome im Grundzustand. In unseren Rechnungen nehmen wir an, daß alle Atome mit gleichbleibend hoher Geschwindigkeit fliegen. Deshalb können wir die Koordinate in Ausbreitungsrichtung des Strahls eliminieren und das Problem eindimensional beschreiben.

Im ersten Teil haben wir gezeigt, daß ein stark verstimmtes, stehendes Laserfeld einen Atomstrahl bündeln kann. Dabei wirken die einzelnen Schwingungsknoten des Feldes als Linsen, die die Streuung des Atomstrahls verkleinern. Hier sind die Rollen von Licht und Materie im Gegensatz zur klassi-

schen Optik vertauscht. Wir nutzen die Lichtwellen, um Materie abzulenken und zu fokussieren. Dabei finden wir auch im Rahmen der Atomoptik „Linsenfehler“ oder Abberation. Für eine perfekte Fokussierung wären unendlich hohe, parabolische Potentiale notwendig, die experimentell nicht realisierbar sind. Stattdessen setzen wir das endliche Potential $\sin^2 kx$ eines Feldes mit Modenfunktion $\sin kx$. Im Bereich der Knoten ist die parabolische Näherung sehr gut. Problematisch sind die Atome, die das Feld im Bereich der Schwingungsbäuche passieren, denn dort verfügt das Laserfeld nicht über die nötige Ablenkungskraft. Damit diese Teilchen den Effekt der Fokussierung nicht verwischen, werden sie durch rein mechanische Blenden entfernt. So wird auf technisch einfache Weise die Qualität der Fokussierung verbessert.

Eine andere Möglichkeit des Ausblendens kann mit einem zusätzlichen, resonanten Laser erzielt werden. Dieser wird der bisherigen Anordnung vorgeschaltet und induziert den Übergang in den angeregten Zustand. Dabei erhalten wir mehr Zerfälle im Bereich der Schwingungsbäuche und wenige bei den Knoten. Daraus resultiert ein gaußförmiges Profil unseres Atomstrahls, dessen Maximum in die Schwingungsknoten der verstimmtten Laserwelle zur Fokussierung geführt werden kann. Durch die Kombination von resonantem und verstimmttem Laser haben wir somit eine Fokussierung mit hoher Qualität durchgeführt.

Bei bestimmten Parametern liegt die Fokusebene im Laserfeld. Deshalb untersuchen wir auch Techniken, diese Ebene zu verschieben. Dabei ist es auch möglich, die Abstände der fokussierten Maxima zu verkleinern. Dies wird durch den fraktionalen Talbot Effekt bewirkt. Der einfache Talbot Effekt führt durch freie Propagation einer Welle zur Wiederholung einer periodischen Struktur. Dies geschieht in makroskopischen Dimensionen und ermöglicht die Wiederholung unserer fokussierten Abbildung außerhalb des Laserfelds. Jedoch können auch bei ganz bestimmten Beobachtungsebenen diese fokussierten Punkte in hoher Anzahl mit entsprechend geringerer Amplitude beobachtet werden. Dies ist der fraktionale Talbot Effekt. In unserem Fall erreichen wir so Abbildungen des fokussierten Atomstrahlprofils im Bereich von einigen Nanometern mit einem Abstand von einer zehntel Laserwellenlänge.

Im nächsten Abschnitt unserer Untersuchungen haben die Atome nur ein Laserfeld durchquert. Bei diesem wurde die Verstimmung während des Experiments verändert. Entweder war der Laser anfangs rot und zum Ende hin blau verstimmt oder umgekehrt. Dabei wurde die Verstimmung so geregelt, daß der Laser zum Zeitpunkt der maximalen Intensität resonant war. Dieses Verhalten erzeugt sowohl Dämpfung im Bereich der Resonanz als auch transversale Streuung der Atome. Bei anfänglich rot verstimmttem Licht fallen beide Effekte zusammen und wir erhalten einen Quantenteppich mit

einfachen Strukturen, da die stark beschleunigten Teilchen sofort gedämpft werden. Wird der Laser zu Beginn jedoch blau verstimmt, werden Streuung und Dämpfung räumlich getrennt. Es zerfallen vorwiegend die Atome, die im ursprünglichen Zustand verblieben sind. Die Teilchen jedoch, die stark abgelenkt wurden, befinden sich in Bereichen der schwachen Dämpfung und erhalten hohe transversale Impulse und diese führen zu komplizierten Quantenteppichen.

Im letzten Teil der Arbeit haben wir einen Strahlteiler simuliert. Dazu wurden zwei stehende Laserfelder gekreuzt. Bei einem kleinen Winkel entsteht ein Feld mit einer zusätzlichen longitudinalen Modulation. Bei geeigneter Wahl des Winkels erhalten wir die Doppler-Resonanz zu den transversalen Impulszuständen. Diese führt dann in der Wechselwirkung mit den Atomen zu transversaler Streuung. Diese Streuung betrifft je nach Parameter mehr oder weniger Atome. Findet der Impulsübertrag auf die Mehrheit der Atome statt, erhalten wir in jeder Periode des Ortsraums einen zweiten Peak. Je mehr Atome im Ausgangszustand verbleiben, desto schwächer ist der Effekt ausgeprägt. Wir haben aber auch einen Parameterbereich gefunden, in dem fast alle Atome gestreut werden.

Um weitere atomare Maxima pro Ortsraumperiode zu bekommen, müssen Zustände höherer transversaler Impulse besetzt werden. Wir haben ein Modell entwickelt, mit dem eine gezielte Streuung vorgenommen werden kann. Dazu wird die vorige Anordnung verdoppelt. Wir benutzen also zwei Paare stehender Laserfelder. Die Paare unterscheiden sich in der Intensität und im Winkel oder in der longitudinalen Modulationsfrequenz. Die Frequenzen sind so gewählt, daß die zugehörigen Energien für die Übergänge erreicht werden. Diese Anordnung ist an das STIRAP Modell angelehnt. STIRAP steht für *STImulated Raman Adiabatic Passage*. Hierbei werden Atome durch einen Dunkelzustand in einen weiteren Zielzustand transferiert. In unserem Fall jedoch ist der Übergang nicht adiabatisch. Wir betrachten die quantisierten Impulszustände in transversaler Richtung, die nacheinander besetzt werden. Es gibt bei unserem Modell keinen Dunkelzustand.

Um Zustände hoher kinetischer Energie mit verhältnismäßig geringer Laserintensität zu erreichen, erfolgt der Transfer in Stufen zwischen den Zuständen und nicht in einem Schritt. Wir dokumentieren den Effekt durch einen Transfer vom Zustand ohne transversalen Impuls über den $2\hbar k$ Zwischenzustand in den $4\hbar k$ Zielzustand. Des weiteren zeigen wir die Auswirkungen von nicht transferierten Teilchen.

Contents

1	Introduction	1
1.1	Description of the Model	1
1.1.1	Normal Incident	2
1.1.2	Incident under Bragg Angle	3
1.1.3	Interaction with Laser Field	3
1.2	Experimental Setup	5
1.2.1	Beam Setup	5
1.2.2	Trap Setup	6
2	Focusing and Multiplication	7
2.1	Introduction	7
2.2	Focusing Revisited	8
2.2.1	Focusing in Theory	8
2.2.2	Numerical Approach to Focusing	10
2.2.3	Full Numerical Simulation	10
2.3	Talbot Effect	13
2.3.1	Talbot Images	15
2.3.2	Fractional Talbot Effect	18
2.4	Focus and High Period	18
2.4.1	A Historic Review	18
2.4.2	Beam Aperturing	20
2.5	Demands on Atomic Beam	26
2.5.1	Beam Collimation	26
2.5.2	Spread in Axial Velocity	27
2.6	Conclusions	28
3	Time-Dependent Detuning	29
3.1	Setup and Time Scales	29
3.2	Approximate Analysis	30
3.2.1	Mixing of Waves	31
3.2.2	Asymptotic Behavior for $t \rightarrow +\infty$	32

3.2.3	Limit of Small Angular Detuning	32
3.3	$\Delta(t) = \arctan(t)$	33
3.3.1	A Close View on the Potential	35
3.3.2	Interpretation and Explanation	35
3.4	$\Delta(t) = -\arctan(t)$	37
3.4.1	Time Evolution of the Beam	37
3.4.2	Analysis of the Potential	37
3.5	Quantum Kicks	41
3.6	Experimental Realization	41
4	The Beam-Splitter	43
4.1	Model of a Light Crystal	43
4.2	A Feeling for Parameters	45
4.2.1	No Modulation	45
4.2.2	A Touch of Scattering	46
4.2.3	Result of Modulation	49
4.3	Effect of Intensity	49
4.3.1	Introduction of Iterative Scattering	49
4.3.2	Enforced Scattering	49
4.3.3	Back Scattering or Saturation?	52
4.4	Conclusion	53
5	Stepwise Scattering	55
5.1	The STIRAP Model	55
5.1.1	Transitions in a Two-Level System	56
5.1.2	Processes in a Three-State System	57
5.2	Our Setup	60
5.2.1	Energy Structure	60
5.2.2	Laser Field Configuration	62
5.2.3	Analytical Solution	63
5.3	Numerical Results	65
5.3.1	Narrow Beams	66
5.3.2	Wide Beams	66
5.4	Conclusion	69
A	Paraxial Approximation	71
B	Focusing Function	73

C	Analytical Solution of Two Wave Mixing	75
C.1	Analytical Model	75
C.1.1	Approximate Solution	76
C.1.2	Hankel Functions	77
C.2	Regimes of Damping and Scattering	79
C.2.1	Asymptotics after Interaction	79
C.2.2	Conclusion	82
D	Scattering with Nonadiabatic Modulation	83
D.1	The Basic Dynamics	83
D.1.1	Weakly modulated crystal	84
D.1.2	Resonant modulation of the crystal	86
D.2	Quantum Kicks	89
D.3	Conclusions	90
E	The Numerics	93
	Bibliography	95
	Acknowledgment	99
	Curriculum Vitae	101
	List of Publications	103

Chapter 1

Introduction

The progress in experimental quantum optics and especially the experiments of Mark Raizen (Austin) and Ton van Leeuwen (Eindhoven) have motivated us to investigate atom optics. These experiments have shown that standing laser fields can easily manipulate the transversal profile of an atomic beam. The modulation of the field can be used for nanolithography. To imprint structures we have to alternate the transversal profile of the atomic beam. We reach this goal by modulating the laser field in longitudinal and transversal direction. The aim of this thesis is to analyze in detail various field configurations with respect to atomic beam modulation. Therefore, we use analytic approximations and numerical methods.

Especially we focus on the role of the detuning in the interaction of the laser field and the particles. We build lenses and deal with their faults like in classical optics. Furthermore, we investigate scattering in different ways. For all these ideas we need an atomic beam and a laser field in a special configuration. Nevertheless, we do not insist on the beam geometry. We use for our calculations the model of an atomic beam. Although, the realization in a trap is possible as well.

1.1 Description of the Model

Throughout the thesis we consider the model of an atomic beam. We assume that the atoms have the same velocity v_z in z -direction. This velocity is considered to be large and constant for the whole experiment. Therefore, we treat this motion classically which yields for the position $z = v_z \cdot t$. This implies scaling the propagation along the z -axis into a time evolution of a position wave function. The treatment reduces this problem to a 1D-scheme.

In Fig. 1.1 we illustrate the setup. The atoms are prepared at an early

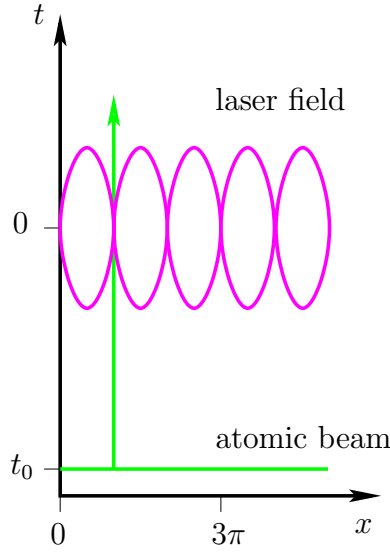


Figure 1.1: The schematic model of our investigations. The periodicity of the laser field along the x -direction is scaled to π . The atomic beam is prepared at time t_0 . The atom is initially a plane wave moving towards the laser field which has a time-dependent intensity. This envelope in t -direction is described by a Gaussian and thus slowly switches on and off the interaction.

stage t_0 and pass on their way in z -direction a standing laser field with a Gaussian profile in time or space. This simulates a realistic laser field with a spread.

The core of our investigation is the center-of-mass motion in the transverse x -direction. This we treat quantum mechanically and look for position and momentum distributions. Our special interest concentrates on the time evolution of these quantities which is, due to our scaling, the 2D-solution of the interaction with the laser field.

1.1.1 Normal Incident

The atom is prepared in an early stage $t_0 \ll 0$. The preparation affects only transversal properties. The longitudinal z -direction is treated as time evolution due to the constant velocity v_z of the beam. This paraxial approximation we describe in more detail in App. A. We can shape the cross-section of the beam with a certain profile, for example a rectangle or a Gaussian

$$\psi(x, t_0) = \mathcal{N} \exp \left[- \left(\frac{x - x_0}{2\Delta x} \right)^2 \right].$$

The profile is chosen such that the probability distribution $|\psi|^2$ has the mean value x_0 and the spread Δx . Alternatively we use a plane wave

$$\psi(x, t_0) = \mathcal{N}$$

which has no transversal profile. Additionally we can assume a general transversal momentum which is the same for all particles.

In both examples \mathcal{N} denotes the normalization constant. As shown in Appendix E we use a discrete and finite description. To apply the Fast Fourier Transform (FFT) we have to use a periodic setup. The periodicity is determined by the wavelength of the laser field. Throughout this thesis we calculate one period out of a perfect regular structure. Within this period we can normalize the wave function ψ . To get a better impression of the results we usually depict a few periods. This way of handling neglects marginal effects. Indeed, they play no important role because the width of the atomic beam is much broader than the wavelength of the laser. Therefore, the atoms reach over many laser periods.

1.1.2 Incident under Bragg Angle

Since our model is restricted to an atom beam traveling along the z -axis, we have to describe the non-normal incident of the atoms as transversal momentum of the beam. We do not rotate the laser field but turn our coordinate system. The superposition of normal incident and transversal momenta has the same effect as shown in Fig. 1.2. A plane wave crossing the potential field at the Bragg angle is written as

$$\psi(x, t_0) = \mathcal{N} \exp(-ip_{\vartheta}x).$$

According to standard quantum mechanics this wave function describes a plane wave with a constant transversal momentum.

For the numerical integration it is not important, how complicated the wave function is. The main input is the initial wave function at time t_0 and the corresponding potential.

1.1.3 Interaction with Laser Field

We use three-level atoms illustrated in Fig. 2.8. The atoms are prepared in a metastable ground state $|g\rangle$. The laser field acts on the transition $|g\rangle \leftrightarrow |e\rangle$. From the excited state there exists a decay channel to a non-detected state $|nd\rangle$ with a decay rate γ . In the weak saturation regime $dE/\hbar \ll \gamma$ we can

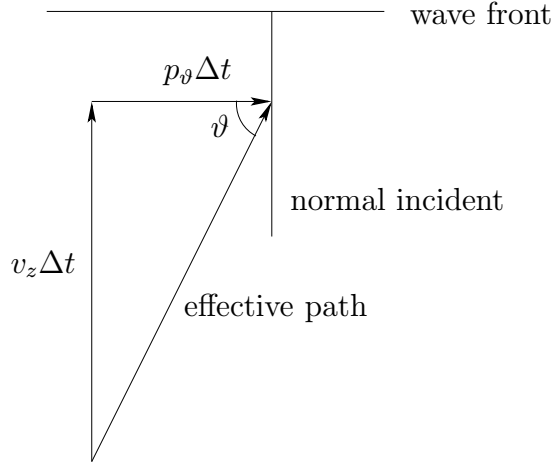


Figure 1.2: To make the atoms enter the laser field under the Bragg angle ϑ we just combine the flight along the z -axis with velocity v_z and a transversal momentum p_ϑ . Simple geometry leads to the relation $p_\vartheta = v_z / \tan \vartheta$.

eliminate the excited state and describe the whole system only in the ground level. Effectively, we describe the interaction by the potential

$$V(x, t) = \frac{(dE)^2}{\hbar} \frac{\sin^2 kx}{\Delta + i\gamma/2}.$$

Here d denotes the dipole moment of the atom and E represents the electric field of the laser.

Since we consider a standing wave we have a $\sin kx$ modulation of the field in transversal beam direction with wave number k . Further we take into account the detuning of the laser frequency Δ . Spontaneous emission back to the ground state is neglected.

In order to include the finite width of the laser field we extend our potential to

$$V(x, t) = \frac{(dE)^2}{\hbar} \frac{\sin^2 kx}{\Delta + i\gamma/2} \exp(-t^2/T^2)$$

where T denotes the Gaussian width of the field.

Now we can start solving the time-dependent Schrödinger equation

$$i\hbar \frac{\partial}{\partial t} \psi(x, t) = \left[\frac{\hat{p}^2}{2M} + V(\hat{x}, t) \right] \psi(x, t)$$

for difficult potentials and initially given wave functions.

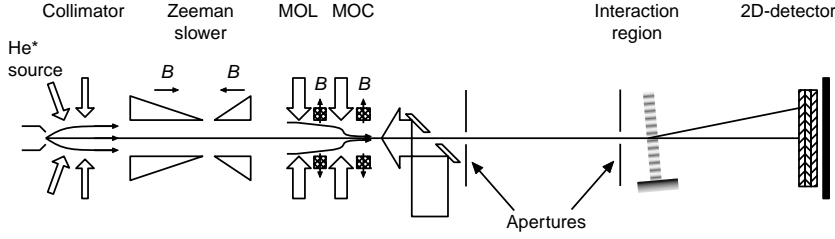


Figure 1.3: Schematic illustration of the Eindhoven beam experiment for metastable He^* atoms. The source sends the atoms with a wide spread. Hence via collimator and Zeeman slower the atoms are prepared. In the next stage the atoms are focused to a beam with magneto-optical devices. Due to apertures only central atoms are allowed to pass the interaction region and finally the atoms are detected in their 2D-distribution.

Since it is impossible to diagonalize both operators simultaneously we can solve these problems only numerically. Therefore, we describe the initial wave function at an early time t_0 and integrate this wave function with the split-operator technique described in App. E.

1.2 Experimental Setup

The thesis represents a numerical simulation for an experimental situation. Therefore, real atoms and experimental problems are not our main concern. Nevertheless, these ideas are not out of the world and we want to show that it is indeed possible to do the experiments.

1.2.1 Beam Setup

We have enjoyed an intensive collaboration with the group of Ton van Leeuwen from Eindhoven. He plans to realize some of our suggestions with the experimental setup shown in Fig. 1.3.

The special part of the Eindhoven group is the large size of the apparatus. It is about 10 meters long including the oven, the Zeeman slower, the interaction chamber and some so-called “elbow-space” to make use of the Talbot effect. Of course, there exist many atomic beam experiments but most of them are too small to observe the Talbot effect. Nevertheless, this is no limit for some ideas, since the fractional Talbot effect is a near field topic.

The detection of the atom is done in the following way: The atoms are prepared in a metastable state. We are only interested in those atoms that are finally still in the metastable state. A wire is moved through the beam

and the atom induces a current by decaying into low energy state. This yields immediately the spatial distribution. The momentum distribution is only available as position distribution in the far field. Since the measurement destroys the distribution we cannot repeat the measurement later for evaluation of the momentum distribution. This repetition is only possible in the trap scheme discussed in the next section.

1.2.2 Trap Setup

The other way of realizing experimentally our calculations is to use a magneto-optical trap. Mark Raizen did many experiments proposed for beams in the trap. In this case the idea of time evolution instead of propagation is realized, too.

In Mark Raizen's group the momentum distribution of the particles is observed indirectly. Via CCD camera density pictures of the atom cloud are taken. Out of a series in fixed time steps the momentum distribution is calculated.

The advantage of the trap is that the spatial dimensions of the experiment are much smaller than in the beam configuration. Another advantage we find in Chapter 3 where we have to apply a position-dependent magnetic field. Its intensity is connected to the velocity of the particles. In comparison to the beam arrangement this can be realized in the beam setup much simpler: Here we just need a time-dependent magnetic field. The strength is connected to the laser intensity. These parameters can be controlled much easier.

Chapter 2

Focusing and Multiplication

A standing light wave can be used as an array of micro-lenses to focus an atomic beam. In this chapter we present theoretical and practical considerations related to this focusing effect. At the end of this chapter we extend the technique to the production of regular structures with a much smaller period than that of the standing light wave. For this, we make use of the fractional Talbot effect which provides us with many shifted repetitions of our focused structure. We investigate different initial conditions for the beam and techniques to prepare the beam.

The combination of focusing with the fractional Talbot effect results in a practical scheme to produce nanostructures. Masking of the incoming atomic wave by an absorptive grating is used to eliminate atom-optical aberrations that would otherwise wash out the fractional Talbot images. The scheme allows the creation of structures of very small feature size as well as small period.

2.1 Introduction

Focusing of atoms in optical standing waves creates periodic structures with feature sizes in the nanometer region. The structures can be produced either through direct deposition from an atomic beam [4, 13, 17–19, 29, 30, 33, 40], or through exposing a resist layer on a substrate with metastable rare gas atoms and subsequent processing [4, 17, 18, 33]. McClelland *et al.* [13, 19, 29, 30, 40] used one- and two-dimensional standing waves as an array of cylindrical and spherical micro-lenses to focus a beam of chromium atoms to an array of lines or dots on a substrate. Feature sizes of 38 nm at spacings of 213 nm were achieved. So far, metastable atoms have only been used without focusing in a proximity printing process, but extension of the technique to include

focusing should be straightforward.

The application of near field imaging in atom optics to the production of regular nanostructures with a smaller period has been suggested, e.g., by Janicke and Wilkens [20]. In the near field diffraction pattern of atoms passing through a regular structure (e.g., a transmission grating or an optical standing wave), images with a regular structure with a period equal to an integer fraction of the original period can arise [11]. The fundamental Talbot image with a period equal to that of the original structure, has been first observed for atoms by Clauser and Li [16] and by Chapman *et al.* [14]. The so-called fractional Talbot images have been observed by Nowak *et al.* [34] using metastable helium atoms passing through a transmission grating.

In this chapter we will show that the combination of focusing and high-order fractional Talbot imaging allows the production of structures with very small feature sizes as well as a small period. We discuss the feasibility of such an approach and present solutions to problems which arise. The calculations of the atomic focusing and diffraction are based on a numerical integration of the one-dimensional atomic wave equation.

2.2 Focusing Revisited

First we want to investigate the principle of focusing. Therefore, we apply a highly detuned laser field to the atom beam. Due to the detuning the field does not change populations or coherences of the internal levels of the atoms. However, momentum can still be transferred to the atoms.

2.2.1 Focusing in Theory

The focusing action in a standing light wave is provided by the spatially corrugated dipole potential which can be described by $\sin^2 kx$. For red detuning, the minima of this potential are near the nodes where we can use the parabolic approximation for the dipole potential. Hence, we assume the Hamiltonian

$$H = \frac{\tilde{p}^2}{2M} + f(t)M\omega_0^2 \frac{\tilde{x}^2}{2}$$

for a time-dependent harmonic oscillator. The function $f(t)$ switches the potential on and off as experienced by the atom crossing the standing light wave. We assume for this switching function a Gaussian envelope

$$f(\tilde{t}) = \exp\left[-(\tilde{\alpha}\tilde{t})^2\right].$$

Note that this envelope is not normalized. Hence, the parameter α combines the properties *width* and *maximum* of the envelope. For the sake of simplicity we combine all in one parameter. We will see soon that this is no restriction for experimental results.

With the scaling relations

$$p = \frac{\tilde{p}}{\hbar k}, \quad t = \frac{\hbar k^2}{M} \tilde{t} = 2\omega_R \quad \text{and} \quad x = \sqrt{\frac{M\omega_0^2}{\hbar^2 k^2}} \tilde{x}$$

we find the Hamiltonian

$$H = \frac{p^2}{2} + f(t) \frac{x^2}{2}$$

including the switching function

$$f(t) = \exp[-(\alpha t)^2]$$

in dimensionless coordinates. Here ω_R denotes the recoil frequency. The only free parameter α comes in via $f(t)$.

The Hamiltonian shows the well-known problem of a time-dependent harmonic oscillator. Hence, we need the solutions $s(t)$ and $c(t)$ of the set of differential equations

$$\begin{aligned} \ddot{c}(t) + \omega_0^2 f(t) c(t) &= 0 \\ \ddot{s}(t) + \omega_0^2 f(t) s(t) &= 0 \end{aligned} \tag{2.1}$$

with the initial conditions

$$\begin{aligned} \dot{c}(t) = s(t_0) &= 0 \\ c(t) = \dot{s}(t)/\omega_0 &= 1. \end{aligned}$$

With the solution of the time-dependent harmonic oscillator we apply the parameter set for the parabolic approximation in the standing laser field.

In our theoretical considerations we use an initial Gaussian wave

$$\psi(x, t_0) = \mathcal{N} \exp \left[-\frac{1}{2} \left(\frac{x}{\Delta_0} \right)^2 \right] \tag{2.2}$$

located near a node of the light field. From Appendix B we find that the wave function remains a Gaussian with the time evolution of the width following from

$$\Delta(t) = \frac{\sqrt{s^2(t) + \Delta_0^4 c^2(t)}}{\Delta_0}. \tag{2.3}$$

2.2.2 Numerical Approach to Focusing

We can now solve the differential equations Eq. (2.1) numerically for different parameters α and a fixed initial width $\Delta_0 = 10$ to find the parameter regimes for good focusing. Fig. 2.1 displays the results for $\Delta(t)$. From the figure we check the focus for two aspects in order to find a parameter regime suitable for sharp focusing. First we are interested in the minimum focus width. The second aspect is the location of the focus relative to the laser field. Two parameter values seem to be of special interest: $\alpha = 0.6101$ and $\alpha = 2.0$. The first will put the focus in the center while the effect of focusing vanishes after the interaction. The other parameter value shows a clear focus in free space.

2.2.3 Full Numerical Simulation

Now that we have identified the interesting parameter regimes, we can check the results by a full numerical calculation. Here we integrate the wave function Eq. (2.2) with the split-operator technique and the potential

$$V(x, t) = \frac{(dE)^2}{\hbar} \frac{\sin^2 kx}{\Delta + i\gamma/2} \exp(-t^2/T^2).$$

Since we use the fast Fourier transform to integrate we need a periodic setup. Hence, we extend our model to an array of beams. We have to prepare this atomic beam in a special state: The transversal Gaussian distributions are restricted to the nodes of the potential. Otherwise we are not able to use the parabolic approximation. A rough collimation is necessary. When we assume that this pre-collimation is done, we can guide the beam through the potential. The result for $\alpha = 0.6101$ is shown in Fig. 2.2.

The beam with the Gaussian profile moves from bottom to top. Magenta and red denote high probability, blue a low one. The time scale is chosen in such a way that the natural spread of the Gaussian due to free evolution is negligible. The black line in the right graph just indicates the envelope of the potential. This simulates the switching of the potential as it acts on the atoms. The parameter α of the switching function is chosen such that the focus is centered within the potential, at time $t = 0$.

The red line in the right diagram denotes the *full width at half maximum* of the central wave packet. After $t \cong 2.8$ the beam extends over the whole period. At this time interferences arise from the overlap with the neighboring beams. Therefore, we cannot calculate the width any more.

The focus has a non-zero background. This indicates aberration like in classical optics. The potential does not provide perfect parabolas but

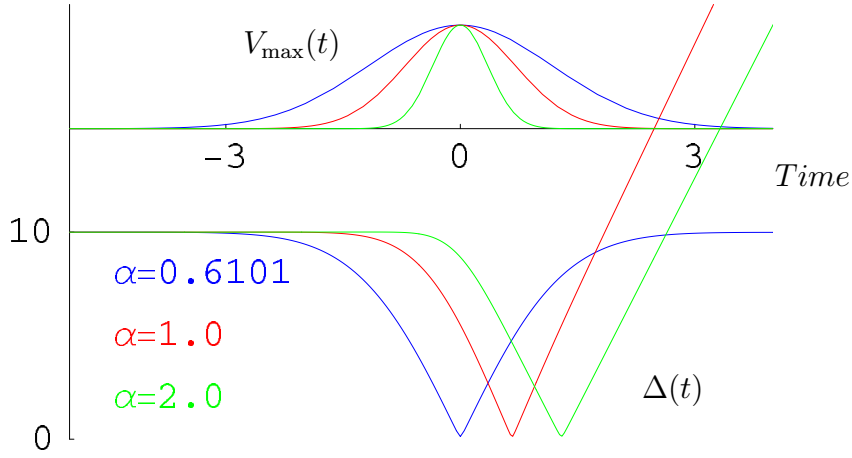


Figure 2.1: Envelope and focusing function. In the upper part we show the envelope of the laser field for $\alpha = 0.6101, 1.0$ and 2.0 . The bottom displays the focusing function evaluated from Eq. (2.3). One can clearly see the focus or the minimum width, respectively. In theory there is no important difference in the focal width. The larger α is, the later the focus appears. This has the advantage that the focus moves from the center of the potential ($\alpha = 0.6101$) to a place clearly outside ($\alpha = 2.0$). Note, that in the case of $\alpha = 0.6101$ the output wave function has the same width as the input function. The focus is located in the center.

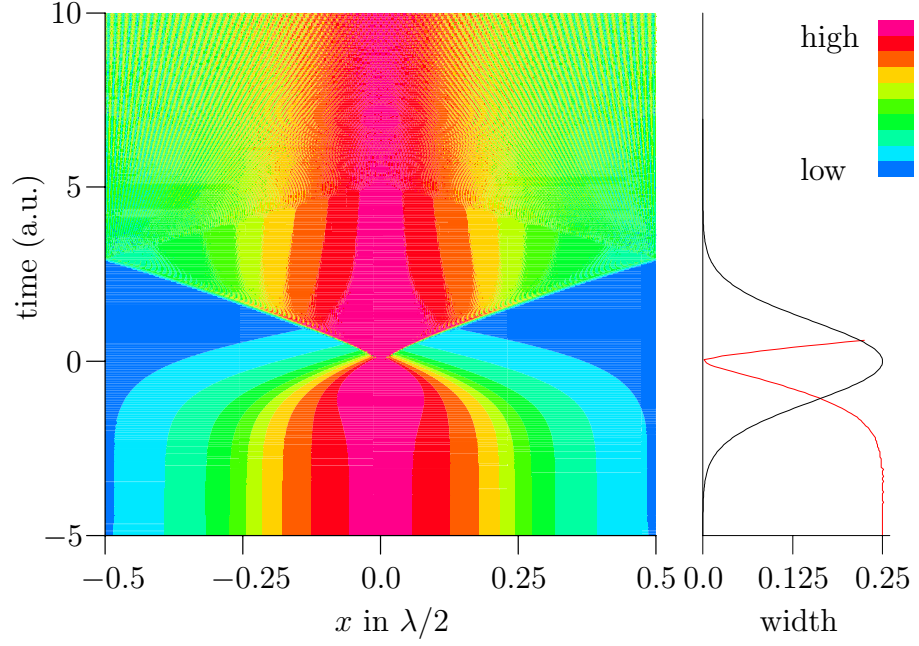


Figure 2.2: Focusing of a Gaussian beam by a $\sin^2 kx$ potential. The right diagram shows the evolution of the maximum potential intensity in time (black line). The red line displays the FWHM width of the Gaussian wave packet. From Fig. 2.1 we know that the final evolution is linear. Since this extends the plot range the line is cut earlier. The left hand side shows a density plot of the probability in time. Blue denotes low probability, magenta is high. One can see clearly the focus at $t = 0$ and the following spread. Note the aberration effect: Near the focus, the cyan background indicates a non-zero base level of the central peak. This is due to the outer part of the Gaussian wave packet which does not experience a strict parabolic potential and hence, is not well focused.

it is given by a \sin^2 function. Therefore, particles, which are too far from the center, are not focused strongly enough and smear out the focus. This is equivalent to the effect of spherical aberration in classical optics where non-paraxial rays are not focused to the same spot as paraxial rays. Due to the aberration there are interferences already around the focusing plane. They disturb the picture and hence, we have to stop calculating the width at $t \cong 1.5$. Since the width evolves linearly we can easily predict the values for times $t > 1.5$.

This parameter regime includes a particular property: The focus is centered in the laser field. This complicates the positioning of a substrate in the focus plane. Nevertheless, due to experimental restrictions the focus in the center of the field is sharper than outside. Hence, many experimentalists prefer this setup. There are two principle ways to avoid this problem: *(i)* We use the Talbot effect to reproduce the focus again after the half Talbot time or *(ii)* we change our parameters such that we get the focus outside of the potential accepting the loss of sharpness.

The first approach works. But since the potential is still there, we do not have the required free evolution for the Talbot effect. This leads to uncertainties and an increase of the focus size.

Changing the parameter regime is much simpler. In Fig. 2.3 we present the focusing for a relatively narrow field envelope. The evolution of the Gaussian beamlets before the interaction is the same as before. Now the potential rises and decays faster. This is like a short symmetric kick on the beam, equivalent to the effect of the thin lens in classical optics.

In the diagram on the right hand side we can clearly see that the focus is outside of the potential. This gives enough space for working in an experiment. Thus, there is enough room to position a substrate in the focus plane.

Now we have realized a working regime for focusing of atomic beams. This is one of the basic techniques in this chapter.

2.3 Talbot Effect

In 1836 H. F. Talbot reported in a paper [43] entitled “Facts Relating to Optical Science” a diffraction experiment. He used a plate of glass covered with gold leaf, on which several hundred parallel lines were cut in order to transmit the light at equal intervals. It is interesting to note that this grating was produced for him by Joseph Fraunhofer. Talbot viewed the light, which had passed through the grating with a lens and found:

The appearance was very curious, being a regular alternation of

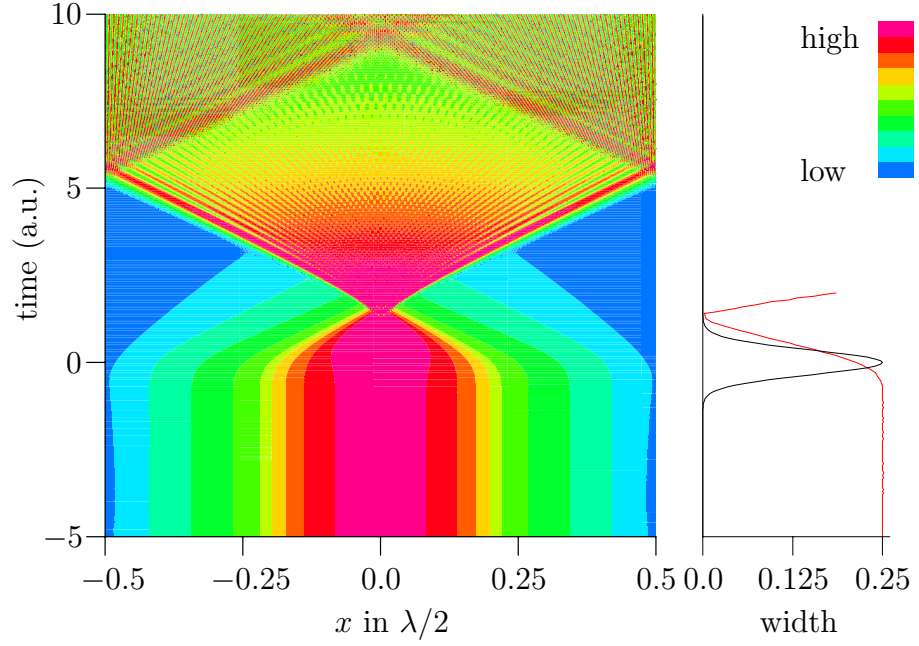


Figure 2.3: Focusing of a Gaussian beam outside of the potential. Now the potential is narrow. The interaction yields a momentum distribution such that the beam is focused behind the interaction region. Since we use a $\sin^2 kx$ potential we find aberration. The atoms far from the nodes are not focused well and cause interferences. We cannot determine the width of the atomic beam further than $t \approx 2$. This behavior is less important since the evolution of the width is linear at this stage.

numerous lines or band of red and green color, having their direction parallel to the lines of the grating. On removing the lens a little further from the grating, the bands again became red and green. And this change continued to take place for an indefinite number of times, as the distance between the lens grating increased. IN all of cases, the bands exhibited two complementary colors.

In contrast to H. F. Talbot we consider a monochromatic wave with transverse periodic structure under free evolution. Hence, we find at a well-defined distance the original structure again. This self-rebuilding effect is called the Talbot effect. The required distance depends on the periodicity and the wavelength, or in the case of atomic waves on the longitudinal velocity, which determines the de Broglie wavelength λ_{dB} . The distance which is necessary for self-rebuilding is called Talbot length and in terms of wavelength it reads

$$L_T = \frac{2a^2}{\lambda_{\text{dB}}}$$

where a is the periodicity of the initial wave.

2.3.1 Talbot Images

In a periodic setup and with free evolution we find the Talbot effect. In this regime we use the familiar Hamiltonian

$$H = \frac{p^2}{2M} = -\frac{\hbar^2}{2M} \frac{\partial^2}{\partial x^2}$$

of a free particle. Further we assume wave function $\psi(x, t_0)$ prepared in an arbitrary state at a fixed time t_0 . Now we have to solve the time-dependent Schrödinger equation

$$i\hbar \frac{d\psi(x, t)}{dt} = H\psi(x, t) = -\frac{\hbar^2}{2M} \frac{\partial^2 \psi(x, t)}{\partial x^2}. \quad (2.4)$$

Due to the periodic setup we can use the Fourier decomposition of the wave function

$$\psi(x, t) = \sum_{n=-\infty}^{\infty} \exp[2\pi i n \frac{x}{a}] a_n(t) = \sum_{n=-\infty}^{\infty} \varepsilon_n a_n(t)$$

to substitute into the Schrödinger equation Eq. (2.4)

$$i\hbar \frac{\partial}{\partial t} \sum_{n=-\infty}^{\infty} \varepsilon_n a_n(t) = -\frac{\hbar^2}{2M} \frac{\partial^2}{\partial x^2} \sum_{n=-\infty}^{\infty} \varepsilon_n a_n(t).$$

The components of the series fulfill

$$i\hbar \varepsilon_n \frac{\partial}{\partial t} a_n(t) = \frac{\hbar^2}{2M} \frac{4\pi^2 n^2}{a^2} \varepsilon_n a_n(t).$$

After introducing the so-called Talbot time

$$T_T = Ma^2/(\pi\hbar)$$

the differential equation for $a_n(t)$ reads

$$i \frac{\partial}{\partial t} a_n(t) = \frac{2\pi}{T_T} n^2 a_n(t)$$

and the corresponding solutions yield

$$a_n(t) = a_n(t_0) \exp \left[-2\pi i n^2 \frac{t - t_0}{T_T} \right]$$

for the coefficients a_n and

$$\psi(x, t) = \sum_{n=-\infty}^{\infty} \varepsilon_n \exp \left[-2\pi i n^2 \frac{t - t_0}{T_T} \right] a_n(t_0)$$

for the wave function. When we chose the time t such that $t - t_0$ is an integer multiple of T_T , ψ simplifies to

$$\psi(x, t) = \sum_{n=-\infty}^{\infty} \varepsilon_n \exp[-2\pi i n^2 k] a_n(t_0) = \psi(x, t_0)$$

since $\exp[-2\pi i n^2 k] \equiv 1$.

For atomic waves not only the time but as well the distance plays an important role. The measurement takes place at a certain location. Therefore, we are interested in the length of free evolution. With the help of the de Broglie wave length $\lambda_{dB} = h/p$ we find

$$L_T = vT_T = \frac{vMa^2}{\hbar\pi} = \frac{2pa^2}{h} = \frac{2a^2}{\lambda_{dB}}.$$

We always assume a constant longitudinal velocity due to transformation into the time evolution of a 1D-problem. Therefore, the Talbot distance L_T and Talbot time T_T are connected by a constant. This means we can use distance and time equally.

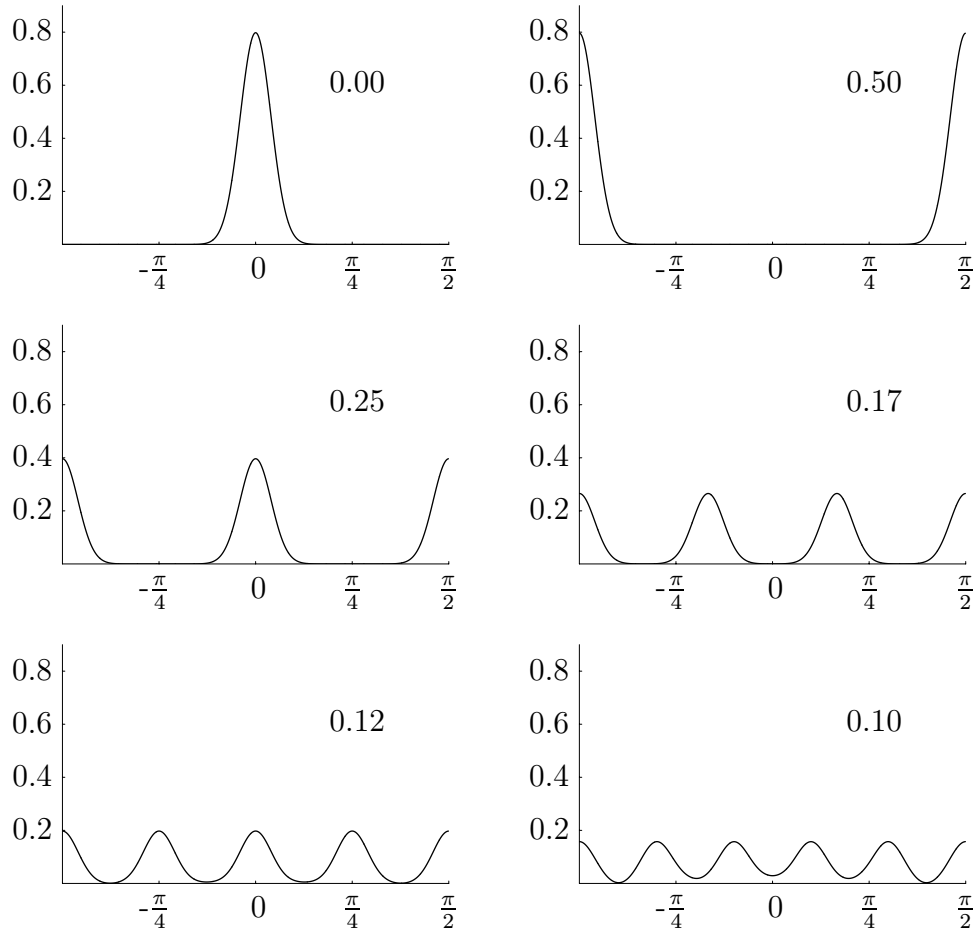


Figure 2.4: Fractional Talbot effect. The inserted number gives the fraction of time of the full Talbot time. $t = 0$ denotes the initial wave function. At $t = 0.5T_T$ we find the same shape but a phase shift of a half period. The other figures show the wave function at 1/4th, 1/6th, 1/8th and 1/10th Talbot time.

2.3.2 Fractional Talbot Effect

For our purpose the so-called fractional Talbot effect is more interesting. In the preceeding section we have seen that the Talbot effect leads to a repetition of a certain distribution by simple free evolution.

In Fig. 2.4 we take a closer look at the images of a fractional Talbot evolution. We consider a Gaussian located at the center of a periodic space with length π . The inserted numbers denote the passed time in units of the Talbot time T_T . The distribution at the half Talbot time $t - t_0 = \frac{1}{2}T_T$ is shifted by half a period. In an experimental setup this shift is irrelevant due to the periodicity. For this reason the half Talbot time is called Talbot time by some authors.

The other images show the distribution at different fractions of T_T . We recognize that for $t = T_T/2n$ we observe n equidistant peaks which are weaker due to normalization. Note that the width we observe remains the same as the initial peak. In the last picture we see that the individual peaks are no longer separated and start to overlap. This is a major restriction in constructing high periods with the fractional Talbot effect: We need sharp initial wave packets in order to obtain separated spots.

2.4 Focus and High Period

Now we combine both effects: focusing and the fractional Talbot effect in order to obtain sharp structures with a small period. Both effects have been seen in experiments whereas the combination remains a challenge.

2.4.1 A Historic Review

The combination of focusing and the fractional Talbot effect was originally suggested by Janicke *et al.* [20]. In this approach, the incoming atomic beam is represented by a nearly plane de Broglie wave and the diffracting structure is an off-resonant standing light wave as used in the focusing experiments. When we examine this approach numerically one problem becomes aware. Indeed, the atoms are focused after passing through the light field. Later, a number of fractional Talbot images of these original foci are observed. For these images a number of the initially focused peaks are superimposed. The copies are shifted by a fraction of the laser field period and hence, this yields a high repetition period. The fractional images, however, will only display clear foci when the individual imaged copies do not overlap [41]. For the plane wave focusing overlap cannot be avoided because of strong imaging aberrations and no clear periodic structure is observed for high-order fractional images. This

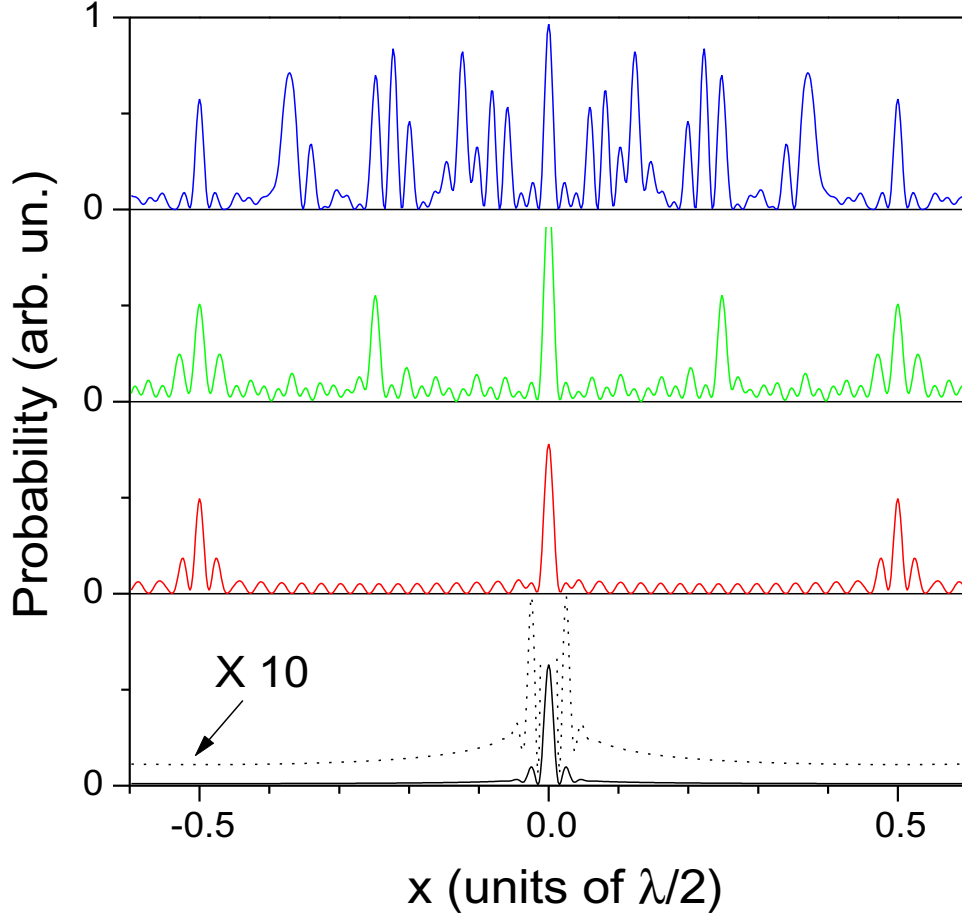


Figure 2.5: Plane wave focused. The bottom shows the best focus. The dashed line is magnified by a factor 10. The other graphs are disturbed distributions at $t = T_T/4, T_T/8$ and $T_T/16$. The noise originates from aberration.

is illustrated in Fig. 2.5, where for a plane atomic wave, focused by a standing light field, the probability distribution as a function of transverse position is shown in the focus plane z_f and at distances of one quarter the Talbot length $L_T/4$, $L_T/8$ and $L_T/16$, where fractional images with a period of $1/2$, $1/4$ and $1/8$ of the period of the diffracting standing light ($d = \lambda/2$) should be observed. The full range in transverse position in the figure is a .

The original focus (bottom curve) is quite sharp, with a full width at half maximum around 0.01λ . However, the background is not zero as shown in the $\times 10$ magnified curve. This is caused by the fact, that the standing wave

represents a sinusoidal phase grating for the atoms. Perfect focusing is only achieved with a parabolic phase variation. Near the nodes of the light field, where the atom phase has extrema, the sine square can be approximated by a parabola. Hence, atoms passing close to the nodes are focused to a well-defined spot. Atoms which do not pass close to a node, “off-axis atoms”, are not imaged to the same focus. This “sinusoidal aberration”, a close analogon to spherical aberration in light optics, results in the non-zero background. Hence, the non-overlap condition can never be fulfilled. The images at $L_T/4$ and $L_T/8$ still show relatively clear doubled and quadrupled images respectively, although the peaks are not equal in height and interference oscillations are observed in between the peaks. At $L_T/16$, the image is fully scrambled and no $a/8$ periodicity is discernible.

2.4.2 Beam Aperturing

In light optics, the main solutions to spherical aberration are the use of more complicated, aberration-corrected optics and the use of apertures to block far-off-axis light. For atom optics, the first solution is impractical. Aperturing, however, can be realized. The effect is illustrated in Fig. 2.6, where calculated atomic probability distributions are shown with an incident plane wave (on the right); with the incident atoms restricted by square apertures to the nodes of the light field (width of the apertures $\Delta x = 0.5d$) (center); and with incident “Gaussian beamlets” centered at the nodes with a root mean square width of $0.088a$ (left). The density plots of the two-dimensional probability distribution (with the propagation direction of the atomic wave shown vertically) show the characteristic “channel” or “quantum carpet” pattern discussed extensively in the literature [23,42]. Cross-sections through the distribution at $z = z_f$ and $z = z_f + L_T/20$ (see the dotted lines in the figure) are shown at the bottom and top of the figure. It is obvious that, while the quality of the focus does not differ markedly, the quality of the high-order Talbot image is dramatically improved with the use of apertures.

Both, hard-edged square and Gaussian apertures, can be realized experimentally. For square apertures, freestanding nanostructure transmission gratings with a period of 213 nm and slit widths around 100 nm, as would be needed for the chromium example, can be produced with relative ease at a number of facilities.

To obtain “soft-edged” Gaussian apertures physical transmission gratings are of course of no use. However, for metastable rare gas atoms, Gaussian apertures can be approximated with good accuracy by letting the incident atomic beam pass first through a separate standing light wave [1, 22, 27]. In this standing wave, tuned to an optical pumping transition, the atoms

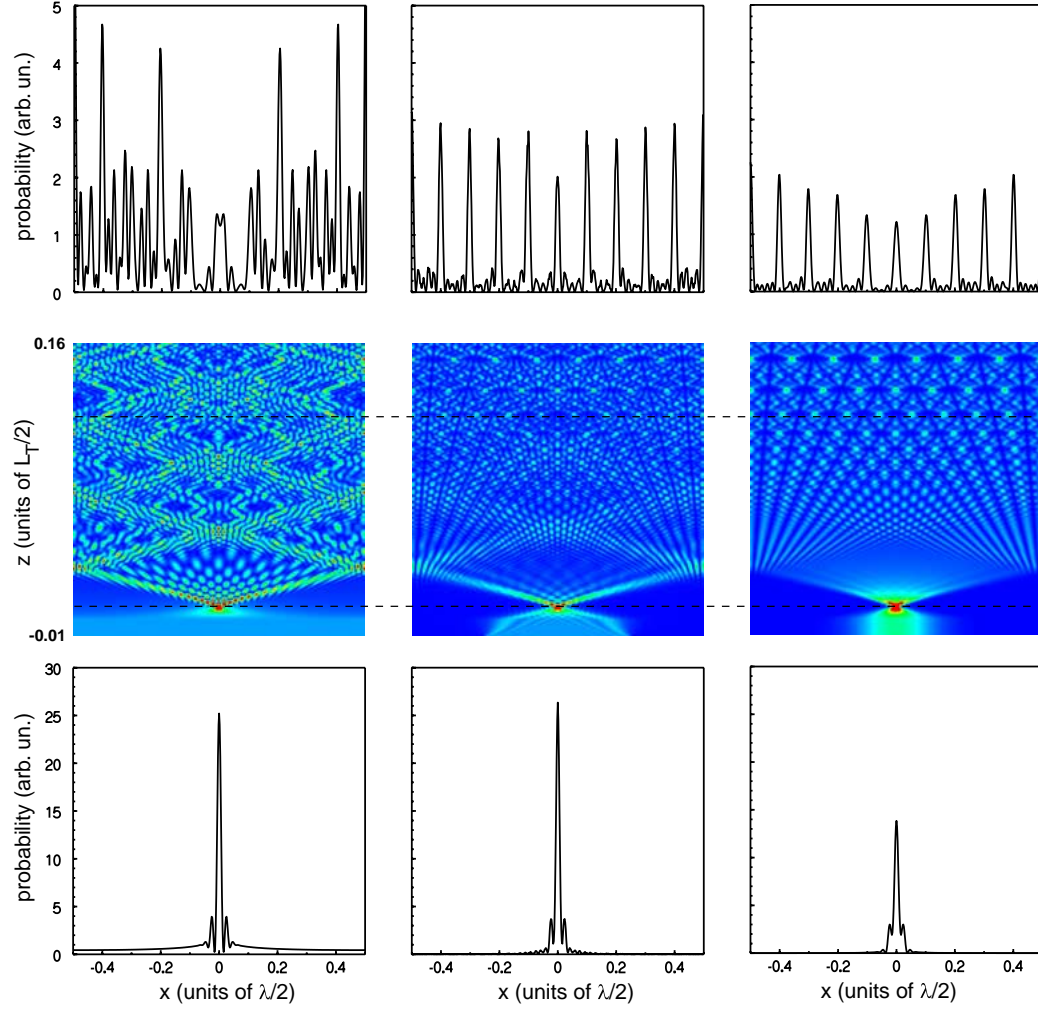


Figure 2.6: Comparison of preparation at focus plane and Talbot image. The left column shows the result using a simple plane wave. In the right column the initial beam has a Gaussian profile and the center uses simple gratings to block the disturbing atoms. The middle row shows a density plot for each. This is the time evolution of the probability distribution. The dashed line indicates the focusing plane. All the cuts at this plane show nice foci in the bottom row. But the cuts for the Talbot image at the full line shows a drastic difference.

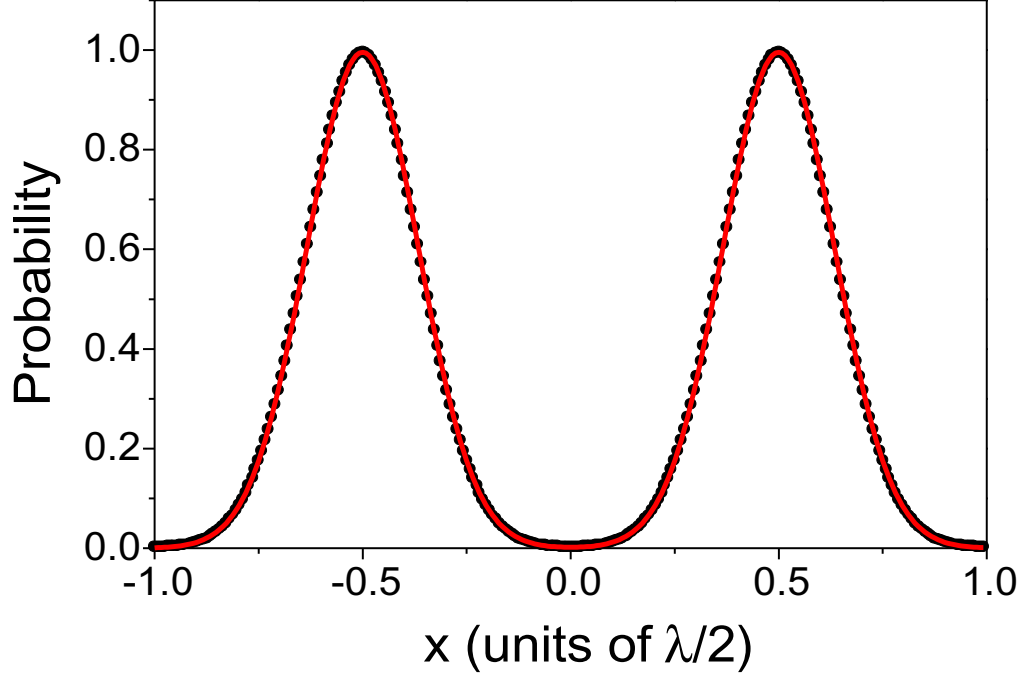


Figure 2.7: Comparison of damping result (dots) and a fitted Gaussian (solid). We find that the output of the damping method is a perfect Gaussian profile. Note, that this result is obtained by an approximation for the one level model.

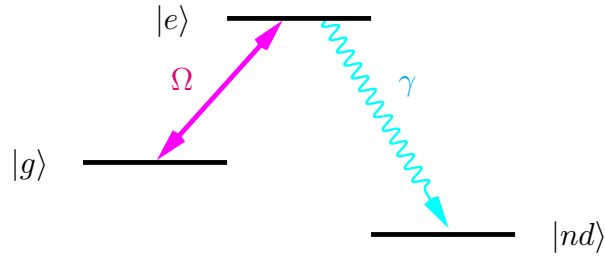


Figure 2.8: Level scheme of the atoms. The atoms are prepared in a metastable level $|g\rangle$. The laser field invokes the atomic transition to the excited state $|e\rangle$. Spontaneous emission back to $|g\rangle$ is neglected. The only decay is towards a nondetected level $|nd\rangle$ with a decay rate γ .

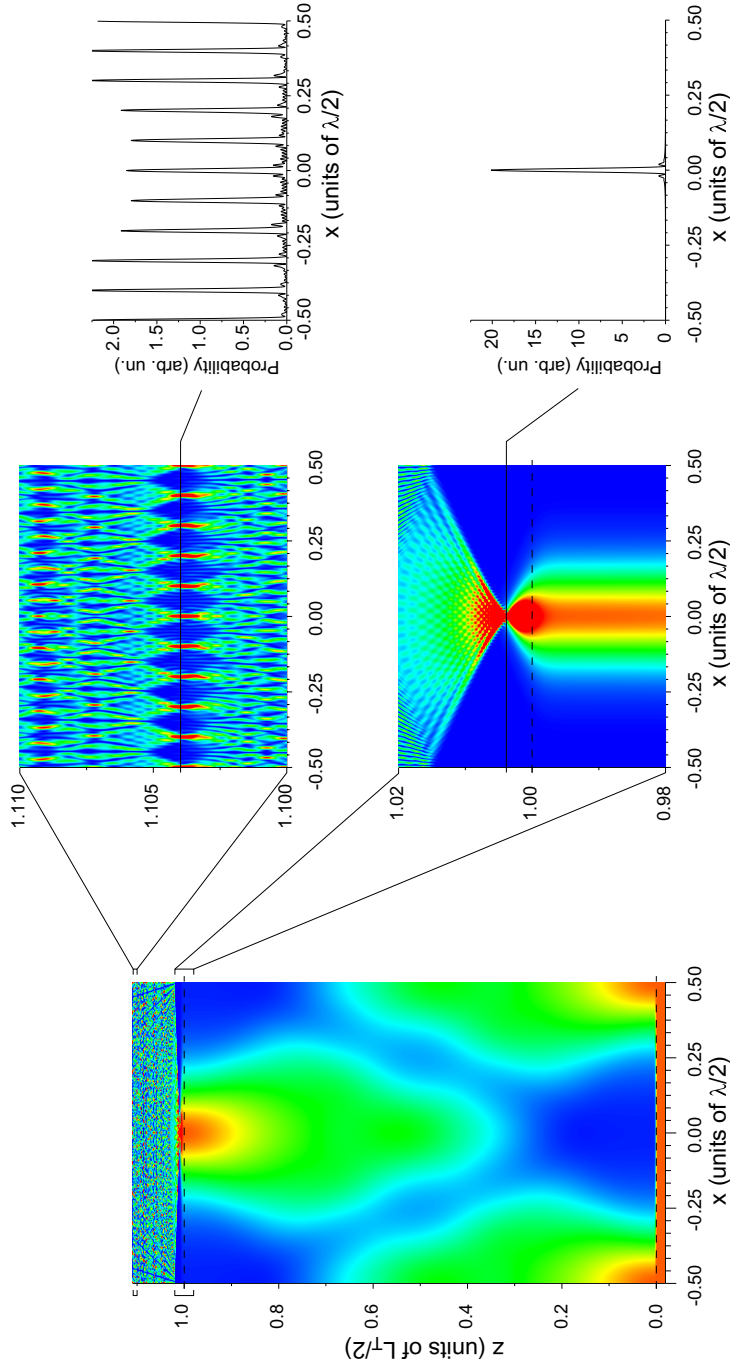


Figure 2.9: Full view on the Gaussian case. Gaussian profiles are produced out of a plane wave by damping near $t = 0$. At the Talbot distance there is the focusing laser. Both lasers are indicated by dashed lines. The zoomed images show the focus and the 10 times Talbot regime with the cross sections, respectively.

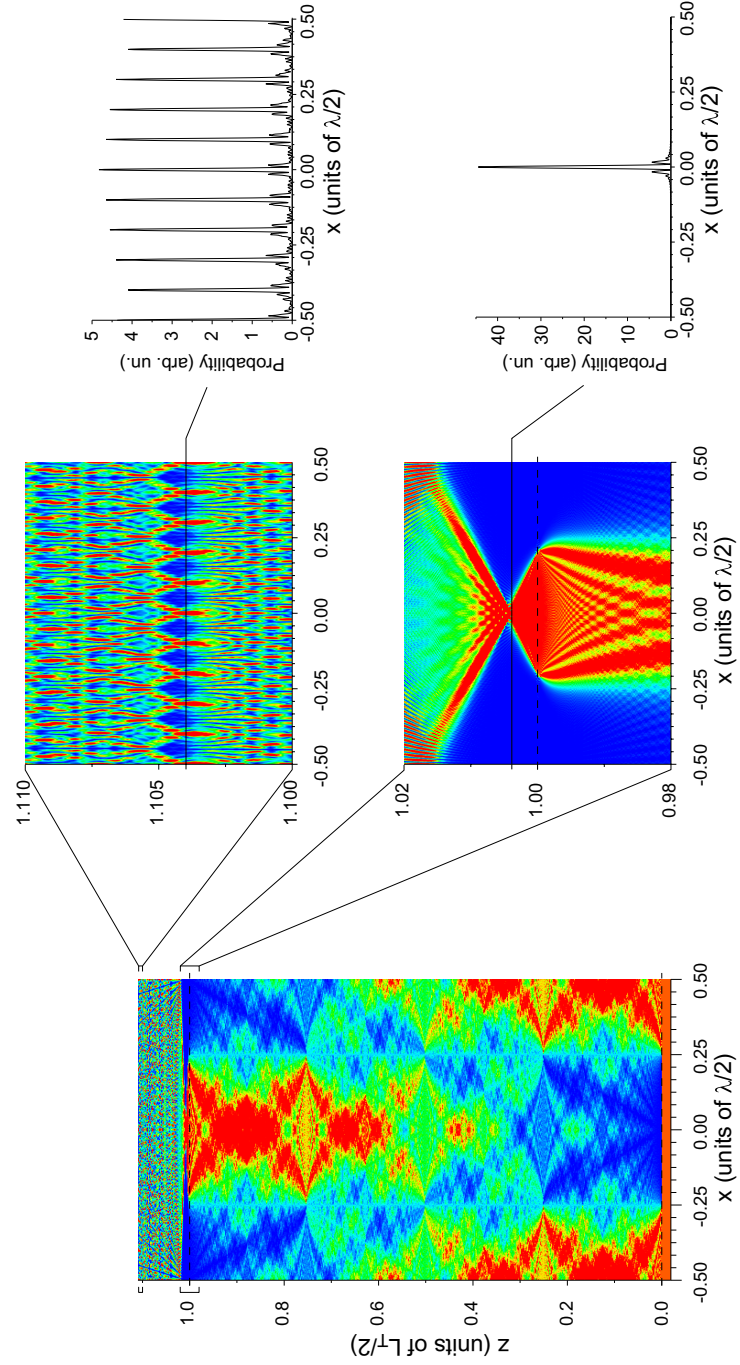


Figure 2.10: Full view on the rectangle case. The profile is set up by a grating. At the Talbot distance there is again the focusing laser. The zoomed images are marked by the small brackets whereas the cross sections are denoted by thin lines in the zoomed pictures.

are excited from the metastable state $|g\rangle$ to an upper level which decays preferentially to the atomic ground state shown in Fig. 2.8. This ground state $|nd\rangle$ is not detected. Thus, the atoms end up in the ground state except when they pass the standing wave near the nodes. Rare gas atoms in the inert ground state do not contribute to exposing the resist layer and hence can be neglected. The width of the “wave packets” of metastable atoms which pass the nodes can be adjusted with the intensity of the light wave and the interaction time. The transverse probability of the wave packets can be made close to Gaussian, as is illustrated in Fig. 2.7 where calculated and fitted Gaussian probability distributions are shown. The calculation is based on a similar numerical integration of the one-dimensional wave equation as before, including the spontaneous emission from the upper level of the transition to the ground state as a damping term.

The resonant light wave used for the optical pumping is relatively weak, just enough to saturate the transition. Because of this, the non-dissipative part of the interaction of the metastable atoms with the light wave is weak and does not cause appreciable focusing effects. For the focusing, an intense light wave can be used which is far detuned with respect to the same optical transition. By detuning, optical pumping can be suppressed while inducing strong focusing. For example, the parameters used in Figs. 2.5 and 2.6 can be achieved for (360 m/s axial velocity) metastable argon atoms on the $\lambda = 706.9$ nm transition with a laser power of 35 mW in a Gaussian beam with a waist of $18\text{ }\mu\text{m}$ and a detuning of 23 GHz. The probability for optical pumping will then be less than 2.5%.

In principle, the difference in wavelength between the resonant optical pumping light field and the off-resonant focusing field causes a mismatch between the periods of the incident array of Gaussian beamlets and the focusing array. However, even at 23 GHz detuning the relative mismatch is only 8×10^{-5} . Hence, a few thousand periods of the focusing field can be supplied with Gaussian beamlets positioned at the nodes with acceptable tolerance.

In practice, positioning a mechanical grating immediately in front of the focusing light field is difficult. Since after the grating, the initially square wave packets spread quickly because of diffraction, this means that the atoms cannot be restricted to the nodes of the focusing field. For the optical pumping approach, the same problem exists: If the distance between the optical pumping field and the focusing field is too short, overlap between the light fields results in unwanted interference effects. The problem can be solved by separating grating and focusing field (or the two light fields) by an axial distance $z = L_T/2$. At this distance, a Talbot image of the original wave packets is produced which has the same periodicity as the original one, but is

shifted by half a period. Using a mechanical transmission grating or optical pumping leads to the full diffraction patterns shown in Figs. 2.9 and 2.10 respectively. The positions of the light waves and gratings are indicated in the figure. The area near the focus ($z \equiv z_f \approx 1.004 L_T/2$) and an area near $z = z_f + L_T/20$ (indicated by brackets) are depicted enlarged at the bottom of each figure, the latter region illustrating the fractional Talbot images at $L_T/20$.

To get the result shown in Fig. 2.10 experimentally, we use metastable argon atoms with 360 m/s axial velocity and a laser beam with a Gaussian waist radius $w_l = 25 \mu\text{m}$ near-resonant with the $\lambda = 811.5 \text{ nm}$ two-level transition, but with a larger laser power and detuning than in Fig. 2.5 (14 mW at $\Delta\nu = 44 \text{ GHz}$). This leads to somewhat stronger focusing. For Fig. 2.9, where optical pumping is used to produce near-Gaussian beamlets, the weaker optical transition at $\lambda = 706.9 \text{ nm}$ requires even larger power and detuning (260 mW at $\Delta\nu = 45 \text{ GHz}$) as well as a smaller laser beam ($w_l = 25 \mu\text{m}$).

The dashed lines in the figures indicate the positions of the two laser beams or, in the grating case, the mechanical transmission grating and the laser beam at $z = 0$ and $z = L_T/2$. The probability distribution as a function of x in the focus plane and at $z = z_f + L_T/20$ is shown at the right in the figures.

2.5 Demands on Atomic Beam

2.5.1 Beam Collimation

In a real experimental setup, the perfectly monochromatic plane wave, assumed in the calculations above, cannot be realized. The atomic beam originates from a finite-sized source and is collimated with apertures. As a result, the beam can be described by an incoherent superposition of plane waves incident under all angles allowed by the collimation ratio of the beam. After passing through a regular structure, the Talbot image of each plane wave is simply projected under the angle of incidence of the wave and the associated probabilities have to be summed. In order for the high-order Talbot image to be retained under the summation, the spread in position of the individual images in the image plane has to be smaller than the distance between the peaks in the image. We will first look at the visibility of the image at $L_T/2$. With $L_T = 2a^2/\lambda_{dB}$ ($a = \lambda/2$ and $\lambda_{dB} = h/mv_z$, with m the atomic mass and v_z the (axial) velocity of the atoms in the beam), we can also express

the Talbot length as

$$L_T = \frac{\lambda^2 m v}{2h}. \quad (2.5)$$

At axial position $z = L_T/2$, the transverse spread in position of the images induced by an angular spread $\Delta\varphi$ of the incoming plane waves is $\Delta\varphi L_T/2$. Demanding that this spread is much smaller than the period $\lambda/2$ of the imaged pattern, we obtain

$$\Delta\varphi v_z \ll \frac{h}{m\lambda}. \quad (2.6)$$

As $\Delta\varphi v_z$ is equal to the spread in transverse velocity Δv_x and $h/m\lambda$ is equal to the single-photon recoil velocity of the atom, this condition can be written

$$\Delta v_x \ll v_{recoil}. \quad (2.7)$$

The collimation thus requires either a sub-recoil transverse laser cooling scheme or conventional collimation by slits. For a typical beam of argon atoms at $v_z = 360$ m/s, the required collimation evaluates to be $\Delta v_x \ll 0.02$ m/s or $\Delta\varphi \ll 6 \times 10^{-5}$ rad.

For the higher order fractional Talbot images, the axial position of the fractional image plane is $z = L_T/2n$ and the period of the image $\lambda/2n$. Hence, the same visibility condition (Eq. 2.7) is obtained. It is worthwhile to note, that the actual minimum size of the features as determined by the finite beam collimation becomes smaller as the order n of the Talbot image increases.

2.5.2 Spread in Axial Velocity

The Talbot length scales linearly with the axial velocity v_z . Therefore, for different axial velocities the axial positions of the fractional Talbot planes are different. The tolerance for the spread in v_z is determined by the depth-of-focus Δz_{dof} of the images, the axial distance over which the images are “sharp”. Here, we define Δz_{dof} as the full width at $1/\sqrt{e}$ height of the focal spot in the axial direction. We assume the depth-of-focus for our typical parameter set to be $\Delta z_{dof} \approx 4 \times 10^{-4} L_T$, independent of the fractional order of the image and equal to that of the original focus.

From the depth-of-focus, a limit for the spread in v_z which allows the observation of a fractional Talbot image at $z = L_T/2n$ without considerable image degradation is obtained:

$$\frac{\Delta v_z}{v_z} \leq 2n \frac{\Delta z_{dof}}{L_T}. \quad (2.8)$$

Equation (2.8) shows, that obtaining sharp images is easiest for high order images. Still, for the $\lambda/20$ period images, the allowed spread in axial velocity is only 0.4 %, which requires axial laser cooling of the atomic beam.

2.6 Conclusions

Focusing atomic beams using near-resonant optical standing waves as “micro-lens arrays” allows the production of regular nanostructures with dimensions on the order of a few nanometers. The fractional Talbot effect in the near-field diffraction pattern of the atoms behind the standing light wave can be used to produce nanostructures with a smaller spatial period than that of the standing light wave. However, when starting from a normal atomic beam, “clean” high-order fractional Talbot images do not appear due to aberrations of the micro-lenses. We have shown that either a physical transmission grating or optical pumping in a separate standing light wave can be used as lens aperture arrays for the atomic beam in order to effectively reduce the deviation due to aberrations. This allows high-order Talbot images to be used. The sample calculations that we have presented indicate that diffraction patterns with clean, separated peaks can be obtained with periods of $\lambda/20$. For our argon example, this amounts to a period of 41 nm; for chromium, to 21 nm. The demands on the incoming atomic beam are stringent, but within the range of laser-cooled atomic beam technology.

The laser power needed for the focusing is, for all considered atoms and transitions, not a limiting factor.

Chapter 3

Time-Dependent Detuning

We have met the detuning as a tool for damping or preparing atomic beams in the preceding chapter. Now we discuss a much more subtle role of detuning: In contrast to the last setup only one laser field acts on the beam of two-level atoms with an additional decay channel from the excited state. The laser field acts on the transition between ground and excited state and has a time-dependent detuning. We start either with red detuned and change to blue or vice versa. Both schemes include an area of resonance on the internal levels of the atoms. We find that the cases differ strongly. When we start with blue detuning the particles are gathered around the nodes of the laser field. The damping occurs at the antinodes. Hence, the potential scatters the atoms keep and they keep their acquired momenta. This effect creates a complicated structure in the carpet. In contrast, the change from red to blue detuning produces a quantum carpet with rather uninteresting design. In this scheme the particles are gathered in the regions of strong damping. The atoms with high transverse momenta decay through the excited state to a level which we do not detect. Therefore, these atoms do not contribute to the carpet structure.

3.1 Setup and Time Scales

We now analyze the dynamics of an atomic wave traversing a light crystal. As shown in Sec. 2.4.2 we use atoms with the Λ -level scheme depicted in Fig. 2.8. Moreover, we consider a Gaussian envelope with width $T > 0$.

The laser field E and the atomic center-of-mass motion are coupled via the atomic dipole d on the transition $|g\rangle \rightarrow |e\rangle$. The rate of spontaneous decay to the $|nd\rangle$ -level is γ . In the weak saturation regime $dE/\hbar \ll \gamma$ we can

describe the process by an effective Hamiltonian

$$H = \frac{p^2}{2M} + \frac{(dE)^2}{\hbar} \frac{\sin^2 kx}{\Delta(t) + i\gamma/2} \exp[-(t/T)^2]. \quad (3.1)$$

Here k denotes the wave number of the laser field. The time-dependent detuning

$$\Delta(t) = \Delta_0 \chi(t)$$

consists of a constant Δ_0 and a dimensionless function $\chi(t)$ with a change of sign at $t = 0$, that is $\chi(t) \cong t/\tau$ in the immediate vicinity of $t = 0$. The detuning rate Δ_0 is considered to be large compared to the damping rate $\gamma \ll |\Delta_0|$. Typically we assume

$$\chi(t) = t/\tau$$

or, in order to keep the detuning finite at $t \rightarrow \infty$, we choose $\chi(t) = \arctan(t/\tau)$.

For further considerations we focus on the regime with active damping. This happens within a characteristic time

$$t_0 = \frac{\gamma\tau}{2\Delta_0}$$

around $t = 0$. Note that we include the sign of Δ_0 into t_0 . This will be useful in the analysis in Appendix C.

With the help of this characteristic time we define three time zones: (i) In the early stage for $t < -|t_0|$ the detuning is large and the damping is negligible. Hence, the number of particles is conserved. The atoms are just distributed in the potential wells. (ii) Due to the vanishing detuning for $|t| < |t_0|$ the particles are in the damping zone. This region is quite small. Nevertheless, the time is sufficient for many atoms to be transferred into the nondetected level $|nd\rangle$. The particles reach quickly the third regime $t > |t_0|$. (iii) Now the detuning is large again but with the opposite sign. This moves the position of the potential minima. As before the damping vanishes and particle number is conserved.

3.2 Approximate Analysis

First we want to find some approximate analytical results. We study the interaction and mixing of two waves roughly corresponding to transverse momenta $\pm\hbar k$. Therefore, we solve the time-dependent Schrödinger equation and find coefficients describing the amplitudes of the two waves.

3.2.1 Mixing of Waves

We consider a simple function $\chi(t) = t/\tau$ which yields the detuning function $\Delta(t) = \Delta_0 t/\tau$. The Gaussian envelope is omitted since we discuss the regime $t \approx 0$. The solution takes into account mixing of the two waves with transversal momenta $\pm \hbar k + \delta p$, $\delta p \ll \hbar k$ mentioned in Sec. 1.1.2. For $\delta p = 0$ the beam falls under the Bragg angle into the field. Hence, δp plays the role of an angular deviation of the Bragg angle. The center-of-mass wave function for this approach has the form

$$\psi(x, t) = e^{i\varphi(t)} e^{-\Gamma(t)} \left[c_+(t) e^{i(1+\delta p/\hbar k)x} + c_-(t) e^{i(-1+\delta p/\hbar k)x} \right].$$

The first term only contains the phase which cancels when we calculate the modulus square of the probability distribution. From Appendix C we find the damping rate

$$\Gamma(t) = 2\lambda \left(\arctan(t/t_0) + \frac{\pi}{2} \text{sign} \Delta_0 \right) \geq 0$$

with the boundary conditions

$$\Gamma(-\infty) = 0 \quad \text{and} \quad \Gamma(+\infty) = 2\pi|\lambda|.$$

Note that we have included the sign of the detuning in t_0 . Hence, we have to consider the sign in Γ as well to keep the damping positive. This is an envelope over the whole experiment. The scattering is only visible in the coefficients $c_{\pm}(t)$. Here we introduced the notation

$$\lambda \equiv \left(\frac{dE}{\hbar} \right)^2 \frac{\tau}{4\Delta_0}.$$

The initial beam is a single plane wave. Hence, c_{\pm} have to fulfill the conditions

$$c_+(t \rightarrow -\infty) = e^{-i\delta t} \quad \text{and} \quad c_-(t \rightarrow -\infty) = 0$$

with the angular detuning $\delta = k\delta p/M$. From Eq. (C.6) we get the final result

$$c_{\pm}[z = \delta(t + it_0)] = -i\sqrt{\frac{\pi}{8}} e^{-\delta t_0} \left[e^{\pi\lambda/2} \sqrt{z} H_{\frac{1}{2}+i\lambda}^{(2)}(z) \pm e^{-\pi\lambda/2} \sqrt{z} H_{\frac{1}{2}-i\lambda}^{(2)}(z) \right]$$

where $H_{\mu}^{(2)}$ denotes the Bessel function of the 3rd type. In the coordinate we have included $\delta = k\delta p/M$ which plays the role of angular detuning.

The derivation holds true for $\delta \neq 0$. The case of $\delta = 0$ is investigated more carefully in the Sec. 3.2.3.

3.2.2 Asymptotic Behavior for $t \rightarrow +\infty$

In this limit we have to distinguish two fundamentally different cases: $\Delta_0 < 0$ and $\Delta_0 > 0$. First we assume $\Delta_0 > 0$. This includes two subcases $\delta < 0$ and $\delta > 0$. Again we start with the positive subcase, that is $\delta > 0$. Here, $\arg z$ changes from $-\pi$ to -2π for $-\infty < t < \infty$. Using the properties shown in Appendix C we find the results

$$c_+(t = +\infty) = e^{-i\delta t} \quad \text{and} \quad c_-(t = +\infty) = -2 \sinh \pi \lambda e^{-\delta t_0 + i\delta t}$$

and, hence the probabilities

$$W_+ = |c_+|^2 = e^{-4\pi\lambda} \quad \text{and} \quad W_- = |c_-|^2 = 4 \sinh^2 \pi \lambda e^{-4\pi\lambda} e^{-4\delta t}.$$

For $\delta < 0$ $\arg z$ changes from 0 to $-\pi$. As depicted in Fig. C.1(b) the splitting of the Bessel function is not possible. Hence, there is no scattering but only damping which results in

$$W_+ = e^{-4\pi\lambda} \quad \text{and} \quad W_- = 0.$$

If $\Delta_0 < 0$ the scattered wave vanishes for $\delta < 0$. Hence, the angular dependence shows a sharp asymmetry. The special case of $\delta = 0$ is the subject of Sec. 3.2.3.

3.2.3 Limit of Small Angular Detuning

The results of the preceding section are valid within the region $|\delta|, 1/|t_0| \gg 1/T$. The case $|\delta| \ll 1/T \ll 1/|t_0|$ can be described with the help of the perturbation theory.

To describe correctly the limit $\delta \rightarrow 0$ we introduce an envelope function

$$\lambda(t) \equiv \lambda \exp(-t^2/T^2).$$

Applying the perturbation theory for $|\delta|T \ll 1$ we find

$$W_-(\delta) \approx e^{-4\pi|\lambda|} [\sinh^2(\pi\lambda) + \delta T \text{sign} \Delta_0]$$

in first order for the parameter $|\delta|/T$. This results shows a linear behavior for the scattering probability in the vicinity of $t = 0$. The derivative of $W_-(\delta)$ with respect to δ depends on the sign of Δ_0 . Following from the behavior of $W_-(\delta)$ at $\delta \cong 0$ we find that the maximum of $W_-(\delta)$ is shifted depending on the sign of Δ_0 .

Hence, the angular dependence of the scattering probability owns a sharp asymmetry and includes two scales: $|\delta| \cong 1/t_0$ and $|\delta| \cong 1/T$.

3.3 $\Delta(t) = \arctan(t)$

Now we turn towards numerical calculations. For this purpose we introduce dimensionless variables. With the help of the recoil frequency

$$2\omega_R = \frac{\hbar k^2}{M}$$

we find the scaling relation

$$2\omega_R t = \tilde{t}.$$

Omitting the Gaussian envelope and introducing

$$kx = \tilde{x}$$

the Hamiltonian in scaled variables reads

$$H = \frac{\tilde{p}^2}{2} + \frac{A \sin^2 \tilde{x}}{\Delta(\tilde{t}) + i\gamma/2}.$$

Here

$$A = \frac{(dE)^2}{\hbar^2 2\omega_R \Delta_0}$$

denotes the scaled field intensity. Note, that we measure the rate of spontaneous emission γ and the detuning $\Delta(t)$ in units of Δ_0 .

The numerator of the potential is the standing wave. The denominator includes the detuning $\Delta(t)$ and the damping. The damping is realized with the spontaneous emission from the excited state to a nondetected level as shown in Fig. 2.8.

In this scheme we find the intuitive solution as shown in Fig. 3.1. In the off-resonant regime the particles are collected in the potential wells. This is clearly shown in the dark areas at time $t < 0$. In the short zone where the laser field is resonant with the atom the damping is active. The collecting force of the potential as well as the damping are proportional to the laser intensity A . In this parameter regime the particles are gathered at the zone of large damping. Therefore, most particles are lost.

In contrast, the damping is weak at the areas with low particle density. Behind the damping zone the particles which are left, stay in the new potential wells. Since the detuning changes the sign the new potential minima are shifted. Therefore, the particles which were not damped remain at their places. When the laser intensity decays the particles start to spread and interfere with neighboring wells.

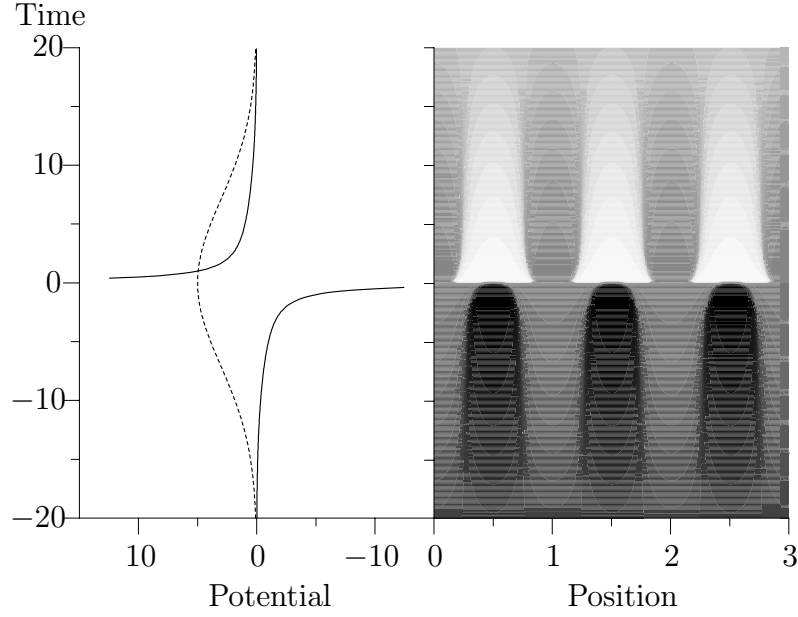


Figure 3.1: Density plot of the wave function for the detuning $\Delta(t) = \arctan(t)$. Here we have integrated the full Hamiltonian Eq. (3.1) with the scaled parameters $A = 1.0$ and $\gamma = 0.02$. On the left hand side we show the real part of the potential (solid) and the Gaussian envelope (dashed). The right hand side displays the density of particles. Dark denotes high probability, white is low probability. The particles are gathered in the potential wells. In the very small resonant area given by the dimensionless time parameter $\gamma\omega_R\tau/\Delta_0 \ll 1$ most particles are damped. With decaying potential the channels start to interfere.

3.3.1 A Close View on the Potential

To understand in detail how this potential acts on the atom beam we separate the potential

$$V(x, t) = \left[\frac{\Delta(t)}{\Delta^2(t) + (\gamma/2)^2} - i \frac{\gamma/2}{\Delta^2(t) + (\gamma/2)^2} \right] A \sin^2 x$$

into its real and imaginary part. The real part has the same sign as the detuning. Therefore, the potential minimum is shifted with the change of sign. Further one can see easily that the maximum damping occurs when the detuning $\Delta(t)$ vanishes.

Both effects, the collimation and the damping are proportional to the intensity of the field. Therefore, the antinodes play an important role. Damping is restricted to two conditions: The detuning is zero and the particle is near an antinode. This was seen in Fig. 3.1 when the particles in the low density regime are less damped.

3.3.2 Interpretation and Explanation

Fig. 3.2 shows all important quantities. The symmetric peak (blue line) is the imaginary part of the potential which is responsible for the damping. The damping only occurs in a small area around $t = 0$. Furthermore it is proportional to the strength of the laser field. The field intensity modulation is shown by the sin-functions. The bottom one represents the situation $t < 0$, the upper plot depicts $t > 0$. The thin line denotes zero. The sign of the \sin^2 function is taken from the real part which is drawn in the last curve including the change of sign.

In our case of $\Delta(t) = \arctan(t)$, the real part is negative for $t < 0$. Therefore, the potential minima are coupled to the antinodes of the standing laser field. Incoming particles are gathered at these antinodes and travel to the damping zone.

The damping is proportional to the imaginary part of the potential and proportional to the intensity of the laser. The potential is purely time-dependent whereas the laser intensity is purely position-dependent. Hence, the damping occurs at time $t \cong 0$ at the antinodes. Since the particles are collimated at the antinodes the damping and the collimation match and many particles are lost.

Those atoms which remain uncollimated and reach the damping zone at the nodes of the laser field are not damped. They stay and therefore the gray-level does not change in the damping region.

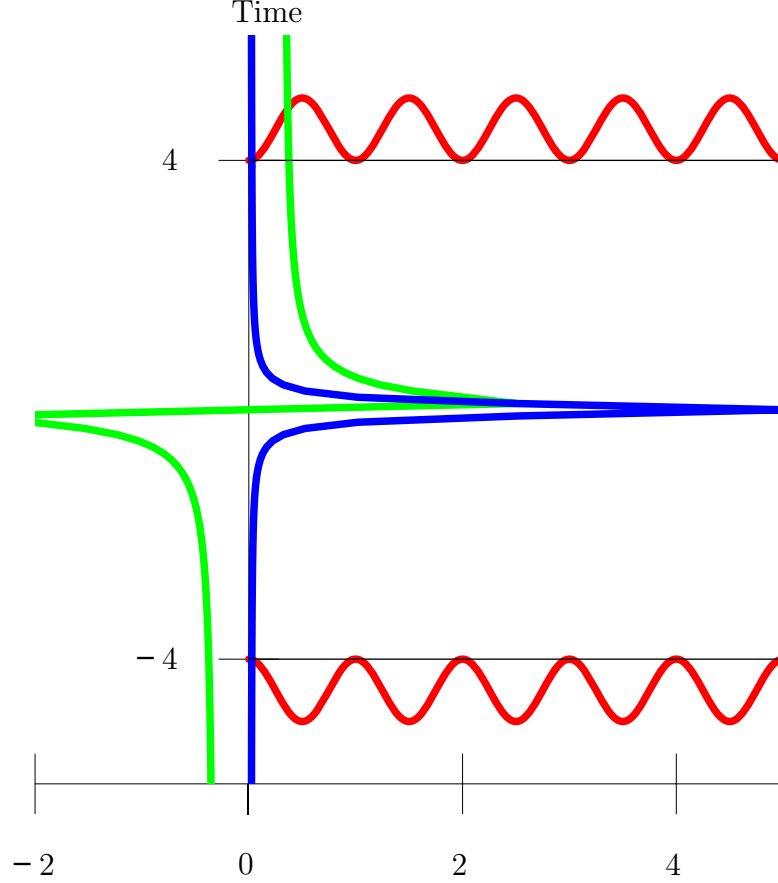


Figure 3.2: Real (green) and imaginary part (blue) of the potential and, the nodes and antinodes of the laser field (red). Since we concentrate on the time region $-5 < t < 5$. We can omit the Gaussian envelope. The thin horizontal black line denotes the zero-level of the laser field. Depending on the real part, the field points toward positive or negative direction at the antinodes. The direction is fixed by the detuning function. Note that the horizontal axis combines potential strength for the real and imaginary part. Further the numbers denote periods for the $\sin^2 x$. For the modulation only the sign is important. Hence, there are no values depicted for this function.

For $t > 0$ the real part of the potential has a negative sign. Therefore, the minima are at the nodes. The few particles which were in the damping region but were not damped start to move into the new wells. The majority of atoms which were not damped due to the passage at the nodes stay, since they are already at the minima of the laser field.

Note that the Gaussian rise and decrease are not included in Fig. 3.2. For the central region this does not play an important role. But the decrease makes the potential vanish. For this regime the particles start to spread and interference between atoms from different wells arises.

3.4 $\Delta(t) = -\arctan(t)$

Now we change our detuning function in the sign only: The change of sign at $t = 0$ is no longer from $-$ to $+$, but vice versa. On first sight one would expect that this is only a minor difference and the plots just show a shift. This does not hold true as a comparison between Figs. 3.1 and 3.3 displays in an impressive way.

3.4.1 Time Evolution of the Beam

Similar to the case $\Delta(t) = \arctan(t)$ the particles are gathered in the potential wells for $t < 0$. Note that the wells are now shifted. The potential minima are connected to the nodes, the maxima to the antinodes. The particles are collected at the nodes or places of low damping, respectively. Reaching the damping zone, white spots at low atomic density regimes arise. But the damping does not clean up the structure of the carpet. The opposite holds true. For $t > 0$ a complicated structure similar to the Talbot effect emerges. In this scaled units the Talbot length is 2π . This indicates that high transversal momenta are excited and the laser field is too weak to guide the particles.

We emphasize, this is not the original Talbot effect, since this requires free evolution. Nevertheless, the channels and periodic repetitions typical for the Talbot effect occur.

3.4.2 Analysis of the Potential

The peak of the imaginary part of the potential has the same shape and location as before. Since this is only important in the neighborhood of $t = 0$, we concentrate on the real part which is for $t < 0$ positive. Therefore, the antinodes of the potential mark the maxima and the nodes represent the

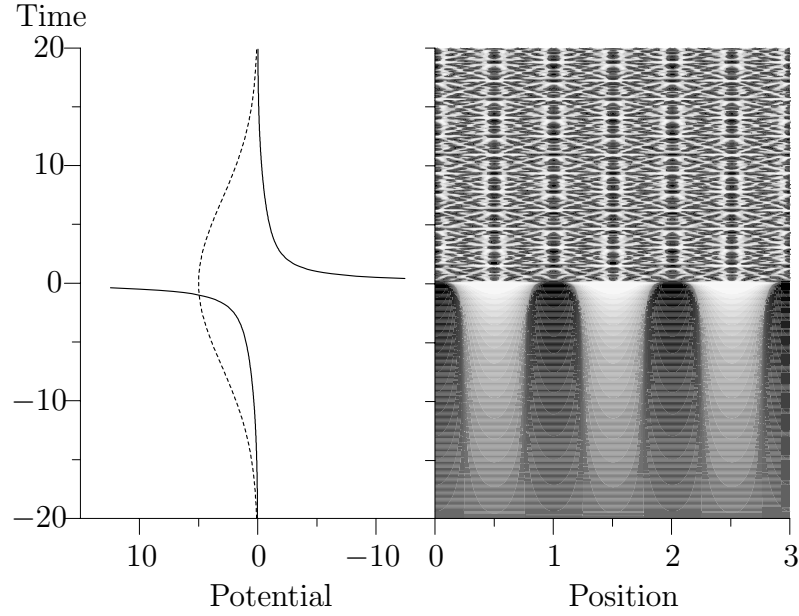


Figure 3.3: Density plot of scattered atoms of the detuning $\Delta(t) = -\arctan(t)$. The parameters are $A = 1.0$ and $\gamma = 0.02$. The left hand side shows the real part of the potential (solid) and the Gaussian envelope (dashed). The right hand side displays the density of particles. As before, dark denotes high probability, white is low probability. For $t < 0$ the particles are gathered in the potential wells. Note that the wells are shifted. But from the damping zone on we find a completely different solution: Fine structures appear. Moreover, no wells for $t > 0$ are visible.

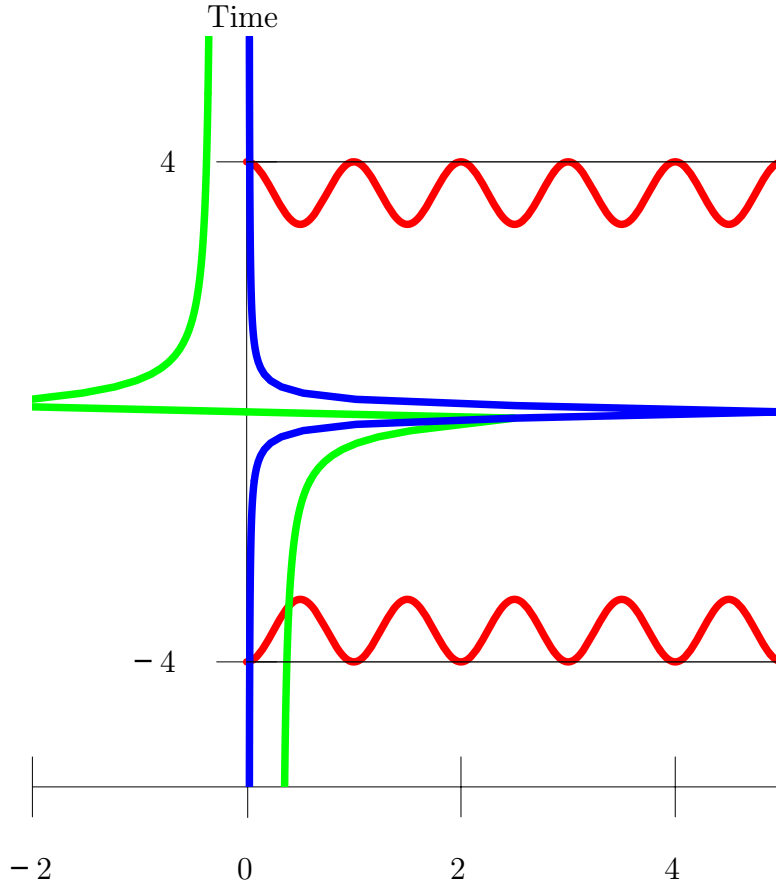


Figure 3.4: Real (green) and imaginary part (blue) of the potential as well as the nodes and antinodes of the laser field (red). The vertical t -axis is marked by “Time”. For the potential the numbers on the axis denote arbitrary units whereas for the laser modulation the numbers indicate periods. The thin lines denote for the $\sin^2 x$ the zero-level, depending on the time. The laser field amplitudes at the antinodes are positive or negative depending on the sign of the detuning function. The Gaussian increase and decay are omitted. Similar to Fig. 3.2 the horizontal axis combines potential values and periods for the modulation function.

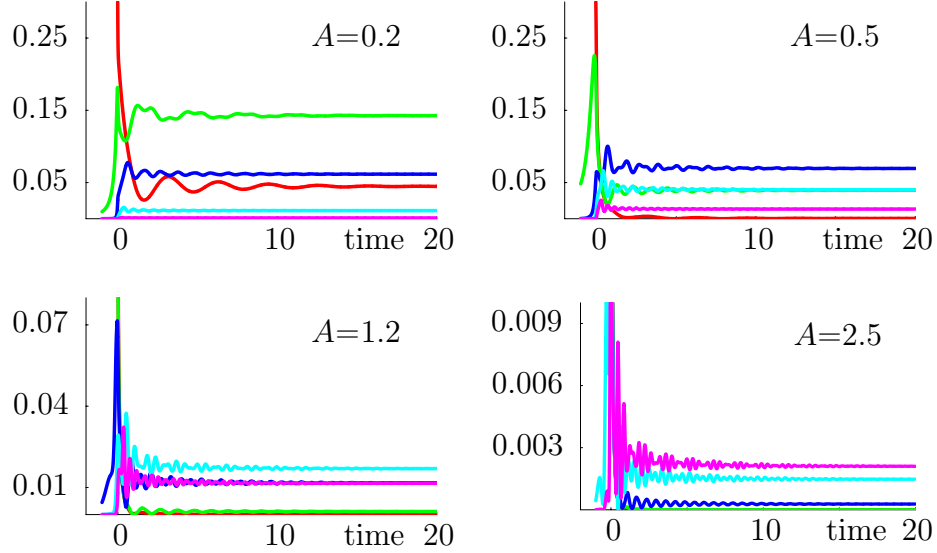


Figure 3.5: Time evolution of occupation of momenta for different intensities. The colors denote the momenta: $p = 0$, $p = 2\hbar k$, $p = 4\hbar k$, $p = 6\hbar k$ and $p = 8\hbar k$. With increasing intensity the highest populated momentum moves to higher momentum states.

minima. The large detuning disables the damping and the atoms move into the potential wells near the nodes.

When we reach the interaction zone the damping rises. But since the damping is proportional to the intensity, at the nodes is no damping. The places of collimation and damping are shifted against each other. The damping occurs at the places of low atom density whereas the collimation guides the particles to regions of low damping.

In contrast to Sec. 3.3 now damping and collimation are separated. In the preceding section the particles were gathered and damped together. The force of the real part accelerated the atoms but they were damped immediately. Therefore, the probability to find higher momenta is negligible.

In the current case the atoms acquire a transversal momentum by a kick from the potential. This kick arises from the peak of the real part of the potential as shown in Fig. 3.4. Note, that the derivative of the real part is huge and therefore high momenta could be achieved. Since the damping around the particles is weak they keep the momenta and we can measure this outside of the potential.

3.5 Quantum Kicks

We have seen in the preceding sections that the sign in the detuning is very important to select transversal momenta. So far we just know that we need the detuning $\Delta(t) = -\arctan(t)$ from Sec. 3.4 to produce atoms in high transversal momentum states. The question is now if we are able to choose the momentum. Can we perform coherent control or do state engineering of momentum states?

In Fig. 3.5 we show the time evolution of the probabilities for various momenta and different laser intensities. For $A = 0.2$, which is a quite weak potential, only low momenta are excited. The most populated state is $p = 2\hbar k$. The second most populated states at the end of the interaction are the initial state $p = 0$ and $p = 4\hbar k$. All other states do not play an important role since the energy of the field is too weak to push the atoms into higher states. Note the symmetry $p_n = p_{-n}$. The total number of scattered atoms is the double of the plotted probability.

Increasing the intensity to $A = 0.5$ leads to a maximum population in the $p = 4\hbar k$ -state. It is difficult to see in Fig. 3.5 that the states $2\hbar k$ and $6\hbar k$ are equally populated. Note, that maximum probability has decreased from approx. 15% to 7%.

When the laser power rises up to $A = 1.2$ the effect continues. The maximum can be found for $p = 6\hbar k$ but only at a level of 2%. Again two levels have almost the same probability, $4\hbar k$ and $8\hbar k$ have similar amplitudes.

From $A = 2.5$ on the maximum has a quite high momentum but the probability to find this excited state is only about 0.3%.

Finally we can summarize that we can choose the transversal momentum state which is populated maximally. But since the damping is proportional to the intensity of the field the damping increases with rising field. Therefore, the probability to find the chosen state reduces as well.

3.6 Experimental Realization

Finally we want to propose an experimental setup. The difficulty lies in the change of the detuning. It is very complicated to modify the detuning of a laser correlated to the velocity of the atomic beam. To solve this problem we suggest a trap. The whole experiment can be done in a trap. A longitudinal velocity is not necessary. Hence, we just switch on and off the laser field.

Parallel to the light the detuning is controlled via a magnetic field. Using the Zeeman effect we adjust the energy distance between the atomic levels which are affected by the laser. Hence, we change not the detuning at the

laser but at the atoms. The magnetic field can be easily varied and since the atoms have no longitudinal velocity v_z we just combine the intensity of the laser and the magnetic field.

The distribution is measured via pictures of a CCD camera. Note that we are only interested in the atoms in the ground state. Therefore, we have to illuminate those atoms and take the picture. This measurement destroys the distribution and we have to repeat the experiment. The alternative is to switch off the collimation lasers of the trap and wait for the free evolution to represent the momentum distribution.

Chapter 4

The Beam-Splitter

In this chapter we apply a longitudinal modulation to the laser field. This modulation is resonant to the Doppler frequency and is used to scatter the atoms in transversal direction. The modulation is created by crossing two laser beams under a small angle. Hence we assume for the whole field the same envelope as for both individual beams. We investigate the effects of the laser intensity and the crossing angle.

4.1 Model of a Light Crystal

The light crystal is formed by two standing laser fields crossing each other at a small angle θ . Both laser beams have the same wave number k and Gaussian envelopes with width L . Hence the resulting light field has the form

$$E(z, x, t) = E e^{-z^2/L^2} \cos(k_z z) \sin(k_x x) e^{-i\Delta t} + c.c., \quad (4.1)$$

where $k_x = k \cos \theta/2 \approx k$, $k_z = k \sin \theta/2 \approx k\theta/2$. Again, Δ is the detuning of the laser frequency from the resonant atomic transition $|g\rangle \leftrightarrow |e\rangle$.

As in the preceding chapters, we consider a monochromatic beam of atoms with a longitudinal velocity $p_z/m = v_z \equiv v$ which traverses a region where the atoms interact with a standing light field. The velocity v is assumed to be large enough so that it remains approximately constant during the interaction. Consequently we can consider the time evolution of a 1D-problem. The laser field and the atomic center of mass motion are coupled through the atomic dipole d on the transition $|g\rangle \leftrightarrow |e\rangle$.

In the weak saturation regime, $dE/\hbar \ll \Delta$, the dynamics of atomic waves is governed by a nonstationary Hamiltonian

$$\hat{H} = \frac{\hat{p}^2}{2M} + \frac{(dE)^2}{\hbar\Delta} e^{-(\tau/T)^2} \cos^2(\omega_D \tau) \sin^2 k\hat{x} \quad (4.2)$$

with an effective (optical) potential for the ground state atoms.

The basic new feature of our model is the longitudinal modulation of the light crystal which manifests itself in two terms entering the effective potential Eq. (4.2): (i) The Gaussian envelope whose width $T = L/v$ is assumed to be large so that the overall intensity changes quite slowly, and (ii) the time dependent modulation with the Doppler frequency $\omega_D = k\theta v/2$ given by the squared cosine dependence.

The latter is physically most interesting since it can significantly alter the properties of the potential during the interaction. In particular, when the frequency $2\omega_D$ is close to the separation $\varepsilon_{\text{tr}}(n) - \varepsilon_{\text{tr}}(n-1)$ of the transversal kinetic energy

$$\varepsilon_{\text{tr}}(n) = \frac{(2n\hbar k)^2}{2M}$$

the ‘‘Doppleron’’ [28] resonance occurs. Note, that from a mathematical point of view the potential is not separable and a closed form expression for the solutions is difficult to find. However, in certain physically interesting regimes approximate solutions can be given.

By introducing dimensionless variables $kx \rightarrow x$, $2\omega_R\tau = t$, where $\omega_R = \hbar k^2/(2M)$ is the recoil frequency, we transform the Schrödinger equation using the Hamiltonian Eq. (4.2) into the form

$$i\frac{\partial\psi(x,t)}{\partial t} = -\frac{1}{2}\frac{\partial^2\psi(x,t)}{\partial x^2} + Af(t)\sin^2x\psi(x,t), \quad (4.3)$$

with the definitions $f(t) = \exp[-(t/T)^2]\cos^2(\omega_m t)$, $A = (dE)^2/(2\omega_R\hbar^2\Delta)$, $T = 2\omega_R L/v$, and $\omega_m = \omega_D/(2\omega_R)$.

For moderate amplitudes without the additional longitudinal modulation the potential does not attract too much interest. In this case the normal incident wave, for instance, is adiabatically guided into the medium and changed gradually. The atomic wave is channeled through the crystal via the valleys and after the potential goes back to zero the modulation effect is reversed. As a result, the outgoing atomic wave is not affected by the light crystal. The additional modulation breaks the adiabaticity of the crystal. The crystal can be viewed as a sequence of pulses of different amplitude, which acts on the atomic wave. Already for a moderate modulation frequency, $\omega_m \sim 1$, each change of the potential intensity is fast and hence, we expect a significant change of the atomic wave.

The free parameters in this model are the crossing angle θ which enters our calculations via the modulation frequency ω_m and the intensity of the fields.

We emphasize that it is not necessary to perform the experiment with two standing waves. It might even rather difficult to realize this experimentally.

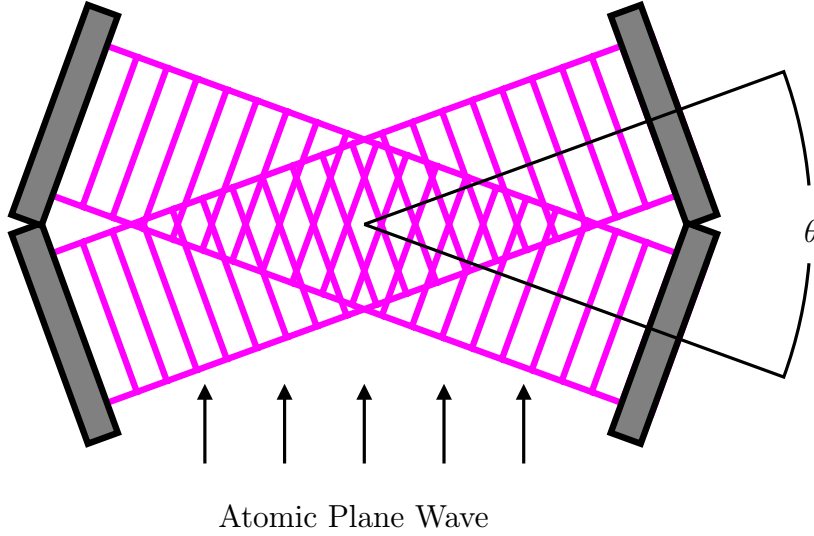


Figure 4.1: Setup of laser field. Two standing laser fields with transverse Gaussian envelope enclose an angle θ . Since the angle is small we assume a common Gaussian for the superposition. The angle defines an additional modulation on the envelope as shown in Eq. (4.2).

However, in a magneto-optical trap the setup is simpler. We need only one beam and the crossing angle can be realized by changing the intensity.

4.2 A Feeling for Parameters

First we want to see what effect results from a change of our parameters. Therefore, we start with the simplest case $\omega_m = 0$, which means we that we have no angle enclosed between the lasers and hence, no modulation. We then increase θ and thus introduce the modulation. In the next step we increase the laser intensity.

4.2.1 No Modulation

First we investigate the simple case of no longitudinal modulation, that is $\omega_m = 0$. The particles just feel an off-resonant laser field rising and decaying. The intensity of the potential is weak. We are in the regime of the Raman-Nath approximation. Hence, the particles glide into the potential wells but are not scattered. No momentum transfer is observed. With the lowering of the field the particles immediately occupy the whole space and no effects

of the earlier scattering phenomenon survives. This situation is shown in Fig. 4.2 which consists of three parts. The area denoted by “Position” covers the time evolution of the position wave function squared over three periods, and a density plot for $-20 \leq t \leq 20$. Dark represents high probability to find the atom at this point whereas white indicates a low probability.

In the “Potential” column we show the maximum of the potential. Since the potential is modulated in x-direction with a $\sin^2 x$, we depict the potential at an antinode to display the rise and decay.

The right columns described by “Probability” show the evolution of the probability to find the atoms in the transversal momentum state $p = 0$. This is a straight line. The probability to find the atoms in the originally prepared state is constant. Hence, no scattering occurs. Since the probability is unity for all times there is no occupation of other transverse momentum states.

The potential changes slowly which corresponds to a small derivative of the potential. Since the force is the derivative of the potential there is a negligible force on the particles and hence, no momentum transfer.

4.2.2 A Touch of Scattering

We now apply the same weak potential as before but the two laser beams enclose a nonvanishing angle in order to get the modulation frequency $\omega_m = 0.3$. In the middle column of Fig. 4.3 we see that the Gaussian envelope of the potential is modulated by $\cos^2(\omega_m t)$. In the density plot we find a clear spatial separation of the particles. As soon as the potential vanishes the particles spread immediately. Since this occurs only at a very short period of time the particles are pushed back to their old positions very rapidly yielding a chessboard-like structure.

In addition to the move towards potential minima we observe the rapid change of the potential. This change causes a large derivative in the potential and thus a strong force. The force is large enough to scatter at least a few particles. In the momenta probabilities we observe for the initial state dip. The total amount of scattered atoms is small and since there is only one small rising peak at $t = 0$ we find that only the lowest states $p = \pm 2\hbar k$ are occupied. Note that the left momentum graph denotes the identical probabilities for $2\hbar k$ and $-2\hbar k$. Since both graphs are identical due to symmetry we observe only one. There is no damping included. Thus the total probability is constant. All particles which are scattered from the original state are transferred into the $\pm 2\hbar k$ states.

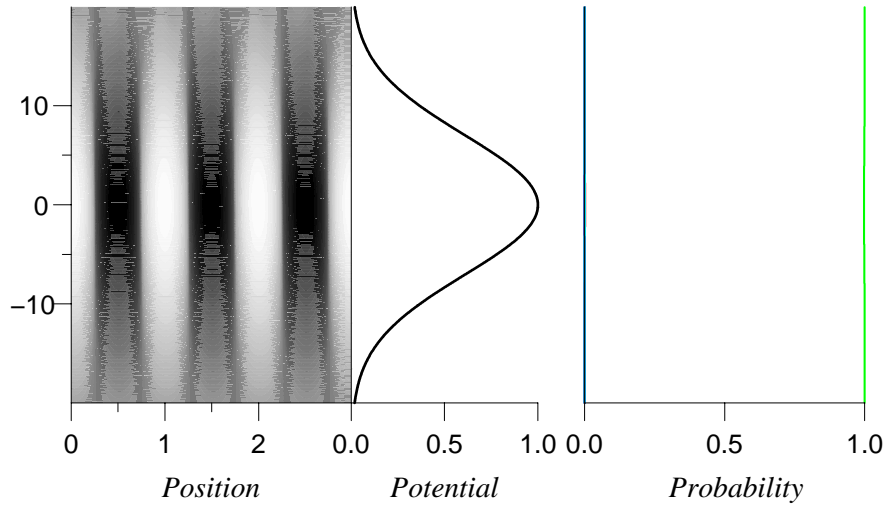


Figure 4.2: Time evolution of position and momentum for $\omega_m = 0$. The left column displays a density plot of the position wave function. In the middle the time dependence of the potential is depicted by the envelope. The right diagram presents the probability of finding the particle in the transversal momentum state $p = 0$. Since this probability P is unity the particle does not occupy any other momentum state. Moreover, no scattering has taken place during the transit through the field.

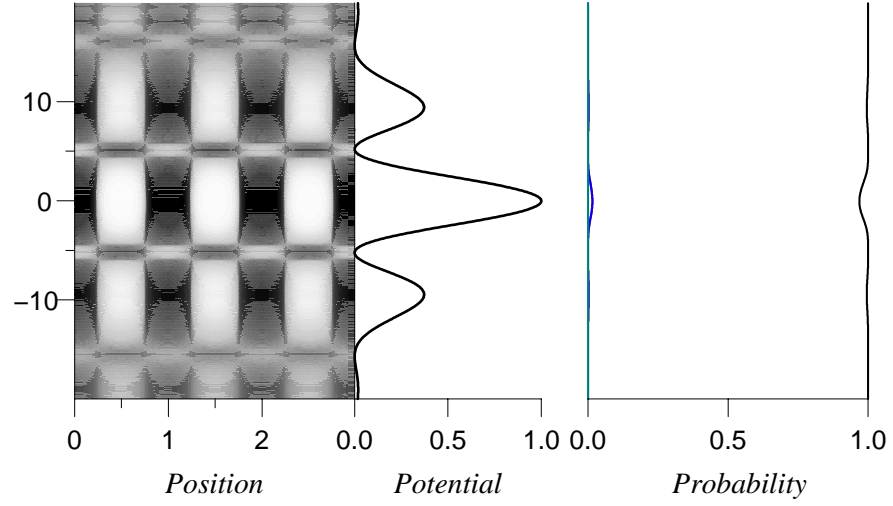


Figure 4.3: Time evolution of position and momentum for $\omega_m = 0.3$. The small modulation already breaks the adiabaticity. We find traces of scattering in the momenta probabilities. The rapid change of the potential acts like a kick on the particles and transfers some of them into the $2\hbar k$ -state. Therefore, a chessboard-like structure is observed. Moreover, from the position density plot we recognize that the atoms spread over the whole space as the potential vanishes.

4.2.3 Result of Modulation

We have seen that the angle enclosed between the lasers rules the modulation of the Gaussian envelope. If there is no modulation, the change of the potential is adiabatic and therefore no scattering occurs. Scattering occurs when the modulation breaks the adiabaticity. The key point is the rapid change of the potential. Here the modulation plays an important role since the $\cos^2 \omega_m t$ part changes the envelope from the Gaussian value immediately to zero. Certainly an appropriate intensity is required.

4.3 Effect of Intensity

In the preceding section we have analyzed the effect of the modulation. Now we want to investigate the impact of the field intensity. To find scattering we have to apply a modulation which we choose the resonant Doppler frequency $\omega_m = \omega_D/(2\omega_R) = 1.0$. This modulation is fixed throughout the whole section.

4.3.1 Introduction of Iterative Scattering

The intensity enters our model in the parameter A . We start with a quite weak field at $A = 0.5$. Due to large interaction time, $\omega_R \tau \gg 1$, the Raman-Nath approximation is no longer valid as we see in Fig. 4.4.

The first impression is the chessboard structure in the density plot. Due to the strong modulation the stripes have a similar length. But this we have seen already in Sec. 4.2.2. From the time evolution of the momenta probabilities we see a continuous scattering. The probability to find the particles in the initial state of no transversal momentum decreases step by step. We find that the steps are connected to the raise or decay of the potential. Note, that the rising probability graphs are two identical graphs for $p = \pm 2\hbar k$. Behind the interaction zone only 50% of the particles are left in the initial state. All the rest is scattered. Note that only the two additional levels $\pm 2\hbar k$ are occupied. The energy is not sufficient to transfer the atoms into higher transverse momentum states. Due to the absence of damping about 25% are in each of the two first excited states.

4.3.2 Enforced Scattering

Since only the first momentum state could be reached till now, we increase the intensity further. The new field strength should still be too weak for

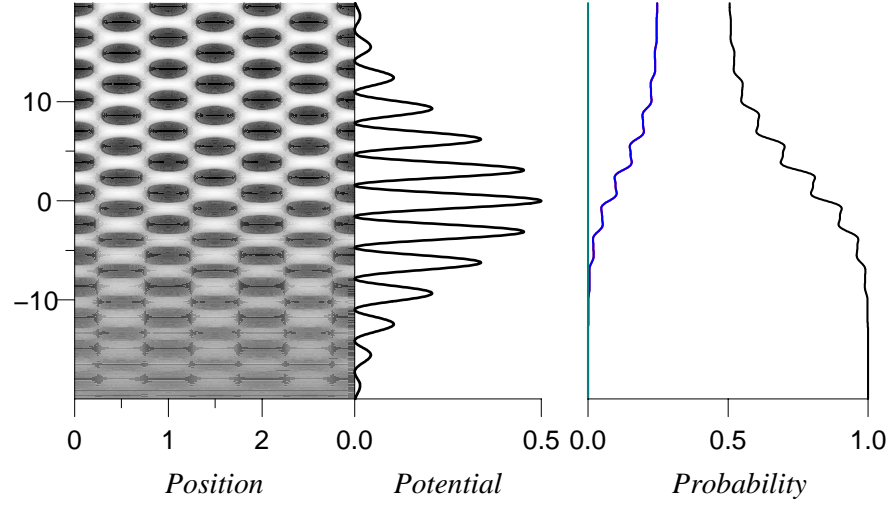


Figure 4.4: Time evolution of position and momentum for $\omega_m = 1.0$. We apply a weak potential with $A = 0.5$. Note that this potential is only half in size compared to the ones of Figs. 4.2 and 4.3. The strong modulation breaks the adiabaticity. The fast change of the potential kicks the particles. Since we have a series of kicks a stepwise transfer pushes more and more atoms into the scattered level. As the potential is weak only about 50% of the atoms are transferred. This results in a chessboard-like structure in the density plot.

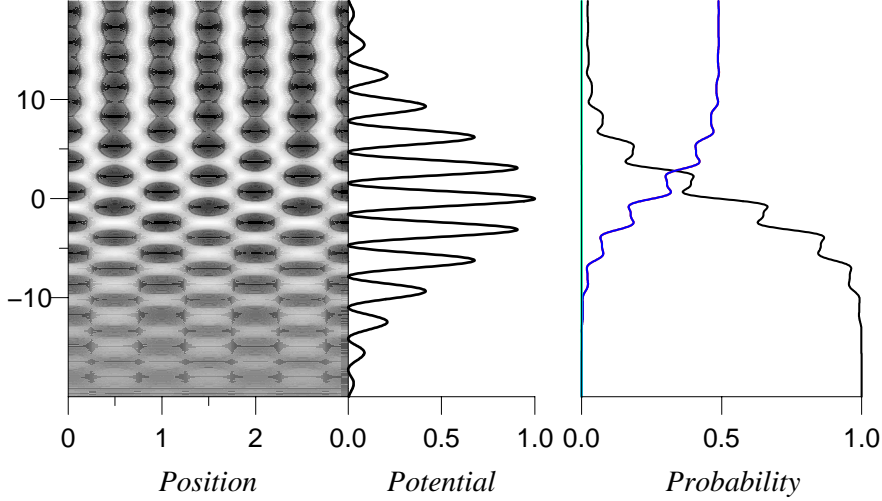


Figure 4.5: Time evolution of position and momentum for $\omega_m = 1.0$. We apply a moderate potential with $A = 1.0$. The kicks now transfer most of the atoms into the scattered level. The potential is weak enough so that only one level is populated. At the end of the interaction zone we find the particles mainly in the $2\hbar k$ state (blue) and therefore the density plot shows two peaks per period in position space.

pushing to higher levels. Our first goal is to push almost all particles into the $p = \pm 2\hbar k$ state.

In Fig. 4.5 we see two major differences. First, the areas of high probability in the density plot start to overlap. Secondly, the position wave function now has two maxima per period. This doubling is similar to the situation at a beam splitter. We define quality by the ratio of maximum and minimum of the position wave function. In the probability picture we find only few particles in the original state. Hence, in the final stage almost all atoms are transferred into the state $\pm 2\hbar k$. The approximate probability distribution for times $t > 20$ is

$$P(p) = \frac{1}{2} \delta_{|p|, 2\hbar k}$$

where $\delta_{n,m}$ denotes the Kronecker δ -function. Therefore, all particles are scattered and the initial level is finally empty.

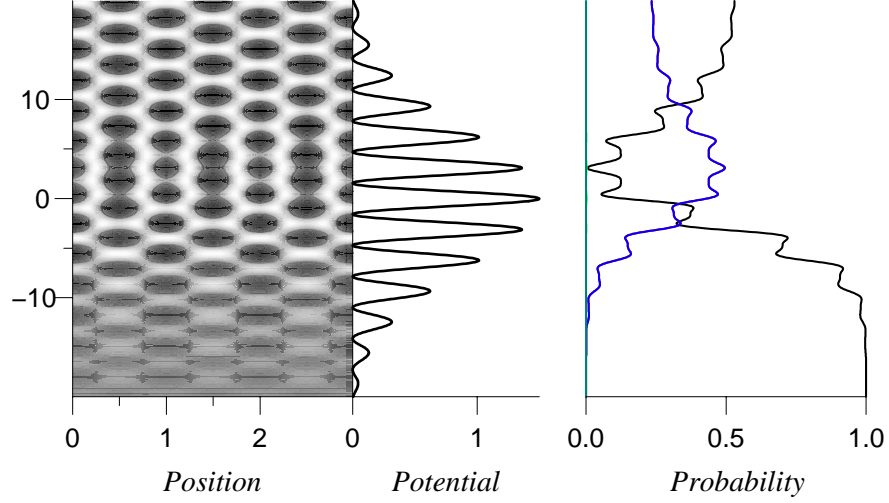


Figure 4.6: Time evolution of position and momentum for $\omega_m = 1.0$. We apply a strong potential with $A = 1.5$. The laser intensity is still too weak to transfer atoms into the $4\hbar k$ state but it is stronger than in Fig. 4.5. In the early stage of the evolution we find that the probability for the excited level rises. When the population in the scattered state is higher than in the initial state, we again see the doubling in position space. However, for later times we do not find saturation but backscattering: The probability for the $2\hbar k$ -state (blue) decays and hence, the doubling slowly disappears.

Since the far field position distribution is the Fourier transform of the above momentum distribution we expect to see a $\sin^2 x$ function in the position representation which indeed can be observed.

4.3.3 Back Scattering or Saturation?

In this step we increase the potential further. Still the potential is too weak to scatter the atoms into a $4\hbar k$ state as we see in Fig. 4.6. Therefore, we investigate whether saturation or back scattering occurs in this regime.

We apply an intensity $A = 1.5$. In the momentum picture we find only one excited momentum level. Hence, it is proven that the potential is weak

enough. On the other hand we see the probability for $p = \pm 2\hbar k$ rising until $t \cong 3$. Here we clearly recognize that this effect has no saturation but back scattering. The particles leave the $\pm 2\hbar k$ state and fall back to the initial state.

Again we find the doubling of peaks in position space for the period when the excited level is higher populated than the original one. Finally, the amount of particles in the initial momentum state is large. Therefore, the position wave function does not vanish at its minima. Further, the maxima do not have equal height. This irregular structures occur together with the population of the initial momentum state.

4.4 Conclusion

In this chapter we have found that with an appropriate intensity of the laser field a full transfer from the original state to a scattered level is possible. Since the energy is chosen weak enough no higher scattering levels are reachable. Further we recognized the effect of backscattering rather than saturation. That is, we observe *Pendellösung* behavior which is well known for a two-level system driven by a resonant field.

Chapter 5

Stepwise Scattering

Since larger interaction times do not lead to higher transversal momenta, we have to choose another way. A configuration of our lasers described in the STIRAP method described in [5] offers a solution. The acronym stands for *STImulated Raman Adiabatic Passage*. A laser beam prepares the atom first by a Stokes pulse and a second field triggers the transfer with the help of a pump pulse. The difference to our system is, that the STIRAP model acts on internal levels of the atoms with an intermediate dark state. In contrast, we want to use this model to achieve higher transversal momentum states by low laser intensities. We transfer the population stepwise and hence, we do not have a dark state. In this sense we have no STIRAP method. We only took the configuration.

In the present chapter we apply the ideas of this technique to our atomic beam. Here we use an additional longitudinal modulation in the field to transfer transversal momentum to the atoms. The passage will be used to scatter the atoms directly into a high momentum state without populating other levels.

5.1 The STIRAP Model

The original model is shown in Fig. 5.1. We emphasize that we have chosen a notation for the levels different from Ref. [5] as to bring out the similarity to our atom optics problem.

First we want to study the interaction of radiation with the atoms. In contrast to our problem, we do not consider center-of-mass motion states. In the next step we analyze analytically the process in a three-level state. Finally, we apply these results to our model of transverse momentum states numerically.

5.1.1 Transitions in a Two-Level System

The goal is to transfer atoms from one state to another. We first study this problem in a two-level system. There exist three principal ways of transferring the atoms into the desired state.

Incoherent excitation

To quantify excitation involving incoherent light one uses differential equations for excitation probabilities. Assuming that the atoms are in the ground state at time $t = 0$ and that stimulated emission dominates spontaneous emission, we find the excitation probability at time t

$$P_{\text{ex}}(t) = \frac{1}{2} [1 - e^{-\beta F(t)}]$$

where β is the absorption coefficient and

$$F(t) = \int_{-\infty}^t dt' I(t')$$

denotes the integral over the intensity of the field. Hence, we find that population of the excited state reaches 50% and the required time is proportional to the intensity of the laser.

Coherent Excitation

In contrast, quantitative discussions of coherent excitation start from a time-dependent Schrödinger equation

$$i\hbar \frac{d}{dt} \mathbf{C}(t) = H(t) \mathbf{C}(t),$$

where $\mathbf{C}(t)$ is a vector of time-dependent probability amplitudes $C_0(t)$ and $C_1(t)$. Their absolute squares provide the probability $P_n(t) = |C_n(t)|^2$ of finding the system at time t in the state $|n\rangle$. The time evolution of these functions is dictated by the Hamiltonian matrix $H(t)$. For radiative transitions the excitation is induced by an electric field acting upon a transition dipole moment. We idealize the radiation as a nearly monochromatic field, of frequency ω , having magnitude $E(t) \cos(\omega t)$. For coherent radiation the key parameter is the Rabi frequency

$$\Omega(t) = \frac{dE(t)}{\hbar}$$

where d denotes the transition dipole moment along the field. This yields the so-called Pendellösung

$$P_{\text{ex}}(t) = \left[\sin \left(\frac{1}{2} A(t) \right) \right]^2$$

where

$$A(t) = \int_{-\infty}^t dt' \Omega(t')$$

is an integral over the time dependent Rabi frequency. Hence, the population of the excited state oscillates and we find no saturation in the asymptotic time limit but oscillations.

Adiabatic transfer

In order to achieve more efficient and coherently controlled excitation probabilities than those just described, one can utilize coherent pulses whose frequency sweeps slowly across the resonance. This is called adiabatic passage. With such schemes one can obtain efficient and selective population transfer. The application of these techniques to three-state systems poses a challenging task.

5.1.2 Processes in a Three-State System

For the simplest implementation of STIRAP shown in Fig. 5.1 we use the Hamiltonian

$$H(t) = \frac{\hbar}{2} \begin{bmatrix} 0 & \Omega_P(t) & 0 \\ \Omega_P(t) & 2\Delta P & \Omega_S(t) \\ 0 & \Omega_S(t) & 2(\Delta P - \Delta S) \end{bmatrix},$$

which describes the coupling of the three states by two coherent radiation fields within the rotating wave approximation. Here, Ω_S and Ω_P denote the Rabi frequencies of the pump and the Stokes laser. Note that the envelopes of the lasers are shifted against each other. The Stokes laser rises earlier than the pulse laser. The delay between the two pulses is defined via the relation of the corresponding Rabi frequencies

$$\tan \Theta = \frac{\Omega_P(t)}{\Omega_S(t)}.$$

At this point we are interested in a parameter regime to transfer the complete population of the state $|0\rangle$ into the state $|2\rangle$ as shown in Fig. 5.2 (bottom).

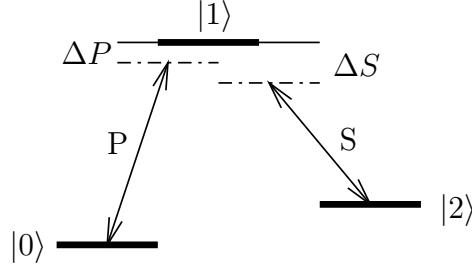


Figure 5.1: Atom used in original STIRAP model of Bergmann, Theuer and Shore. Here we consider a three-level atom originally prepared in state $|0\rangle$. The pump pulse (P) acts on the transition $|0\rangle \leftrightarrow |1\rangle$ with a detuning ΔP . The Stokes pulse (S) connects the states $|1\rangle$ and $|2\rangle$ including a detuning ΔS . Spontaneous emission from state $|1\rangle$ to further levels is taken into account. The main goal is to achieve a transition from $|0\rangle$ to $|2\rangle$ with a counter-intuitive pulse sequence: The S-pulse is active before the P-pulse arises. Hence, the S-pulse acts on an empty level. We emphasize that the detuning is important in this model in order to avoid the population of state $|1\rangle$.

Analytical Solution Technique

For an analytical treatment we skip the detunings ΔP and ΔS . At this stage we leave the STIRAP technique. In the experimental realization the detunings are important to keep the dark state $|1\rangle$ which is never populated in STIRAP. Hence, the two resonant lasers yield the simplified Hamiltonian

$$H(t) = \frac{\hbar}{2} \begin{bmatrix} 0 & \Omega_P(t) & 0 \\ \Omega_P(t) & 0 & \Omega_S(t) \\ 0 & \Omega_S(t) & 0 \end{bmatrix}. \quad (5.1)$$

In order to find the population rates for the three states we use the ansatz

$$|\psi\rangle = \begin{pmatrix} c_0 \\ c_1 \\ c_2 \end{pmatrix} = \begin{pmatrix} \alpha_0 \\ \alpha_1 \\ \alpha_2 \end{pmatrix} e^{i\lambda t/2} \quad (5.2)$$

and hence,

$$\frac{d|\psi\rangle}{dt} = i \frac{\lambda}{2} \begin{pmatrix} \alpha_0 \\ \alpha_1 \\ \alpha_2 \end{pmatrix} e^{i\lambda t/2} \quad (5.3)$$

for the wave function and its time derivative of a three-level system. Here we have separated the time independent part α_j from the time dependent part.

Inserting Eqs. (5.1) and (5.2) into the time-dependent Schrödinger equation yields

$$i\hbar \frac{d|\psi\rangle}{dt} = \frac{\hbar}{2} \begin{pmatrix} 0 & \Omega_P(t) & 0 \\ \Omega_P(t) & 0 & \Omega_S(t) \\ 0 & \Omega_S(t) & 0 \end{pmatrix} \begin{pmatrix} \alpha_0 \\ \alpha_1 \\ \alpha_2 \end{pmatrix} e^{i\lambda t/2}. \quad (5.4)$$

In the next step we recall the time derivative of the wave function ansatz, Eq. (5.3), and rewrite the system in the form

$$\begin{pmatrix} \lambda & \Omega_P(t) & 0 \\ \Omega_P(t) & \lambda & \Omega_S(t) \\ 0 & \Omega_S(t) & \lambda \end{pmatrix} \begin{pmatrix} \alpha_0 \\ \alpha_1 \\ \alpha_2 \end{pmatrix} = 0. \quad (5.5)$$

The equation

$$\det \begin{vmatrix} \lambda & \Omega_P(t) & 0 \\ \Omega_P(t) & \lambda & \Omega_S(t) \\ 0 & \Omega_S(t) & \lambda \end{vmatrix} = 0$$

yields the characteristic polynomial

$$\lambda^3 - \lambda (\Omega_P^2 + \Omega_S^2) = 0$$

in which we immediately see the zeros

$$\lambda_0 = 0 \quad \text{and} \quad \lambda_{1,2} = \pm \sqrt{\Omega_S^2 + \Omega_P^2}.$$

When we use the solution to $\lambda_0 = 0$ and rewrite Eq. (5.5) in the form

$$\lambda \alpha_0 + \Omega_P \alpha_1 = 0 \quad (5.6)$$

$$\Omega_P \alpha_0 + \lambda \alpha_1 + \Omega_S \alpha_2 = 0 \quad (5.7)$$

$$\Omega_S \alpha_1 + \lambda \alpha_2 = 0 \quad (5.8)$$

we find from Eqs. (5.6) and (5.8) a quite remarkable equation:

$$\alpha_1 \equiv 0$$

holds true for all times. When we recall that $|c_1|^2 = |\alpha_1|^2$ we recognize that the state $|1\rangle$ is never populated and hence, the normalization

$$\sum_{n=0}^2 |\alpha_n|^2 = 1$$

simplifies to

$$\alpha_0^2 + \alpha_2^2 = 1. \quad (5.9)$$

Together with Eq. (5.7) we find the final solution

$$\alpha_0 = \frac{\Omega_P}{\sqrt{\Omega_P^2 + \Omega_S^2}} \quad \text{and} \quad \alpha_2 = \frac{-\Omega_S}{\sqrt{\Omega_P^2 + \Omega_S^2}}.$$

The asymptotics in time reads now

$$\begin{aligned} t \rightarrow -\infty &\Rightarrow \Omega_S/\Omega_P \rightarrow 0 \Rightarrow \alpha_0 \rightarrow 1, \quad \alpha_1 \rightarrow 0 \\ t \rightarrow +\infty &\Rightarrow \Omega_P/\Omega_S \rightarrow 0 \Rightarrow \alpha_0 \rightarrow 0, \quad \alpha_1 \rightarrow 1 \end{aligned}$$

We recognize that in the case of an adiabatic passage the population of the initial state is completely transferred into the target state. This is the ideal case. Since we transfer the momentum via longitudinal modulation of the laser field our model is not adiabatic. This leads to an occupation of the intermediate level. Therefore, we have no STIRAP model but a stepwise transfer.

5.2 Our Setup

As seen in the previous chapters we investigate a beam with high velocity. Therefore, we consider the center-of-mass motion in longitudinal direction classically. The velocity is still high enough to remain constant and hence, we treat the propagation in z -direction as time evolution of a 1D-problem

5.2.1 Energy Structure

The properties of our atoms in x -direction are treated quantum mechanically. As outlined in Sec. 4.3 we want to scatter the particles into the $p_x = \pm 4\hbar k$ states. For this purpose we can express the transverse kinetic energy

$$\varepsilon_{\text{tr}}(n) = \frac{(2n\hbar k)^2}{2M} = (2n)^2 \hbar\omega_R$$

in units of the recoil energy $\omega_R = \hbar k^2/(2M)$ and find a $2n^2$ dependence. To scatter the atoms into the $\pm 4\hbar k$ -level we have two principle ways: *(i)* Either we provide the total required energy in one beam at a high intensity or *(ii)* we distribute the energy over two beams with high modulation. Since the energy grows with n^2 the experimental limits of the laser in the one-beam setup will be reached soon. Therefore, the laser power limits the highest achievable momentum.

We see this clearly in an example: When we transfer the momentum from the $p = 0$ to the $p = 6\hbar k$ state, we need the total energy $36\hbar\omega_R$. We can split

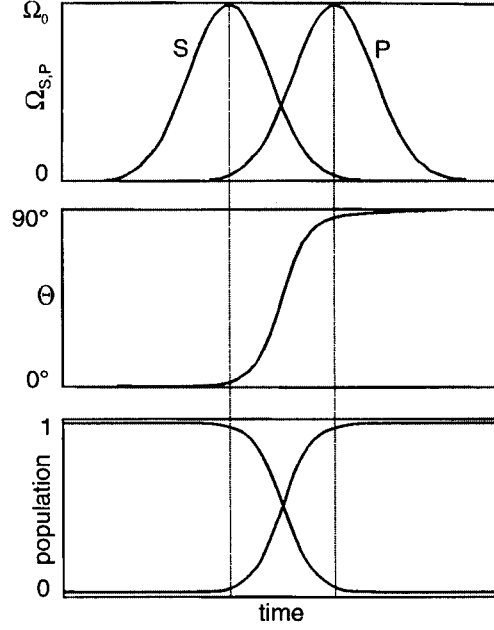


Figure 5.2: Populations in the STIRAP model. On top we show the time-dependent Rabi frequencies of the pulse (P) and Stokes (S) field. The delay between the pulses, indicated by the two vertical lines, defines the angle Θ shown in the middle. The bottom diagram displays the occupation probability for the states $|0\rangle$ which is initially populated with probability $P_0 = 1$ and $|2\rangle$ which is not populated. The curves demonstrate the perfect transfer of population from state $|0\rangle$ to $|2\rangle$. The picture is taken from Bergmann *et al.*, Rev. Mod. Phys. **70**, 1003 (1998).

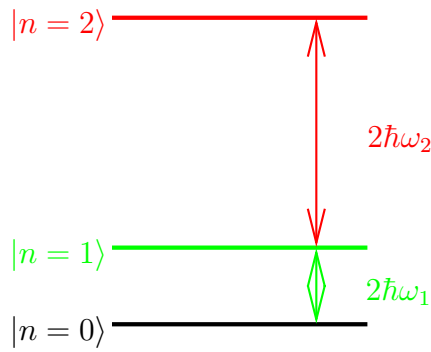


Figure 5.3: Kinetic energy of transversal momentum levels. The state $|n\rangle$ corresponds to a momentum $p = 2n\hbar k$ and an energy $\varepsilon_{\text{tr}}(n)$. To demonstrate the function of our model for momentum states we consider three states: $|0\rangle$, $|1\rangle$ and $|2\rangle$ with the corresponding energies $\varepsilon_{\text{tr}}(n)$ and the differences $2\hbar\omega_j$.

this energy on the transitions $|0\rangle \rightarrow |2\rangle$ with an energy difference of $16\hbar\omega_R$ and $|2\rangle \rightarrow |3\rangle$ with a second energy difference of $20\hbar\omega_R$. Hence, we need only half the laser power for the full transfer.

To demonstrate this scheme analytically we use the levels $|0\rangle$, $|1\rangle$ and $|2\rangle$ depicted in Fig. 5.3. For the transitions we apply the corresponding longitudinal modulation frequencies $\omega_{1,2}$ as shown in Sec. 5.2.2.

5.2.2 Laser Field Configuration

We apply one laser beam exciting the atoms from the motional state $|0\rangle$ corresponding to zero transverse momentum to state $|1\rangle$ corresponding to one unit of transverse momentum. The parameters to achieve this goal are well known from Chapter 4. These excited atoms can be scattered into the destination level $|2\rangle$ with the help of a second laser field with high longitudinal modulation.

We can express the energy difference

$$\frac{\varepsilon_{\text{tr}}(1) - \varepsilon_{\text{tr}}(0)}{2\hbar\omega_R} = 2$$

for the first transition and find with the help of the Doppler frequency $\omega_D = kv_z/2$ the Doppleron resonance

$$\omega_1 = \frac{\omega_D}{2\omega_R} = 1$$

as useful modulation for the excitation of the atoms.

Analogously we find the dimensionless energy difference

$$\frac{\varepsilon_{\text{tr}}(2) - \varepsilon_{\text{tr}}(1)}{2\hbar\omega_R} = 6$$

and hence

$$\omega_2 = 3$$

for the transition $|1\rangle \leftrightarrow |2\rangle$.

Considering the STIRAP laser field configuration we apply in a counter-intuitive way the laser for the transition $|1\rangle \leftrightarrow |2\rangle$ first. The center of this pulse is located at time $t_s < 0$. In this way we keep the laser for the transition $|0\rangle \leftrightarrow |1\rangle$ at the origin $t = 0$.

This yields the time and position dependent potential

$$V(x, t) = \frac{d^2}{\hbar\Delta} \sin^2(kx) \times \left| E_1 \cos(\omega_1 t) e^{-t^2/(2T^2)} + E_2 \cos(\omega_2 t) e^{-(t-t_s)^2/(2T^2)} \right|^2 \quad (5.10)$$

similar to Eq. (4.2). The main difference is, that the quantities E_i , ω_i and the center of the envelope are different for the two laser beams. Note that both lasers have the same envelope T . As mentioned above we apply the Stokes laser, that is the laser with field E_2 , first which means $t_s < 0$.

5.2.3 Analytical Solution

In this section we want to discuss the solutions of the Schrödinger equation

$$i\hbar \frac{\partial \psi(x, t)}{\partial t} = \left[\frac{p^2}{2M} + V(x, t) \right] \psi(x, t) \quad (5.11)$$

corresponding to the potential Eq. (5.10) in an analytical way. Therefore, we make some approximations and try to describe the process in scaled quantities.

We start with the electric fields of the laser

$$E_1 = |E_1| e^{i\varphi_1} \quad \text{and} \quad E_2 = |E_2| e^{i\varphi_2}$$

and choose the phase such that

$$\varphi \equiv \varphi_2 - \varphi_1 = \pi/2.$$

This avoids the mixing terms in the potential Eq. (5.10) and together with the scaled intensities

$$A_i \equiv \frac{d^2 E_i^2}{2\hbar^2 \Delta \omega_R}$$

we can rewrite the potential

$$V(x, t) = \frac{d^2}{\hbar \Delta} \sin^2(kx) \times \left[A_1 \cos^2(\omega_1 t) e^{-t^2/T^2} + A_2 \cos^2(\omega_2 t) e^{-(t-t_s)^2/T^2} \right].$$

To solve the Schrödinger equation Eq. (5.11) we use the ansatz

$$\psi(x, t) = \exp \left\{ -\frac{i}{2} \int_{-\infty}^t dt' \left[A_1 \cos^2(\omega_1 t') e^{-t'^2/T^2} + A_2 \cos^2(\omega_2 t') e^{-(t'-t_s)^2/T^2} \right] \right\} \times \sum_{n=-\infty}^{\infty} a_n(t) e^{i2nx}, \quad (5.12)$$

which yields the coupled differential equations

$$i \frac{da_n}{dt} = 2n^2 a_n - \frac{1}{4} \left[A_1 \cos^2(\omega_1 t) e^{-t^2/T^2} + A_2 \cos^2(\omega_2 t) e^{-(t-t_s)^2/T^2} \right] (a_{n-1} + a_{n+1}) \quad (5.13)$$

where the coefficients $a_n(t)$ obey the relations

$$a_n(-\infty) = \delta_{n,0} \quad \text{and} \quad a_n(t) = a_{-n}^*(t) = a_{-n}(t).$$

Here we assume that the incoming atom has no transverse momentum and hence, the momentum distribution is a δ -function. Due to the symmetric setup the symmetry of the momentum distribution holds true for the whole experiment.

Separation of Longitudinal Modulation

In the next step we want to simplify the coupled Eqs. (5.13). Therefore, we separate the envelopes of the fields resulting from the constants in the longitudinal modulation

$$\cos^2(\omega t) = \frac{1}{2} + \frac{1}{4} (e^{-2i\omega t} + e^{2i\omega t}).$$

We express the functions a_n in the form

$$a_n(t) = \exp \left[\frac{i}{8} \int_{-\infty}^t dt' \left(A_1 e^{-t'^2/T^2} + A_2 e^{-(t'-t_s)^2/T^2} \right) \right] b_n(t)$$

while $b_n(t)$ satisfies the new system of equations

$$i \frac{db_n}{dt} = 2n^2 b_n - \frac{1}{16} \left[A_1 e^{t^2/T^2} (e^{-2i\omega_1 t} + e^{2i\omega_1 t}) + A_2 e^{-(t-t_s)^2/T^2} (e^{-2i\omega_2 t} + e^{2i\omega_2 t}) \right] (b_{n-1} + b_{n+1})$$

including the symmetry relation

$$b_n = b_{-n}.$$

Intensity Coefficients

Since we are interested in the transfer to the second transversal momentum state we can cut the coupled equations at $b_{\pm 2}$. Recalling the modulation frequencies $\omega_1 = 1$ and $\omega_2 = 3$ from Sec. 5.2.2 we introduce the coefficients

$$c_0 = b_0, \quad c_1 = b_1 \sqrt{2} e^{2it} \quad \text{and} \quad c_2 = b_2 \sqrt{2} e^{8it}$$

and the Rabi frequencies

$$\Omega_1 \equiv \frac{A_1}{16} e^{-t^2/T^2} \quad \text{and} \quad \Omega_2 \equiv \frac{A_2}{8\sqrt{2}} e^{-(t-t_s)^2/T^2}.$$

From the standard STIRAP notation Eq. (5.4) we find a system of equations

$$\begin{aligned} i \, dc_0/dt + \Omega_2(t) c_1 &= 0 \\ \Omega_2(t) c_0 + i \, dc_1/dt + \Omega_1(t) c_2 &= 0 \\ \Omega_1(t) c_1 + i \, dc_2/dt &= 0 \end{aligned} \tag{5.14}$$

for the functions c_n .

Now we can use the ansatz Eqs. (5.2) and (5.3)

$$\frac{d}{dt} \begin{pmatrix} c_0 \\ c_1 \\ c_2 \end{pmatrix} = \frac{d}{dt} \begin{pmatrix} \alpha_0 \\ \alpha_1 \\ \alpha_2 \end{pmatrix} e^{i\lambda t/2} = i \frac{\lambda}{2} \begin{pmatrix} \alpha_0 \\ \alpha_1 \\ \alpha_2 \end{pmatrix} e^{i\lambda t/2}$$

to simplify Eq. (5.14). This yields a familiar set of equations

$$\begin{aligned} \lambda \alpha_0 + \Omega_2(t) \alpha_1 &= 0 \\ \Omega_2(t) \alpha_0 + \lambda \alpha_1 + \Omega_1(t) \alpha_2 &= 0 \\ \Omega_1(t) \alpha_1 + \lambda \alpha_2 &= 0. \end{aligned} \tag{5.15}$$

This is exactly Eq. (5.5) which we have solved already in Sec. 5.1.2.

5.3 Numerical Results

Now we are in a position to apply our knowledge about parameters to a numerical simulation. We emphasize that a complete transfer is possible in an adiabatic regime. The longitudinal modulation breaks the adiabaticity and we try to realize transfer in two steps with two beams. In our parameter regimes we mainly change the width and intensities of the beams. One setup is characterized by an envelope with $T = 15$ whereas the wide beam is described by a Gaussian with width $T = 35$.

5.3.1 Narrow Beams

The atomic wave is prepared at time t_0 and the particles fly towards a strong laser field which activates the transition from $2\hbar k$ to $4\hbar k$ at a modulation frequency $\omega_2 = 3.0$. After a delay the weak laser at $\omega_1 = 1.0$ turns on. This second field takes the atoms from their initial state to the $2\hbar k$ state. Since the beam for the transition from level $|1\rangle$ to $|2\rangle$ is already active, the transfer continues.

In Fig. 5.4 we plot the time dependence. The transition $|0\rangle \leftrightarrow |1\rangle$ is induced by the later field with intensity $A_1 = 0.6$. The geometrically first laser has an intensity $A_2 = 1.2$. Hence, the delay is $t_s = -1.3$. The width of the Gaussian envelopes is $T = 15.0$. We find the decay of the probability for $p = 0$ (black) and a rise for $p = 2\hbar k$ (blue). This population rate decreases soon and the final state $p = 4\hbar k$ (green) appears. We end at the final probabilities $P_0 \approx P_{\pm 1} \approx 7\%$ and $P_{\pm 2} \approx 39\%$.

Since the $4\hbar k$ state contains most of the atoms we find four peaks per period in the position distribution. This is clearly shown in the position density. The momentum diagram shows the beats of the different modulation frequencies and the shift between the laser beams.

We do not find the doubling seen in Sec. 4.3.2 since there is no regime when the first level is more populated than the original level. The scattering to the $4\hbar k$ state starts before the $2\hbar k$ state is maximally populated.

Nevertheless, in the end there are some particles left which were not transferred to the desired level. These atoms cause some asymmetries as depicted in the left side of Fig. 5.6. Note that the probability does not display zeros since there are too many peaks per period. Hence, they start to overlap already.

5.3.2 Wide Beams

In order to improve the separation of the beams we change our laser fields to a spread of $T = 35$. The setup is basically the same as before in Sec. 5.3.1. Even the delay is again $t_s = -1.3$. Besides the wide envelopes with long interaction the fields are weaker with $A_1 = 0.43$ and $A_2 = 0.81$.

Both evolutions in position and momentum space are similar as before. We find the four beams per period and the rise of the different probabilities for the different momenta are comparable. The difference is based in the individual probabilities. In this regime we find $P_0 \approx 2\%$, $P_{\pm 1} \approx 6\%$ and $P_{\pm 2} \approx 43\%$.

As depicted in Fig. 5.6 the peaks are now more similar in height. Further the minima in the cross section are deeper. Hence, the overlap is smaller or

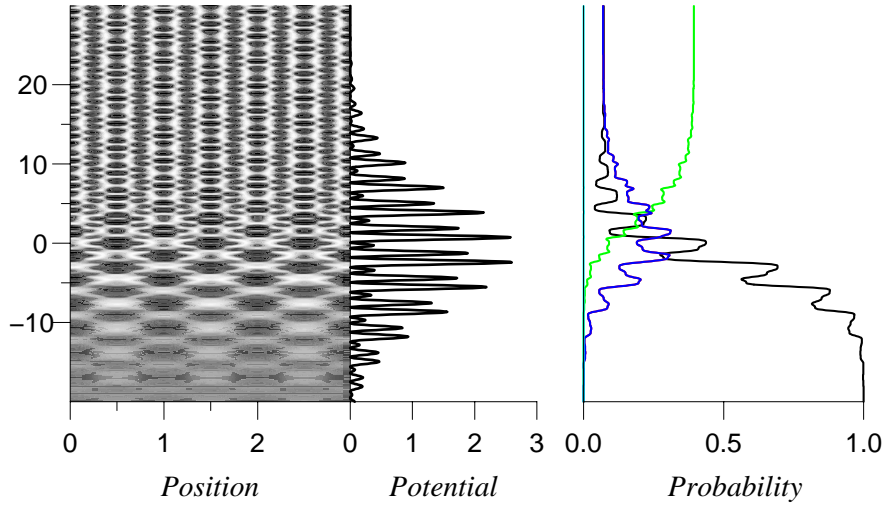


Figure 5.4: Time evolution of position and momentum for a stepwise setup with narrow laser beams. The delay between the beams is $|t_s| = 1.3$. Therefore, the field intensity has beats. In the momentum picture we observe the decay of the initial momentum state $|0\rangle$ (black) and the rise of the first scattered level (blue). This decays soon and the final state (green) comes up. Note that we have two symmetric momentum states. Hence, each state appears with probability $1/2$. After the interaction the second level is mainly populated and in the position picture we find four beams per period.

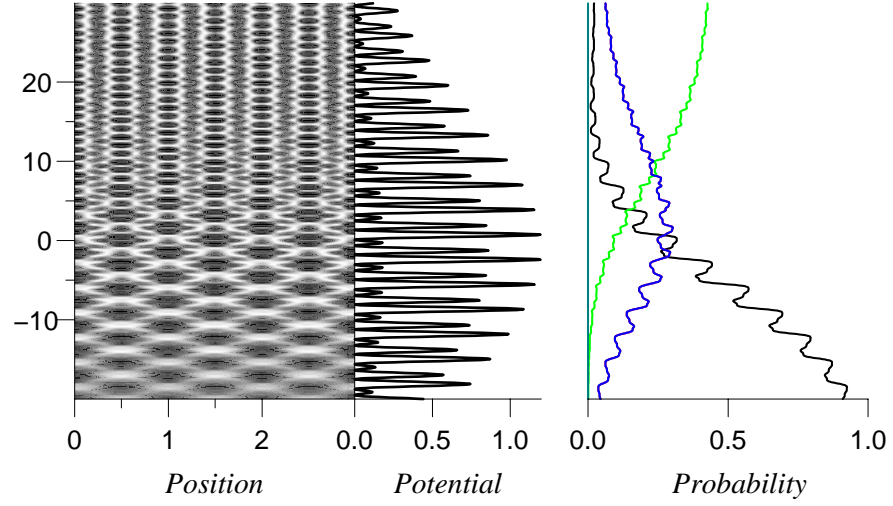


Figure 5.5: STIRAP setup with wide beams. Here, in contrast to Fig. 5.3.1, the envelope of the Gaussians is $T = 35$. The delay between the two beams is the same, namely $t_s = 1.3$. The evolution is the same. The main difference occurs in the final probabilities.

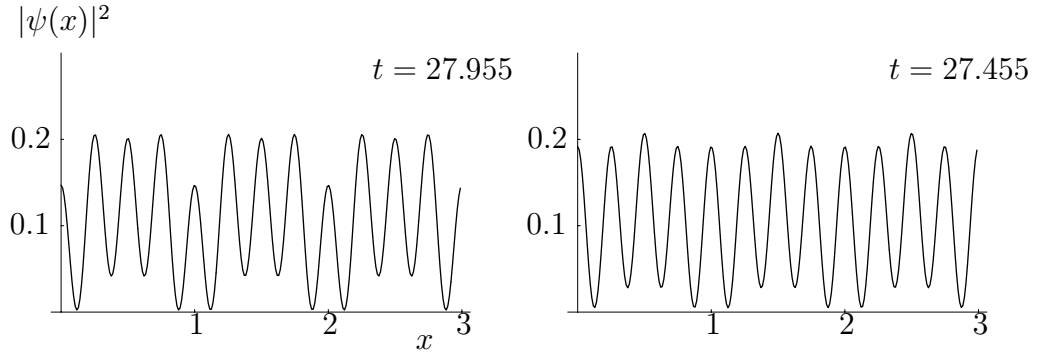


Figure 5.6: Cross section of Figs. 5.4 (left) and 5.5 (right) at slightly different times. We find more regular structures for the wide envelopes. Note that a higher period without focusing is not possible, since the peaks already overlap.

the separation is better.

5.4 Conclusion

In this chapter we have demonstrated a method to transfer momenta to appropriate transverse momentum states. This is mainly useful for the model of a beam splitter. In contrast to some experiments by Ton van Leeuwen's group we can control which state is populated. The second advantage of our regime is the passage through an intermediate state. We need less laser power. We do not transfer the particles at once. Hence we do not provide the complete energy in one step. It is sufficient to provide the energy for two smaller steps. Of course, this is not quite convincing for the second momentum state since the necessary field strength grows by $2n^2$. The advantage becomes clear when we go on to the third level and assume the second state as intermediate level. Then the energy difference is similar.

Appendix A

Paraxial Approximation

In this Appendix we want to investigate the relation of the 2D-evolution and the time evolution. Therefore, we show the derivation of the Schrödinger equation in detail.

We start with the ordinary time-independent Schrödinger equation

$$\hat{H}\phi = E\phi.$$

On the right hand side we express the energy in terms of $\hbar k$

$$\left[\frac{\hat{p}^2}{2M} + V(\hat{x}) \right] \phi = \left[-\frac{\hbar^2}{2M} \Delta + V(\hat{x}) \right] \phi = \left(\frac{(\hbar k)^2}{2M} + \varepsilon \right) \phi \quad (\text{A.1})$$

plus a correction $\varepsilon \cong 0$.

For slowly varying z we can make the ansatz

$$\phi(x, y, z) = e^{ikz} \psi(x, y, z)$$

for the wave function. This ansatz yields the second derivative

$$\Delta \phi(x, y, z) = \left(e^{ikz} \Delta + 2ik e^{ikz} \frac{d}{dz} - k^2 e^{ikz} \right) \psi(x, y, z)$$

which we substitute into Eq. (A.1)

$$\frac{\hbar^2}{2M} 2ik \frac{d}{dz} \psi(x, y, z) = \left[\frac{\hat{p}^2}{2M} + V(\hat{x}) \right] \psi(x, y, z) = \hat{H}\psi(x, y, z). \quad (\text{A.2})$$

With the help of the scaling relation

$$\hbar k = Mv_z = M \frac{dz}{dt}$$

the left hand side of Eq. (A.2) simplifies to

$$i\hbar \frac{d}{dt} \psi(x, y, z) = \hat{H} \psi(x, y, z).$$

Hence, we find the time-dependent Schrödinger equation which we solve for our 2D-problems. We have found a way to solve these problems in 1D-schemes.

Appendix B

Focusing Function

In Sec. 2.2.1 we have used an analytical expression for the width $\Delta(t)$. In the present Appendix we derive in detail how to get the formula.

We can write the time evolution as

$$\psi(x, t) = \int_{-\infty}^{\infty} dx_0 K(x, t|x_0, t_0) \psi(x_0, t_0). \quad (\text{B.1})$$

where

$$K(x, t|x_0, t_0) \equiv \sqrt{\frac{1}{2\pi i s(t)}} \exp \left[\frac{i}{2} \left(\frac{\dot{c}(t)}{c(t)} x^2 + \frac{c(t)}{s(t)} \left(\frac{x}{c(t)} - x_0 \right)^2 \right) \right]$$

denotes the Green's function [35] in scaled variables. For this purpose we recall the solutions $s(t)$ and $c(t)$ of Eqs. (2.1). Note that in the case of a non time-dependent harmonic oscillator these functions are sine and cosine.

In our case the initial wave function is a Gaussian

$$\psi(x) = \frac{1}{(\pi \Delta_0^2)^{1/4}} \exp \left(-\frac{x^2}{2\Delta_0^2} \right).$$

Since this Gaussian is neither time-dependent nor contains a complex part, the integral Eq. (B.1) results in

$$\psi(x, t) = \frac{1}{(\pi \Delta^2(t))^{1/4}} \exp \left[-\frac{1}{2} \left(\frac{x}{\Delta(t)} \right)^2 \right] \exp \left[\frac{i}{2} \Phi(x, t) \right]. \quad (\text{B.2})$$

Note that the wave packet remains Gaussian through the whole process. The phase $\Phi(x, t)$ is a rather complicated expression which we skip, since we are

interested in measuring the width of the atomic beam. Hence, the probability distribution

$$|\psi(x, t)|^2 = \frac{1}{\pi \Delta^2(t)} \exp \left[-\frac{x^2}{\Delta^2(t)} \right] \quad (\text{B.3})$$

is more useful. In Eqs. (B.2) and (B.3) we have introduced the time-dependent function

$$\Delta(t) \equiv \frac{\sqrt{s^2(t) + \Delta_0^4 c(t)}}{\Delta_0}$$

to simplify the expressions. Note that this is the focusing function denoting the time-dependent width of the Gaussian. The knowledge of $s(t)$ and $c(t)$ is sufficient to calculate the theoretically expected width.

Appendix C

Analytical Solution of Two Wave Mixing

In order to get some insight into the density distribution of the scattered atoms obtained numerically in Sec. 3.3 we summarize the approximate analytical solutions. We show in detail how to solve the Schrödinger equation and explain our approximations. Therefore, we introduce the two waves with amplitudes c_{\pm} for each of the two waves and investigate the effects of scattering and damping on them for different regimes.

C.1 Analytical Model

We investigate the system with the Hamiltonian Eq. (3.1)

$$H = \frac{p^2}{2M} + \frac{(dE)^2}{\hbar} \frac{\sin^2 kx}{\Delta(t) + i\gamma/2} \quad (\text{C.1})$$

and the detuning function

$$\Delta(t) = \Delta_0 t/\tau.$$

Here we have omitted the Gaussian envelope since we concentrate on the vicinity of $t = 0$. In this regime the Gaussian plays no important role provided the Gaussian is much broader than the domain over which the detuning changes, that is $T \gg 1$. From Secs. 3.2 and 3.3 we recall

$$\lambda = \left(\frac{dE}{\hbar} \right)^2 \cdot \frac{\tau}{4\Delta_0}, \quad t_0 = \frac{\gamma\tau}{2\Delta_0} \quad \text{and} \quad \omega_R = \frac{\hbar k^2}{2M}.$$

C.1.1 Approximate Solution

If the inequality

$$\frac{(dE)^2}{\hbar^2} \frac{1}{|\Delta(t) + i\gamma/2|} \ll \omega_R$$

holds true, then only the incoming atomic wave which falls onto the crystal near the Bragg angle effectively interacts with the periodic potential. The laser field is weak and we can describe the process with two plan waves with the momenta

$$p_x = \pm \hbar k + \delta p.$$

Here we introduced a momentum deviation $|\delta p| \ll \hbar k$. For the mixing we use the ansatz

$$\psi(x, t) = e^{-i\varphi(t)} e^{-\Gamma(t)} \left[c_+(t) e^{i(1 + \frac{\delta p}{\hbar k})x} + c_-(t) e^{i(-1 + \frac{\delta p}{\hbar k})x} \right]$$

where $\varphi(t)$ denotes the phase which is of no physical importance. We insert this ansatz into the time-dependent Schrödinger equation

$$i\hbar \frac{d}{dt} \psi(x, t) = H \psi(x, t) \quad (\text{C.2})$$

with the Hamiltonian Eq. (C.1).

Hence, we find for the damping rate

$$\Gamma(t) = 2\lambda \left(\arctan \frac{t}{t_0} + \frac{\pi}{2} \text{sign} \Delta_0 \right).$$

For the physical solution a negative damping is forbidden. Since we have included the sign of the initial detuning Δ_0 in t_0 we have to consider the sign-function. We find that $\Gamma(t)$ is positive and fulfills the boundary conditions

$$\Gamma(-\infty) = 0 \quad \text{and} \quad \Gamma(+\infty) = 2\pi|\lambda|.$$

From Eq. (C.2) we find for the derivatives of c_{\pm} the differential equations

$$\begin{aligned} i \frac{dc_+}{dt} &= \delta c_+ + \frac{\lambda}{t + it_0} c_- \\ i \frac{dc_-}{dt} &= \delta c_- + \frac{\lambda}{t + it_0} c_+ \end{aligned} \quad (\text{C.3})$$

where

$$\delta \equiv \frac{k \delta p}{M}$$

plays the role of detuning. The amplitudes c_{\pm} satisfy the initial conditions

$$c_+(-\infty) = e^{-i\delta t} \quad \text{and} \quad c_-(-\infty) = 0.$$

Decoupling of Differential Equations

For $\delta \neq 0$ we can introduce the superpositions

$$u = c_+ + c_- \quad \text{and} \quad v = c_+ - c_-$$

and the above differential equations, Eqs. (C.3), read

$$\begin{aligned} i \frac{du}{dt} &= \frac{\lambda}{t + it_0} u + \delta v \\ i \frac{dv}{dt} &= \frac{\lambda}{t + it_0} v + \delta u \end{aligned}$$

with the initial conditions

$$u(t \rightarrow -\infty) = v(t \rightarrow -\infty) = e^{-i\delta t}. \quad (\text{C.4})$$

We can rewrite this system of coupled equations in one differential equation of second order

$$\frac{d^2 u}{dt^2} + \left[\delta^2 - \frac{\left(\frac{1}{2} + i\lambda\right)^2 - \frac{1}{4}}{(t + it_0)^2} \right] u = 0. \quad (\text{C.5})$$

Kamke [25] presents the the solution of Eq. (C.5), subjected to the initial conditions Eq. (C.4),

$$u = A \sqrt{z} H_{\frac{1}{2} + i\lambda}^{(2)}(z).$$

Here $H_\nu^{(2)}(z)$ is the Hankel function or Bessel function of the 3rd type of the complex variable

$$z = \delta(t + it_0).$$

The amplitude reads

$$A = -i \sqrt{\frac{\pi}{2}} e^{\frac{\pi\lambda}{2} - \delta t_0}.$$

Analogously we find the solution for v and therefore the complete solution yields

$$c_{\pm} = -i \sqrt{\frac{\pi}{8}} e^{-\delta t_0} \left[e^{\frac{\pi\lambda}{2}} H_{\frac{1}{2} + i\lambda}^{(2)}(z) \pm e^{-\frac{\pi\lambda}{2}} H_{\frac{1}{2} - i\lambda}^{(2)}(z) \right]. \quad (\text{C.6})$$

Note, that the whole calculation only holds true for $\delta \neq 0$.

C.1.2 Hankel Functions

In the expression Eq. (C.6) for the amplitudes c_{\pm} Hankel functions play an important role. Before we start discussing the results we have to get familiar with these functions.

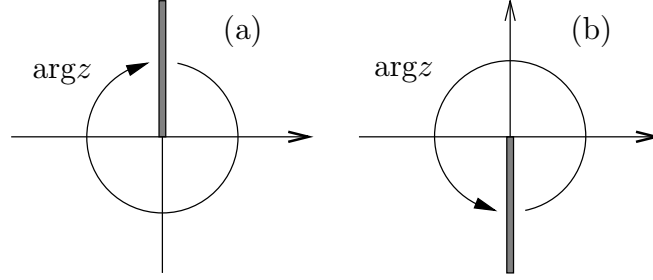


Figure C.1: Complex z -plane with cut along the imaginary axis. In the left picture denoted by (a) the cut is along the positive part of the imaginary axis and the argument runs in negative direction. The right plot (b) displays the cut in the negative part of the axis and the arguments runs in positive direction.

Definition

From Abramowitz [2] we recall standard form of the Bessel-differential equation

$$z^2 \frac{d^2 w}{dz^2} + z \frac{dw}{dz} + (z^2 - \nu^2) w = 0. \quad (\text{C.7})$$

The solutions for this equation are Bessel functions of different kinds. The most familiar is the first kind $J_{\pm\nu}(z)$. The second type is called Neumann's function and is denoted by $Y_{\nu}(z)$. The third kind of Bessel functions are called Hankel functions $H_{\nu}^{(1,2)}(z)$.

The solutions of Eq. (C.7) are connected to each other via the relations

$$Y_{\nu}(z) = \frac{J_{\nu}(z) \cos(\nu\pi) - J_{-\nu}(z)}{\sin(\nu\pi)}$$

and

$$H_{\nu}^{(1,2)}(z) = J_{\nu}(z) \pm i Y_{\nu}(z).$$

Note that the Hankel functions $H^{(1,2)}$ are holomorphic throughout the z -plane cut along the negative real axis.

Integral Representation

Bateman [3] presents the integral representation

$$\Gamma\left(\nu + \frac{1}{2}\right) H_{\nu}^{(2)}(z) = \sqrt{\frac{2}{\pi z}} e^{-i(z - \frac{\pi\nu}{2} - \frac{\pi}{4})} \int_0^{\infty} dt e^{-t} t^{\nu - \frac{1}{2}} \left(1 - \frac{it}{2z}\right)^{\nu - \frac{1}{2}} \quad (\text{C.8})$$

of the Hankel functions for

$$\operatorname{Re} \nu > -\frac{1}{2} \quad \text{and} \quad -\frac{3\pi}{2} < \arg z < \frac{\pi}{2}.$$

We find that $H_\nu^{(2)}$ is an analytical function in the complex z -plane with a cut along the positive imaginary axis as shown in Fig. C.1(a).

First Hankel Function

Since the Hankel function is a superposition of two Bessel functions there is a symmetric and an antisymmetric way to combine these functions. For the positive superposition

$$H_\nu^{(1)}(z) = J_\nu(z) + i Y_\nu(z)$$

there is the integral expression

$$\Gamma\left(\nu + \frac{1}{2}\right) H_\nu^{(1)}(z) = \sqrt{\frac{2}{\pi z}} e^{-i\left(z - \frac{\pi\nu}{2} - \frac{\pi}{4}\right)} \int_0^\infty dt e^{-t} t^{\nu-\frac{1}{2}} \left(1 + \frac{it}{2z}\right)^{\nu-\frac{1}{2}} \quad (\text{C.9})$$

for

$$\operatorname{Re} \nu > -\frac{1}{2} \quad \text{and} \quad -\frac{\pi}{2} < \arg z < \frac{3\pi}{2}.$$

This representation Eq. (C.9) is valid in the complex plane except a cut at the negative imaginary axis as shown in Fig. C.1(b).

To connect the open ends of Eq. (C.8) we use the relation

$$H_\nu^{(2)}(z) = -H_\nu^{(1)}(z) - 2e^{i\pi\nu} \cos(\pi\nu) H_\nu^{(1)}(z). \quad (\text{C.10})$$

This is the complete set of equations and functions to solve the problem. The equations provide the description for the effects in our model.

C.2 Regimes of Damping and Scattering

We have the solution of the two-wave mixing. Recalling the properties of the Hankel function we can illustrate the physics in this system. Here we want to mark the separated regions of damping or scattering, or find regimes where both effects occur simultaneously.

C.2.1 Asymptotics after Interaction

We are ready to calculate the asymptotic behavior of the amplitudes c_\pm for $t \rightarrow \infty$. The main difference in the amplitudes is connected to the sign of $\Delta_0 \cdot \delta$.

Blue Detuning

First we consider the case $\Delta_0 > 0$. Therefore, $\lambda > 0$ holds true. For $\delta > 0$ we find that $\arg z = \arg[\delta(t + it_0)]$ changes from $-\pi$ to -2π when t changes from $-\infty$ to ∞ . Since the argument crosses the cut in the complex z -plane we get following Eq. (C.10) a decomposition into two functions $H_{\frac{1}{2} \pm i\lambda}^{(1)}(z)$ and $H_{\frac{1}{2} \pm i\lambda}^{(2)}(z)$. Using the integral relations Eqs. (C.9) and (C.8) we can calculate the asymptotics

$$\begin{aligned} c_+(t \rightarrow +\infty) &= e^{-i\delta t} \\ c_-(t \rightarrow +\infty) &= -2 \sinh(\pi\lambda) e^{-2\delta t_0} e^{i\delta t} \end{aligned}$$

Hence, we find the probabilities

$$\begin{aligned} W_+ &= e^{-2\Gamma(\infty)} |c_+(+\infty)|^2 = e^{-4\pi\lambda} \\ W_- &= e^{-2\Gamma(\infty)} |c_-(+\infty)|^2 = 4 \sinh^2(\pi\lambda) e^{-4\pi\lambda} e^{-4\delta t_0} \end{aligned} \quad (\text{C.11})$$

Now we turn to the case of $\delta < 0$. Note, that Δ_0 is still positive. So far only the sign of $\Delta_0\delta$ has changed. In this case $-\pi < \arg z < 0$ holds true. Hence, the integral relation does not cross the cut in the complex plane. Therefore, no splitting occurs and the result follows directly

$$\begin{aligned} c_+(t \rightarrow \infty) &= e^{-i\delta t} \\ c_-(t \rightarrow \infty) &= 0. \end{aligned}$$

We find that the amplitude for the scattering, c_- , vanishes. In contrast to Eqs. (C.11) we find only damping in the probabilities

$$\begin{aligned} W_+ &= e^{-4\pi\lambda} \\ W_- &= 0. \end{aligned}$$

When we consider the scattering probability $W_{\text{scatt}} = W_-(\delta)$ as a function of the angular detuning δ we find a sharp asymmetry

$$W_{\text{scatt}}(\delta) = \begin{cases} B(\lambda) e^{-4\delta t_0} & \text{for } d > 0 \\ 0 & \text{for } d < 0 \end{cases} \quad \text{with } B(\lambda) = 4 \sinh^2(\pi\lambda) e^{-4\pi\lambda}$$

Red Detuning

For Δ_0 and, hence $\lambda < 0$, the scattered wave vanishes for $\delta > 0$. This yields immediately the scattering probability

$$W_{\text{scatt}}(\delta) = \begin{cases} 0 & \text{for } d > 0 \\ B(|\lambda|) e^{-4\delta t_0} & \text{for } d < 0 \end{cases} \quad \text{with } B(\lambda) = 4 \sinh^2(\pi\lambda) e^{-4\pi\lambda} \quad .$$

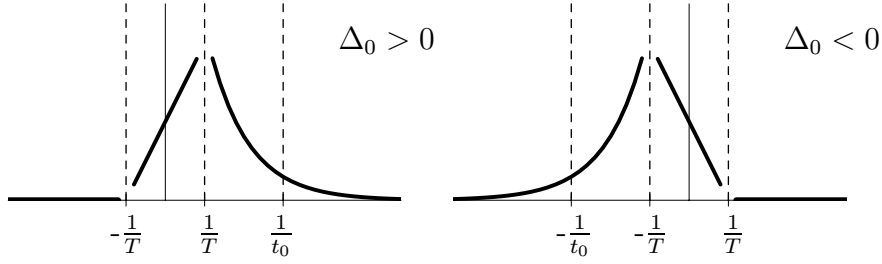


Figure C.2: The scattering function $W_{\text{scatt}}(\delta)$ for different Δ_0 . We observe a shift of the maximum depending on the sign of Δ_0 . The dashed lines denote our different regimes. Note, that we only made qualitative predictions for the gaps.

The asymmetry of the scattering probability manifests itself as a jump at $\delta = 0$. The lack of continuity at this point is not quite satisfactory from a physical point of view. It originates from the fact that the asymptotic regime $|z| \gg 1$ is realized providing $|t| \gg 1/|\delta|$. In other words, we need an infinite interaction time when $\delta \rightarrow 0$. To describe correctly this limit we introduce an envelope function

$$\lambda(t) = \lambda e^{-(t/T)^2}$$

where T is large but finite. So far, our results are only valid in the regime

$$|\delta|, 1/t_0 \gg 1/T.$$

These inequalities guarantee that the asymptotic regime $|z| \gg 1$ may be realized when $1/|\delta| \ll |t| \ll T$ and $\lambda(t) = \lambda = \text{const.}$

The opposite case

$$|\delta| \leq 1/T \ll 1/t_0$$

is investigated separately. Due to the known limitations of Hankel functions this investigation cannot be done analytically. For

$$|\delta| \ll 1/T \ll 1/t_0$$

we can apply perturbation theory for a small parameter range of $|\delta|T \ll 1$. Simple calculations yield

$$W_{\text{scatt}} \approx e^{-4\pi|\lambda|} [\sinh(\pi\lambda) + \delta T \text{sign}\Delta_0].$$

This yields the sign of the derivative $\partial W_-/\partial\delta$ is given by the sign of Δ_0 . This derivative indicates the position of the maximum shown in Fig. C.2. For $t_0 \ll T$ the width of the Bragg resonance given by $1/t_0$ is much larger than the shift.

C.2.2 Conclusion

To conclude we note that the angular dependence of the Bragg scattering by the absorbing potential with the linear time-dependent detuning shows a sharp asymmetry. It has two scales

$$|\delta| \sim \frac{1}{t_0} \quad \text{and} \quad |\delta| \sim \frac{1}{T},$$

the first one is connected with the slope of the function $\Delta(t)$. The second scale is determined by the interaction time T . Considering the inequality $|t_0| \ll T$ the slope of the curve $W_{\text{scatt}}(\delta)$ in the vicinity of $\delta = 0$ is much steeper than the other slope of the curve. The width of the Bragg resonance is determined by the first scale, $1/t_0$, while the inverse interaction time, $1/T$, determines a sharp asymmetry of the scattering probability in the vicinity of the exact Bragg angle, which is $\delta = 0$.

Appendix D

Scattering with Nonadiabatic Modulation

In this appendix we will derive some approximate analytical solutions for the dynamics of an atomic wave in a two-dimensional light crystal with the geometry depicted in Fig. 4.1.

In the following analysis we concentrate mainly on the influence of two parameters — the frequency ω_m and the amplitude $A > 0$. We investigate the in-crystal density of the atomic wave and the momentum components of the outgoing atoms.

D.1 The Basic Dynamics

From Chapter 4 we recall the Schrödinger equation (Eq. 4.3)

$$i \frac{\partial \psi(x, t)}{\partial t} = -\frac{1}{2} \frac{\partial^2 \psi(x, t)}{\partial x^2} + A f(t) \sin^2 x \psi(x, t).$$

The general ansatz for the solution can be written in the form

$$\psi(x, t) = \exp \left[-i \frac{A}{2} \int_{-\infty}^t f(t') dt' \right] \sum_{-\infty}^{\infty} c_n(t) e^{i2nx}. \quad (\text{D.1})$$

Inserting Eq. (D.1) into equation Eq. (4.3) we obtain an infinite chain of coupled equations for the unknown amplitudes $c_n(t)$

$$i \frac{dc_n(t)}{dt} = 2n^2 c_n - \frac{A}{4} f(t) (c_{n-1} + c_{n+1}). \quad (\text{D.2})$$

Since we start with a plane atomic wave without transversal momenta the initial conditions for this set of equations read

$$c_n(-\infty) = \delta_{n,0} \quad (\text{D.3})$$

because we consider only normal incidence. From Eq. (D.2) and initial condition, Eq. (D.3), we see that the problem is symmetric and the expansion coefficients are real and satisfy the equation

$$c_n(t) = c_{-n}(t). \quad (\text{D.4})$$

Using this relation and the ansatz Eq. (D.1) the atomic density reads

$$|\psi(x, t)|^2 = \left| c_0(t) + 2 \sum_{n=1}^{\infty} c_n(t) \cos(2nx) \right|^2.$$

D.1.1 Weakly modulated crystal

In Fig. 4.3 we studied the situation of a longitudinally weakly modulated crystal under the assumptions that $A < 1$ and that the modulation frequency is not too close to the Doppleron resonance, $|\omega_m - 1|T \geq 1$, in which case we expect only a small variation of the atomic wave function. This is valid also for the momentum components. The zeroth momentum component of the wave shows a deviation from its initial value only at the vicinity of the maximum potential intensity. In this region the first momentum components are slightly excited, resulting in an additional modulation of the in-crystal density $|\psi(x, t)|^2$. The atoms are not guided only through the minima of the potential valleys. As soon as the zeros of the longitudinal modulation $\cos^2(\omega_m t)$ turn off the potential the atoms start to spread. Then the potential is turned on again since the modulations damp the field only for a short time and the atoms are forced back to their previous positions. After the potential is totally switched off ($t > T$), the atomic wave is almost in its initial state because each of the switches can be considered as adiabatic.

The in-crystal behavior of the atomic wave can be treated analytically using a three-wave ansatz

$$\begin{aligned} \psi(x, t) &= c_0(t) + c_1(t) e^{2ikx} + c_{-1}(t) e^{-2ikx} \\ &= c_0(t) + 2c_1(t) \cos(2kx) \end{aligned} \quad (\text{D.5})$$

for the wave function using Eq. (D.4).

This approximation is justified by the level structure of the kinetic energy part of the Hamiltonian. The scaled energy levels are spaced as $\varepsilon_{tr}(n) = 2n^2$.

For a moderate potential amplitude only the transitions between the $n = 0$ - and $n = 1$ -levels are important since the energy is not sufficient to transfer the atoms into higher states. In the last step in Eq. (D.5) we used the symmetry given by Eq. (D.4). The expansion coefficients $c_0(t)$ and $c_1(t)$ obey the following set of coupled equations

$$\begin{aligned} i \dot{c}_0(t) &= -\frac{1}{2} A f(t) c_1(t) \\ i \dot{c}_1(t) &= 2c_1(t) - \frac{1}{4} A f(t) c_0(t). \end{aligned} \quad (\text{D.6})$$

The amplitude of the zeroth momentum component does not change significantly, that is

$$c_0(t) \approx c_0(-\infty) = 1. \quad (\text{D.7})$$

The equation for $c_1(t)$ takes the form

$$i \dot{c}_1(t) = 2c_1(t) - \frac{A}{4} f(t). \quad (\text{D.8})$$

The solution satisfying the initial condition $c_1(-\infty) = 0$ reads

$$c_1(t) = i \frac{A}{4} \int_{-\infty}^t d\xi f(\xi) e^{-2i(t-\xi)}. \quad (\text{D.9})$$

Therefore, the in-crystal density has the form

$$|\psi(x, t)|^2 \approx 1 + A \cos(2x) \int_0^\infty d\xi f(t - \xi) \sin(2\xi),$$

where we have neglected the second order term. The time-dependent integral on the right hand side shows oscillatory behavior with changes in sign. It leads to the alternation of brightness along the t axis in Fig. 4.3.

For large times $t \gg T$ the outgoing atomic density

$$|\psi(x, t)|^2 \approx 1 + \frac{AT\sqrt{\pi}}{4} \left[2e^{-T^2} + e^{-T^2(\omega_m+1)^2} + e^{-T^2(\omega_m-1)^2} \right] \sin 2t \cos 2x \quad (\text{D.10})$$

looks like the superposition $\sin[2(t-x)] + \sin[2(t+x)]$ of the two running density waves on the background of the average density. We call them the Doppleron density waves. For large T and $\omega_m < 2$ the T -dependent coefficient in Eq. (D.10) is dominated by the third term in the brackets and shows the resonance structure with the width $|\omega_m - 1| \sim 1/T$ given by the inverse time of flight.

D.1.2 Resonant modulation of the crystal

The results of the previous section corresponding to the weak coupling of the c_0 and c_1 amplitudes are modified when we adjust the modulation frequency to the resonance condition $\omega_m = 1$.

For our analysis we only take into account the resonant terms in Eq. (D.5) and arrive at

$$\begin{aligned} i \dot{c}_0(t) &= -\frac{1}{8} A e^{-t^2/T^2} e^{2it} c_1(t) \\ i \dot{c}_1(t) &= 2 c_1(t) - \frac{1}{16} A e^{-t^2/T^2} e^{-2it} c_0(t). \end{aligned} \quad (\text{D.11})$$

The solution reads

$$\begin{aligned} c_0(t) &= \cos \varphi(t) \\ c_1(t) &= \frac{i}{\sqrt{2}} e^{-2it} \sin \varphi(t) \end{aligned} \quad (\text{D.12})$$

with the phase

$$\varphi(t) = \frac{AT}{16} \sqrt{\frac{\pi}{2}} \left(1 + \frac{2}{\sqrt{\pi}} \int_0^{t/T} d\xi e^{\xi^2} \right). \quad (\text{D.13})$$

Note that this phase $\varphi(t)$ is closely related to the error function. The outgoing wave has populated three momenta with the probabilities

$$\begin{aligned} P_0(t) &= |c_0(t)|^2 = \cos^2 \varphi(t) \\ P_{\pm 1}(t) &= |c_{\pm 1}(t)|^2 = \frac{1}{2} \sin^2 \varphi(t) \end{aligned} \quad (\text{D.14})$$

and the asymptotic value for the accumulated phase $\varphi(t \gg T)$ yields

$$\varphi(+\infty) \equiv \varphi_0 = \frac{AT}{8} \sqrt{\frac{\pi}{2}}. \quad (\text{D.15})$$

This is nothing but the area under the curve $A/(8\sqrt{2}) \exp(-t^2/T^2)$ and therefore φ_0 is proportional to the product AT . We can adjust the parameter AT in such a way that the zeroth transversal momentum component vanishes. Hence, $P_0 = 0$ corresponds to $\varphi_0 = \pi/2$. In this case, known in optics as a $\pi/2$ pulse, the light crystal transforms the incident atomic wave with the transversal momentum $p = 0$ into the two first momentum components and acts like a highly efficient beam-splitter.

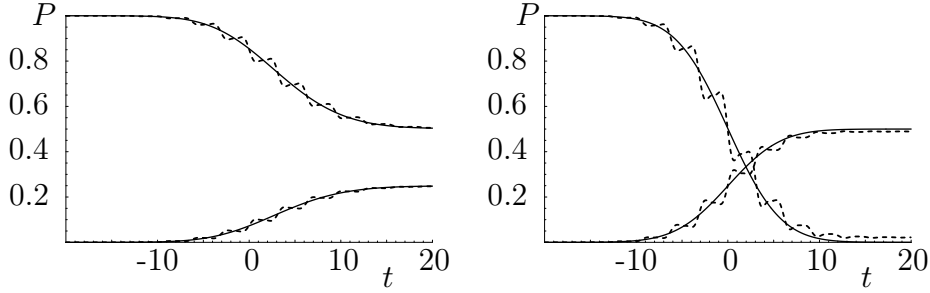


Figure D.1: Comparison of numerical and analytical results for $A = 0.5$ (left) and $A = 1.0$ (right). The dotted lines are taken from the probability evolutions out of Figs. 4.4 and 4.5. The solid lines are calculated from Eq. (D.14) and show a good agreement. Note, that the oscillations are not included in the analytical approach yet and therefore the analytical solutions are smooth.

Review of Numerical Results

The results of the numerical solution of the Schrödinger equation (4.3) are shown in Figs. 4.4 to 4.6 for the resonant modulation frequency $\omega_m = 1$, and different values of the modulation amplitude A . For small values of A (see for example Fig. 4.4) where we set $A = 0.5$, the atomic density acquires a chessboard structure. The size of the dark and bright areas is comparable and the contrast grows towards the end of the interaction region. The structure becomes clear from the plots of the momentum components. First of all, we see that only three of the momentum components are involved, c_0 and $c_{\pm 1}$. Their mutual coherence is responsible for the chessboard structure of the atomic density. During the interaction the probability of the zeroth momentum is decreasing while the probabilities of the first two ones build up. The momenta are exchanged by a sequence of “kicks” on the background of a regular behavior.

In Fig. D.1 we show the results from Eq. (D.14) for the intensities $A = 0.5$ and $A = 1.0$ (solid lines). With dashed lines we have plotted the previously obtained results from our numerical simulations. These earlier results are plotted in dashed style and taken from Figs. 4.4 and 4.5. Apart from the oscillations in the momentum probabilities arising from the kicks in the potential modulation both plots show the same tendency.

Beam-Splitter

In Fig. 4.5 we show the plots for $A = 1$. This case is now within the regime of the $\pi/2$ pulse. Therefore, there is an almost complete exchange in the

population of the involved momenta. The components $c_{\pm 1}$ take over almost all the population. This means that the outgoing wave contains the first two momentum components and the light crystal acts as a beam-splitter for atomic waves.

We emphasize that this beam splitter differs from the usual one. In a standard situation the incoming wave is split up into two parts: The continuation of the infalling wave and a split-off. In the present case the infalling wave completely vanishes and the two, previously completely absent, waves appear.

The resulting structure for the atomic density is seen at the end of the interaction region. The density shows a fractional space period compared to the periodicity of the crystal. This structure is a direct consequence of the beam-splitter properties of the setup. Note that this fractional period appears at the end of the interaction and could be measured with near-field methods.

Back Scattering

A further increase in the amplitude A leads to a larger number of oscillations between the involved momentum components as shown in Fig. 4.6. Moreover, the kicks in the momentum exchange become stronger. Nevertheless, the atomic density exhibits essentially the same structures as in the previous case because there are still only three momenta involved. When the population of the momentum components is inverted we see a fractional period of the atomic density.

Likewise, for even larger values of the amplitude A the excitation of additional momentum components occurs. Their presence makes the atomic density plots more complicated and we expect the generation of carpet like structures [23, 42].

We found that the generation of the first momentum component for a fixed modulation frequency and interaction time depends on the amplitude. How is this situation influenced by a changing modulation frequency? In Fig. D.2 we present the dependence of the probability of the zeroth component on the modulation frequency ω_m . The population of the first momentum component is obtained by $|c_1(\infty)|^2 = (1 - |c_0(\infty)|^2)/2$. The amplitude A is assumed to be moderate and kept fixed. The curve indicates a clear resonance behavior near $\omega_m = 1$. The width of the resonance is determined by the inverse time of flight $1/T$. For small frequencies the system does not depart too far from the adiabatic regime. When the modulation is fast enough, the system is not able to follow the rapid sequence of pulses and does not accumulate a significant change. Only when the modulation is adjusted to

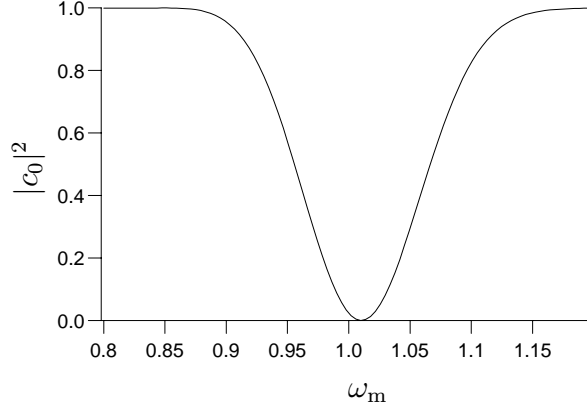


Figure D.2: Probability of the initial momentum state in the far field. We plot the probability $|c_0|^2$ to find the atoms in the transversal momentum state $p = 0$ depending on the modulation frequency ω_m with a fixed amplitude $A = 1.0$.

the interaction time and to the amplitude we obtain a considerable population transfer. Note, that the change of the modulation frequency ω_m is easily obtained by changing the crossing angle θ .

D.2 Quantum Kicks

When we include the nonresonant terms in Eq. (D.11) we find

$$\begin{aligned} i \dot{c}_0(t) &= -\frac{1}{4}A e^{-t^2/T^2} \left[\frac{1}{2} e^{2it} + \left(1 + \frac{1}{2} e^{-2it}\right) \right] c_1(t) \\ i \dot{c}_1(t) &= 2c_1(t) - \frac{1}{8}A e^{-t^2/T^2} \left[\frac{1}{2} e^{-2it} c_0(t) - \left(1 + \frac{1}{2} e^{2it}\right) \right] c_0(t). \end{aligned} \quad (\text{D.16})$$

These nonresonant terms are obviously responsible for a series of “quantum kicks” in the functions $P_{0,\pm 1}(t)$. Using perturbation theory we find the corrections $\partial c_{0,1}$ of first order. Together with Eq. (D.12) these corrections yield

$$\begin{aligned} c_0(t) &= \cos \varphi(t) + \partial c_0(t) \\ c_1(t) &= \frac{i}{\sqrt{2}} e^{-2it} (\sin \varphi(t) + \partial c_1(t)) \end{aligned}$$

with

$$\begin{pmatrix} \partial c_0 \\ \partial c_1 \end{pmatrix} = \frac{A}{4\sqrt{2}} \int_{-\infty}^t d\tau e^{-\tau^2/T^2} \left\{ \begin{pmatrix} -\sin \varphi(t) \\ \cos \varphi(t) \end{pmatrix} (\cos 2\tau + \frac{1}{2} \cos 4\tau) + \right. \\ \left. i \begin{pmatrix} -\sin[\varphi(t) - \varphi(\tau)] \\ \cos[\varphi(t) - \varphi(\tau)] \end{pmatrix} (\sin 2\tau + \frac{1}{2} \sin 4\tau) \right\}$$

where $\varphi(t)$ is taken from Eq. (D.13). Hence, we find the probabilities

$$\begin{aligned} P_0(t) &= \cos^2 \varphi(t) - \sin 2\varphi(t) \frac{1}{\sqrt{32}} A \int_{-\infty}^t d\tau e^{-\tau^2/T^2} (\cos 2\tau + \frac{1}{2} \cos 4\tau) \\ P_{\pm 1}(t) &= \frac{1 - P_0(t)}{2}. \end{aligned} \tag{D.17}$$

Note, that the contributions from all higher momenta are negligible and therefore the conservation law reads $P_0 + P_1 + P_{-1} = 1$. This will reappear in Fig. D.3 where we compare the numerical results shown in Fig. 4.5 with the analytical results taken from Eqs. (D.17). The numerical results are plotted with dashed lines whereas the analytical approximation is shown in the solid style.

For times $t > 5$ we see a small difference. The analytically calculated value is too small. This we can understand since the perturbation theory brings in corrections of first order. Therefore, we include in $|c_i|^2$, $i = 0, 1$, only linear terms of ∂c_i . Hence, the analytical value is too small for c_0 or P_0 , respectively. Since $P_{\pm 1}$ is calculated from P_0 the deviation has the opposite sign in this case.

D.3 Conclusions

We have studied the dynamics of a normal incident atomic wave on a two-dimensional light crystal. The geometry of the crystal is obtained by crossing two identical standing laser fields under the angle θ . The periodic modulation in the longitudinal direction causes an additional transversal modulation of the atomic wave. This modulation appears already for moderate amplitudes of the crystal potential, that is for $(dE)^2/(2\hbar^2\omega_R\Delta) \sim 1$. Without the additional modulation the overall dynamics would be very simple. The incoming wave is almost unperturbed by the crystal and the outgoing wave is identical to the incoming one. The longitudinal modulation is determined by the Doppler frequency ω_D which is easily controlled by the crossing angle

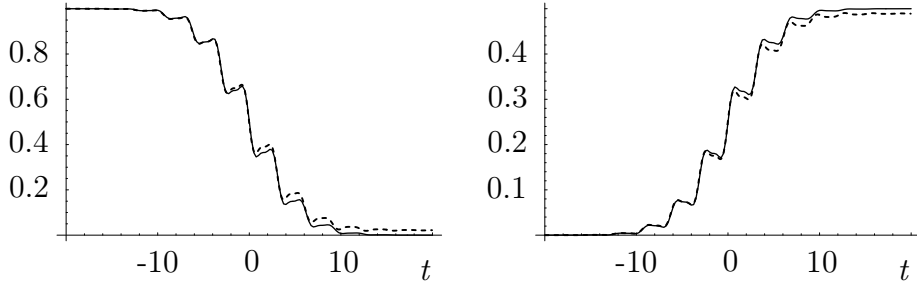


Figure D.3: Comparison between numerical and analytical results including the kicks for $A = 1.0$. The left pictures displays P_0 whereas the right one shows $P_{\pm 1}$. The dashed lines are the evolutions of probabilities taken from Fig. 4.5. The solid lines are the results of Eq. (D.17). We find good agreement at the beginning. In the later part there are small differences due to the approximation of $|c_i|^2$, $i = 0, 1$, where we neglected the higher order terms of the correction.

of the laser beams. It is interesting to note that the Doppler frequency is given by the ration $2\omega_D = \theta/\theta_{\text{diff}}$ where $\theta_{\text{diff}} = 2\hbar k/(Mv)$ is the diffraction angle. The additional modulation breaks the adiabaticity condition for the incoming wave leading to several interesting effects:

First, the periodicity of the modulation can be adjusted in such a way, that the incoming wave is almost completely transformed into two outgoing waves. This process can be viewed as the action of an atomic wave beam-splitter. The incoming atomic wave, which can be viewed as being in the momentum “ground state” $p = 0$, gives rise to two outgoing waves in the “first excited state” $p = \pm 2\hbar k$. The transfer is most efficient at the point of the Doppleron resonance.

Second, due to the change in population of the momentum components the atomic density is spatially modulated. In particular, the outgoing wave can take the fractional transversal periodicity of the optical crystal.

The crystal can be used to detect the longitudinal components of the incoming atomic wave. The longitudinal velocity controls the time of flight of the particular components through the crystal and this can be resolved via measuring the population of the higher momentum components.

The longitudinally modulated optical crystal shows interesting physical effects. It provides a useful tool for the engineering of the transversal profile of atomic waves and might serve as a detection tool for resolving the longitudinal properties of atomic wave packets [37]. A sequence of such crystals could be used to construct a beam splitter for any pair of even order momentum components. Such a device would then be a direct generalization of

the ordinary beam-splitter and could be used to generate spatially periodic atomic waves of higher spatial periodicities than that of the crystal [32].

Appendix E

The Numerics

The basic program during our work uses the operator-splitting technique. With this scheme we can easily integrate one-level wave functions even with rather complicated potentials.

The root is the time-dependent Schrödinger equation

$$i\hbar \frac{\partial}{\partial t} \psi(x, t) = \hat{H}(t) \psi(x, t).$$

Note that the Hamiltonian might be time-dependent, too. The solution of this differential equation has a simple form

$$\psi(x, t) = \hat{T} \exp \left[-\frac{i}{\hbar} \int_{t_0}^t dt' \hat{H}(t') \right] \psi(x, t_0)$$

where \hat{T} denotes the time ordering operator. The difficulty comes from a typical potential $V(\hat{x})$. Indeed, the nonvanishing commutator between \hat{x} and \hat{p} requires a special treatment. This can be done in an easy but tricky way.

For the sake of simplicity we consider in the numerical solution only a single step of dt

$$\psi(x, t + dt) = \exp \left[-\frac{i}{\hbar} \left(\frac{\hat{p}^2}{2} + V(\hat{x}) \right) dt \right] \psi(x, t)$$

which can be split up into two parts

$$\psi(x, t + dt) = \exp \left[-\frac{i}{\hbar} \frac{\hat{p}^2}{2} dt \right] \cdot \exp \left[-\frac{i}{\hbar} V(\hat{x}) dt \right] \psi(x, t).$$

From the Baker-Hausdorff theorem [39] we know that the nonvanishing commutator of \hat{p} and \hat{x} introduces a series of commutators:

$$\exp(\hat{p}) \exp(\hat{x}) = \exp \left(\hat{x} + \hat{p} + \frac{1}{2} [\hat{p}, \hat{x}] + \dots \right).$$

Since these commutators are weighted by powers of dt we can neglect higher powers.

Since ψ is in position representation we can easily evaluate the exponential with the potential term and reach

$$\psi(x, t + dt) = \exp\left[-\frac{i}{\hbar} \frac{\hat{p}^2}{2} dt\right] \cdot \tilde{\psi}(x, t)$$

where we apply a Fourier transform to the equation and get the momentum representation

$$\phi(p, t + dt) = \exp\left[-\frac{i}{\hbar} \frac{\hat{p}^2}{2} dt\right] \cdot \tilde{\phi}(p, t).$$

Then the second step of the propagation can take place. The momentum operator in momentum space is simple and we after a second Fourier transform we have solved the time step dt .

The crucial point of this approximation is the propagation after the first Fourier transform. We express the kinetic propagator at a time which should be already over. Nevertheless, if dt is small enough, we can neglect the error [36].

One way to improve the result is to reduce the step in the propagators to $dt/2$ and evaluate $\tilde{\psi}$ and $\tilde{\phi}$ at $t = t + dt/2$. With this scheme we can reduce the error to the order of dt^3 . In fact, the time steps used in this thesis are small enough that the approximation with full steps dt is good enough.

Bibliography

- [1] R. Abfalterer, C. Keller, S. Bernet, M. Oberthaler, J. Schmiedmayer, and A. Zeilinger, *Phys. Rev. A* **56**, R4365 (1997).
- [2] M. Abramowitz and I. A. Stegun, *Handbook of Mathematical Functions* (Dover Publications, New York, 1972)
- [3] H. Bateman and A. Erdelyi, *Higher transcendental functions*, Vol. 2 (1953)
- [4] A. S. Bell, T. Pfau, U. Drodofsky, J. Stuhler, T. Schulze, B. Brezger, S. Nowak, and J. Mlynek, *Microelectronic Engineering* **41-42**, 587 (1998).
- [5] K. Bergmann, H. Theuer, and B. W. Shore, *Rev. Mod. Phys.* **70**, 1003 (1998)
- [6] *Atom interferometry*, ed. P. R. Berman (Academic Press, New York, 1997).
- [7] S. Bernet, M. K. Oberthaler, R. Abfalterer, J. Schmiedmayer, and A. Zeilinger, *Phys. Rev. Lett.* **77** 5160 (1996).
- [8] S. Bernet, R. Abfalterer, K. Keller, J. Schmiedmayer, and A. Zeilinger, *J. Opt. Soc. Am. B* **13** 321 (1996).
- [9] S. Bernet, R. Abfalterer, K. Keller, J. Schmiedmayer, and A. Zeilinger, *J. Opt. Soc. Am. B* **15** 2817 (1998).
- [10] S. Bernet, R. Abfalterer, K. Keller, J. Schmiedmayer, and A. Zeilinger, *Proc. Roy. Soc. A* **455** 1509 (1999).
- [11] M. V. Berry and S. Klein, *J. of Mod. Optics* **43**, 2139 (1996) and references therein.
- [12] M. V. Berry and D. J. H. O'Dell, *J. Phys. A* **31** (1998) 2093.

- [13] R. J. Celotta, R. Gupta, R. E. Scholten, and J. J. McClelland, *J. Appl. Phys.* **79**, 6079 (1996).
- [14] M. S. Chapman, C. R. Ekstrom, T. D. Hammond, J. Schmiedmayer, B. E. Tannian, S. Wehinger, and D. E. Pritchard, *Phys. Rev. A* **51**, R14 (1995).
- [15] D. O. Chudesnikov and V. P. Yakovlev, *Laser Phys.* **1** 110 (1991).
- [16] J. F. Clauser and S. Li, *Phys. Rev. A* **49**, R2213 (1994).
- [17] U. Drodofsky, J. Stuhler, T. Schulze, M. Drewsen, B. Brezger, T. Pfau, and J. Mlynek, *Appl. Phys. B* **B65**, 755 (1997).
- [18] U. Drodofsky, J. Stuhler, Th. Schulze, M. Drewsen, T. Pfau, and J. Mlynek, *Microelectronic Engineering* **35**, 285 (1997).
- [19] R. Gupta, J. J. McClelland, Z. Jabbour, and R. J. Celotta, *Appl. Phys. Lett.* **67**, 1378 (1995).
- [20] U. Janicke and M. Wilkens, *Journal de Physique II* **4**, 1975 (1994).
- [21] U. Janicke and M. Wilkens, *Phys. Rev. A* **50**, 3265 (1994).
- [22] K. S. Johnson, J. H. Thywissen, N. H. Dekker, K. K. Berggren, A. P. Chu, R. Younkin, and M. Prentiss, *Science*, **280**, 1583 (1998).
- [23] A. E. Kaplan, P. Stifter, K. A. H. van Leeuwen, W. E. Lamb Jr., and W. P. Schleich, *Physica Scripta*, **T76**, 93 (1998).
- [24] H. Katori, S. Schlipf, and H. Walther, *Phys. Rev. Lett.* **79**, 2221 (1997).
- [25] E. Kamke, *Differentialgleichungen — Lösungsmethoden und Lösungen I* (B. G. Teubner, Stuttgart, 1983).
- [26] A. P. Kazantsev, G. I. Surdutovitch, and V. P. Yakovlev, *Mechanical actions of light on atoms* (World Scientific, Singapore, 1990).
- [27] D. S. Krähmer, A. M. Herkommer, E. Mayr, V. M. Akulin, I. Sh. Averbukh, K. A. H. van Leeuwen, V. P. Yakovlev, and W. P. Schleich, in: *Quantum Optics VI*, D. F. Walls and J. D. Harvey eds., p. 87 (Springer, Berlin, 1994).
- [28] E. Kyrolä and S. Stenholm, *Optics Commun.* **22** 123 (1977).

- [29] J. J. McClelland, R. E. Scholten, E. C. Palm, and R. J. Celotta, *Science* **262**, 877 (1993).
- [30] J. J. McClelland, R. Gupta, Z. J. Jabbour, and R. J. Celotta, *Aust. J. Phys.* **49**, 555 (1996).
- [31] S. Meneghini, I. Jex, K. A. H. van Leeuwen, M. R. Kasimov, W. P. Schleich, and V. P. Yakovlev, *Laser Phys.* **10** 1 (2000).
- [32] S. Meneghini, I. Jex, W. P. Schleich, and V. P. Yakovlev *in preparation*
- [33] S. Nowak, T. Pfau, and J. Mlynek, *Microelectronic Engineering* **35**, 427 (1997).
- [34] S. Nowak, Ch. Kurtsiefer, C. David, and T. Pfau, *Opt. Lett.* **22**, 1430 (1997).
- [35] P. Pechukas and J. Light, *J. Chem. Phys.* **44**, 3897 (1966).
- [36] W. H. Press, B. P. Flannery, S. A. Teukolsky, and W. T. Vetterling, *Numerical Recipes in C* (Cambridge University Press, Cambridge, 1988)
- [37] D. E. Pritchard, R. A. Rubenstein, A. Dhirani, D. A. Kokorowski, E. T. Smith, T. D. Hammond, and B. Rohwedder, *Phys. Rev. A* **59** 4641 (1999).
- [38] M. Raizen, *Adv. At. Mol. Phys.* **41** 43 (1999).
- [39] R. D. Richtmyer, *Principles of Advanced Mathematical Physics II* (Springer, New York, 1986).
- [40] R. E. Scholten, J. J. McClelland, E. C. Palm, A. Gavrin, and R. J. Celotta, *J. Vac. Sci. Technol. B* **12**, 1847 (1994).
- [41] P. Stifter, W. E. Lamb, and W. P. Schleich, in: *Frontiers of Quantum Optics and Laser Physics*, p. 236, (Springer, Berlin, 1997).
- [42] P. Stifter, C. Leichtle, W. P. Schleich, and J. Marklof, *Z. Naturforsch.*, **52a**, 377 (1997).
- [43] H. F. Talbot, *Philos. Mag.* **9**, 401 (1881).

Acknowledgment

Talent and knowledge are basic fundamentals of a PhD thesis. Nevertheless, there are many more factors contributing to such an opus. Most of these factors have names, some do not. All their work is reflected in a good thesis but unfortunately it is impossible to thank and mention all of them. Therefore, I want to show my thankfulness to all of them who helped me in some way to do my work.

Of course, there are helpful friends which are elementary necessary:

- The most important person for my thesis is Prof. Schleich. He triggered already years ago my interest in quantum mechanics with his beginner's lecture. For more than five years he was the father of my life in science. His encouraging presentations in lectures — at the university as well as at conferences — gave me the motivation to work with him.

His Texan way of life shows me that my German view is small. We have to think globally and take a glance at other cultures in a world which is smaller than it has ever been. I met many people from different countries. This colorful life I will miss for sure and the only hope I can take with me is that I found friends in the quantum family round the world and I wish to keep contact forever.

- Prof. Yakovlev put the theoretical spirit into my numerical simulations. He taught me the physical understanding of my numbers. Additionally, he built bridges in theoretical approaches which — for me — were unknown relations and functions. Without his help I could never managed to explain all my results.
- Ton van Leeuwen and Volodja Savichev did the startup of my PhD thesis with their contribution to the focusing work. Ton as an experimentalist told us theoreticians what is possible in real life. He gave me the opportunity to see a real experiment in the lab. Volodja was one of my first tutors in theory.

- Thanks to the Humboldt foundation I had a very powerful year together with Igor Jex. He buffered the fights I had to stand with Prof. Yakovlev. Without his help I could never complete the thesis on atom optics. Missing his contributions this work would be a mixture of different subjects of quantum physics. He kept the main stream and was one of the most important columns in my scientific career.
- Karl Vogel taught me two things: I have to take people the way they are; I cannot change minds or habits. I have to go to the people and accept their way. But if I do so, I get good answers and helpful hints. It was not easy to learn this lesson but finally I think I got it.
- The department provides several support. The community is essential to stand all the challenges. Further I made friends there to help me in special problems especially Kathy who improved my English and was always there for us students. I want to thank Markus Cirone, Dietmar Fischer, Matthias Freyberger, and Holger Mack for reading my thesis.
- I do not deny that to write a thesis is very exhausting. All the problems during the years rise doubts. Is it really necessary to get a Phd? In all these crises Amélie gave me the motivation to hold on. This thesis is the proof for her success.
- Mein allergrößter Dank gilt aber meinen Eltern. Ohne ihre Unterstützung wäre mein Studium, meine Promotion und all der Rest im Leben außerhalb der Universität nicht möglich gewesen. Es ist unmöglich, diese Dankbarkeit in Worte zu fassen und deshalb komprimiere ich alles in dem schlichten aber wichtigen Wort: *Danke*.

Curriculum Vitae

Born: 15th February 1972 in Ulm-Söflingen, Germany

Parents: Wolfgang Meneghini, and Irmgard Meneghini, née Nündel

Nationality: German

09/78 – 07/80 Eduard-Mörike Grund- und Hauptschule, Blaustein

08/80 Move to Laupheim

09/80 – 07/82 Grundschule Laupheim

09/82 – 06/91 Gymnasium Laupheim

07/91 – 06/92 Military Service at the Gustav-Adolf-Kaserne in Nürnberg and
the Kurt-Georg-Kiesinger-Kaserne in Laupheim

10/92 – 05/97 Study of Physics and Mathematics at the University of Ulm

06/97 – 09/00 PhD Student in the Department of Quantum Physics

List of Publications

1. S. Meneghini, P. J. Bardroff, E. Mayr and W. P. Schleich, *Comment on “Nature of Dynamical Localization in Atomic Momentum Transfer Experiments”*, Phys. Rev. Lett. **78**, 1195 (1997)
2. S. Meneghini, V. I. Savichev, K. A. H. van Leeuwen and W. P. Schleich, *Atomic Focusing and Near Field Imaging: The Combination to Produce Small-Period Nanostructures through Atomic Near-Field Imaging*, Appl. Phys. B **70**, 675 (2000)
3. This paper is reprinted in K. A. H. van Leeuwen, S. Meneghini and W. P. Schleich, *Atom optics in the near-field limit: applications to nanostructure production*, Van A tot Q, **13**, 25 (1999)
4. S. Meneghini, I. Jex, K. A. H. van Leeuwen, M. R. Kasimov, W. P. Schleich and V. P. Yakovlev, *Atomic Motion in Longitudinally Modulated Light Crystals*, Laser Physics **10**, 116 (2000)
5. S. Meneghini, I. Jex, W. P. Schleich and V. P. Yakovlev, *Reshaping of Atomic Waves with Two-Dimensional Optical crystals*, J. Opt. B: Quantum Semiclass. Opt. (submitted)
6. H. Mack, S. Meneghini and W. P. Schleich, *Atom Optics and the Discreteness of Photons*, Verh. Nat. Kon. Ned. Akad. van Wetensch. (accepted)
7. S. Meneghini, I. Jex, M. R. Kasimov, K. A. H. van Leeuwen, W. P. Schleich and V. P. Yakovlev, (*in preparation*)